Title
Modeling Strength Degradation of Reinforced Concrete Structural Walls

Author
Safdari, Amin

Publication Date
2023

Peer reviewed|Thesis/dissertation

UNIVERSITY OF CALIFORNIA

Los Angeles

Modeling Strength Degradation of Reinforced Concrete Structural Walls

A dissertation submitted in partial satisfaction of the

requirements for the degree Doctor of Philosophy

in Civil Engineering

by

Amin Safdari

2023

ABSTRACT OF THE DISSERTATION

Modeling Strength Degradation of Reinforced Concrete Structural Walls

by

Amin Safdari

Doctor of Philosophy in Civil Engineering

University of California, Los Angeles, 2023

Professor John Wright Wallace, Chair

Reinforced concrete structural walls are a widely used structural system in modern construction in regions where strong ground shaking is likely to occur. For performance-based design of structural walls, including coupled wall systems, it is necessary to model cyclic responses with strength and stiffness deterioration of the prototype system over a wide range of shaking intensities. Current models typically incorporate strength loss using ad-hoc approaches that manipulate material relations to produce strength loss that are difficult to calibrate for the broad range of expected shaking intensities. To address this issue, a model is proposed that captures strength and stiffness degradation compatible with backbone curves that are currently available in the literature. The model is tested in case studies under static and dynamic loading to demonstrate its reliability and effectiveness. The model is refined further to be used for coupled wall systems where the fluctuation of shear and axial load in the coupled piers makes it difficult to pre-determine the deformation parameters of the backbone curves for the piers.

In a separate but related study, a database of reinforced concrete wall tests is assembled to develop a new model that estimates the plastic hinge length of flexure controlled structural walls and validate the model against test results. Plastic hinge lengths have been widely used and it is well known that deformation parameters of backbone curves (Structural walls or any other element) depend on element size (Plastic hinge length). The goal of this study is to calibrate backbone curve deformation parameters for a range of wall element sizes and then use the calibrated plastic hinge lengths in the subsequent case studies that incorporate strength loss.

The dissertation of Amin Safdari is approved.

Henry V. Burton

Ertugrul Taciroglu

Kristijan Kolozvari

John Wright Wallace, Committee Chair

University of California, Los Angeles

2023

To my parents, Nahid and Masoud

Table of contents

List of figures

List of Tables

Vita

2011	B.S., Civil Engineering, Sharif University of Technology
2013	M.S., Structural Mechanics, Sharif University of Technology
2016	M.S., Structural and Earthquake Engineering, UCLA
2016 - 2020	Teaching Assistant, UCLA
2018 - 2023	Graduate Student Researcher, UCLA
2019	Structural Engineering Intern, Skidmore, Owings & Merrill

Chapter 1 Introduction

1.1 General

There is an increasing tendency towards the use of reinforced concrete structural walls as the lateral force resisting system of mid- and high-rise buildings in modern construction. Reinforced concrete structural walls possess significant stiffness that decreases lateral drifts and limits damage to nonstructural components. Extensive research on design, detailing and modeling of reinforced concrete walls has been carried out over the last 50 years and results of these studies are reflected in Chapter 18 of ACI 318-19 [9] for design of special reinforced concrete structural walls. In addition to high stiffness, if designed and detailed per ACI 318, structural walls have proven to provide sufficient ductility to dissipate substantial earthquake energy in Design Earthquake (DE) and risk targeted maximum considered earthquake (MCE_R) events. Use of coupled wall systems is also popular in cases where cantilever walls do not provide sufficient lateral stiffness, either due to limits on cantilever walls from architectural constraints or for taller buildings.

ASCE 7-22 [1] chapter 12 specifies a prescriptive procedure for analysis and design of RC structural walls and other conventional lateral force resisting systems. For prescriptive design, Table 12-2-1 of ASCE 7 [1] enforces height limits on, or prohibits the use of, some lateral force resisting systems for certain seismic design categories. To use these systems where they are restricted, or to use a lateral force resisting system not recognized by Table 12-2-1, section 12.2.1 of ASCE 7 allows alternative design procedures if the intent of the code is satisfied. These procedures include Nonlinear Dynamic Analysis of ASCE 7 [1] chapter 16, or in case of tall building, a Performance Based Seismic Design according to consensus guidelines. Both procedures provide acceptance criteria to meet performance objectives to achieve a prescribed level of performance, e.g., a 10% or less probability of collapse in buildings with a risk category

of II, 5% or less probability of collapse in buildings with a risk category of III, and 2.5% or less probability of collapse in buildings with a risk category of IV corresponding to an MCE_R shaking. Both ASCE 7 chapter 16 and tall buildings guidelines (e.g., PEER Tall Buildings Initiative (2017) [3] and LATBSDC (2020) [54]) require mathematical models that capture the nonlinear response of structural elements. Such a model must be compatible with nonlinear response (backbone) relations specified in ASCE 41, or be validated using appropriate laboratory test data. ASCE 7 section 16.3.1 specifically states:

"Degradation in element strength or stiffness shall be included in the hysteretic models unless it can be demonstrated that response is not sufficient to produce these effects."

The PEER TBI guidelines, in Section 4.4.3, also prohibits the use of component models that do not account for post-peak strength degradation for nonlinear models used for MCE_R evaluation.

1.2 Objectives and scope

While Performance Based Seismic Design of tall buildings has become relatively common in recent years, mathematical models that reliably capture strength and stiffness degradation of flexure controlled structural walls without substantial calibration and validation are not available in literature. Even with extensive calibration and validation, the available models have drawbacks, e.g., when applied to coupled walls where significant variations in demands (axial, shear, moment) occur. The objective of this research is to provide a computer model that captures post-yield strength and stiffness degradation such that the envelope of hysteretic force deformation curve matches a specified backbone curve, e.g., as specified by ASCE 41-17. The model must also retain the important features of traditional models being used in practice, such as variation in flexural strength due to variation in axial load, and fluctuation of the neutral axis.

1.3 Organization

This dissertation is organized into 7 chapters. Following the introductory Chapter 1, Chapter 2 reviews previous studies that have focused on modeling strength and stiffness deterioration of structural members. Most of the work on this topic has focused on developing single springs, with force deformation rules that capture different modes of stiffness and strength degradation. These springs are used for structural components whose deterioration parameters depend on response in one degree of freedom only, and cannot be used to model structural walls without oversimplification of prototype's response.

Chapter 3 provides an overview of some macro-models that have been widely used in practice for modeling structural walls. Based on this review, the Multiple Vertical Line Element model is selected as a baseline model to develop a new model that appropriately captures strength and stiffness deterioration. A new approach for modeling the material (Reinforcing steel and concrete) used in the fiber section of this element is proposed. This approach serves as a platform that enables modeling of strength loss, compatible with a given backbone curve. The cyclic force deformation rules for the concrete and steel material relations are developed to address different load paths. The element and the material objects are coded in OpenSees [4], an open-source nonlinear dynamic analysis software for earthquake engineering purposes. The performance of this model is tested in two case studies. A cantilever structural wall, loaded with cyclic displacement-controlled loading and dynamic ground motion excitation.

Chapter 4 presents an algorithm for dynamic computation of deformation parameter d of the backbone curve proposed by Abdullah and Wallace (2019) [46][47], incorporated into ACI Code 369.1-22. This backbone curve will be adopted by future editions of ASCE 41. The variables on which the deformation parameters depend on (shear stress, axial load, and depth of the

compression zone) are formulated as functions of nodal displacement. The exact value of d, at the load step through which strength loss initiates, is calculated using the Newton approach. This algorithm is coded into the OpenSees wall element object and utilized in a case study that models a coupled wall system subjected to dynamic loading.

Obtaining the element backbone curve from the base shear versus roof drift response of a wall tested, requires that realistic estimate of the size of plastic hinge be determined. Chapter 5 investigates the height of plastic hinge for flexure controlled structural walls. The adjustments needed to be applied to the ASCE 41 backbone curves so that they could be appropriately used in the element developed in this study, are discussed. A summary of the work and the conclusions are presented in Chapter 6. An appendix provides supplemental data, documentations, and sample calculations.

Chapter 2 Literature review

Most research on the development and application of models that incorporate strength and stiffness degradation has been done in the last thirty years. Some important work regarding this subject is presented in this chapter.

2.1 Clough (1966) [5]

The importance of ductility for seismic design has been well documented. To evaluate the ductility capacity of code compliant concrete moment frames, the Portland Cement Association (PCA) was asked to conduct an experiment on an assembly of a concrete beam and column. The schematic of the test specimen, and the force deformation response are shown in Figure 2-1. An important observation in this test was stiffness degradation of the specimen in consecutive cycles. This gave rise to the question whether more strict ductility requirements should be imposed, because the energy absorption capacity of the system is reduced due to stiffness degradation. Clough conducted a parametric study on single degree of freedom models utilizing a proposed nonlinear spring that captured stiffness degradation.

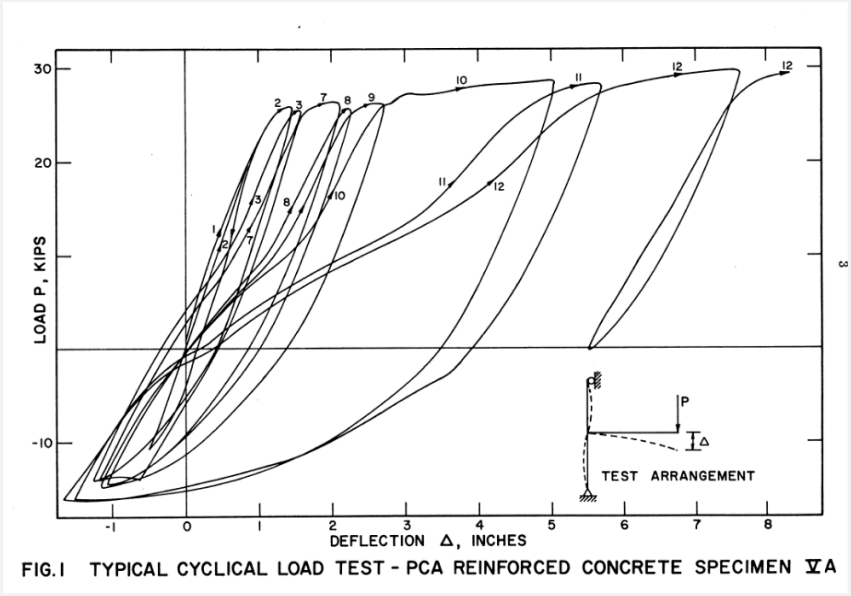

Figure 2-1 Test on beam column assembly by PCA

The force deformation response of the spring he proposed is shown in Figure 2-2.

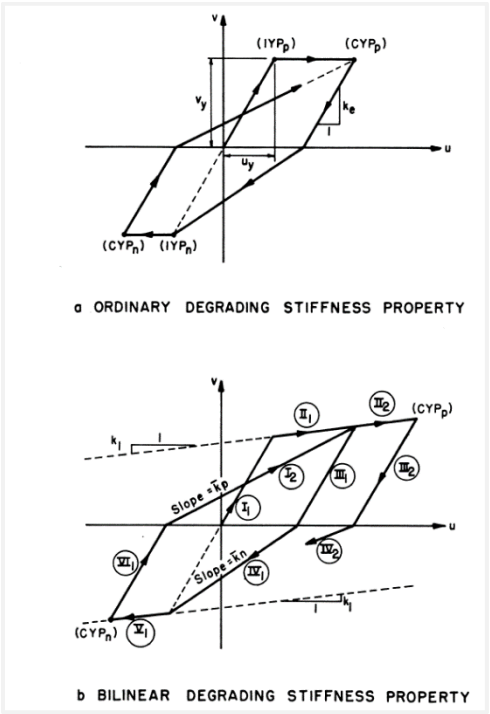

Figure 2-2 Force deformation of springs proposed bu Clough to model stiffness degradation

The primary variables in this study were yield strength, damping ratio, period, and the post yield stiffness of the SDOFs. A total of 384 nonlinear dynamic analyses with 4 different ground motions

were conducted. Figure 2-3 and Figure 2-4 show how the response of a system with an ordinary bilinear spring compared to that of a system with degrading spring.

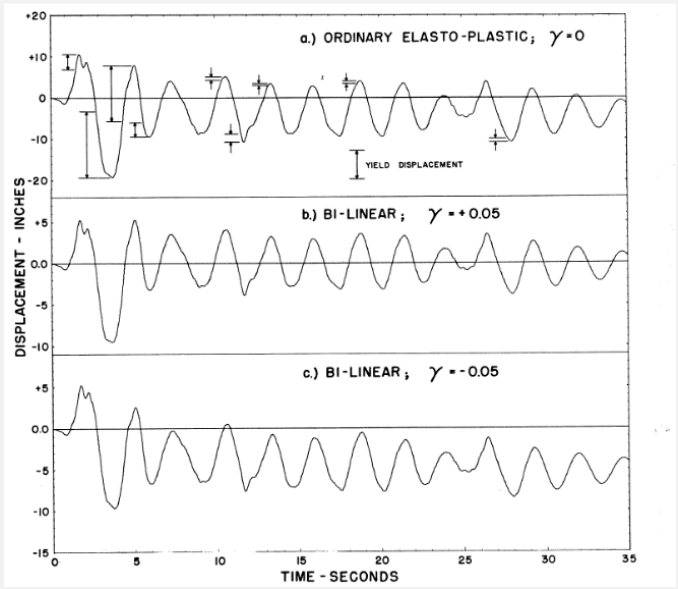

Figure 2-3 Response of an ordinary bilinear system by Clough

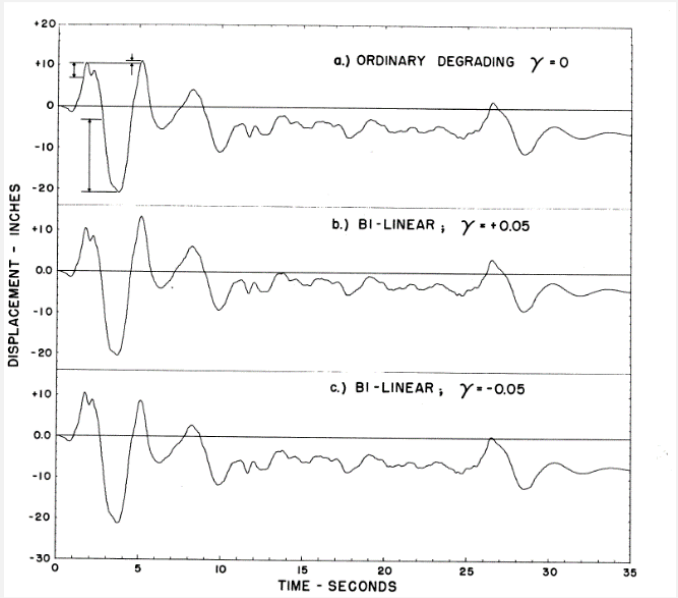

Figure 2-4 Response of a degrading system by Clough

The bilinear system essentially keeps vibrating with almost constant period after the initial pulses, while the degrading system shows a different response due to degrading stiffness. In Figure 2-3 and Figure 2-4, γ is the ratio of post-yield stiffness to the initial stiffness.

The results also show that:

1. For short period structures ($T = 0.3$ sec.), the maximum displacement of degrading structures is significantly more than that of the elastoplastic structure, whereas for long-period structures the maximum displacements are almost equal.
2. A negative post-yield stiffness (A representation of strength loss) has a disastrous effect on the response of the building.

2.2 FEMA P440 (2005) [6] and FEMA P440A (2009) [7]

FEMA P440 studied the effectiveness of, and proposed potential improvements to, two nonlinear static procedures (NSPs) in evaluating the seismic demands of buildings. These two are described in FEMA 273 (and FEMA 356) and in the ATC40 report and are referred to as the Coefficient Method and the Capacity Spectrum method, respectively. FEMA P440 emphasized the importance of cyclic and in-cycle strength and stiffness degradation in predicting building demands, and the need for developing models that capture such deterioration in future research. FEMA P440A, a follow-on document on FEMA P440, investigated the response of buildings considering strength and stiffness degradation. Different types of stiffness and strength degradation in available models were characterized in FEMA P440A. Figure 2-5 shows three different types of stiffness degradation. In the first model, loading and unloading stiffnesses are equal, and both degrade with an increase in maximum deformation. In the second model, the unloading stiffness does not degrade, but the reloading stiffness degrades with increase in maximum experienced deformation.

In the third model, unloading and reloading stiffnesses are different, and both degrade with increase in maximum observed deformation.

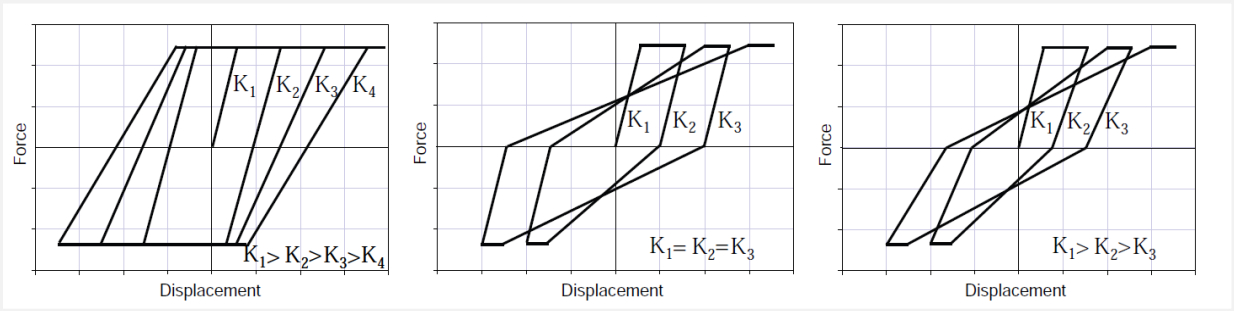

Figure 2-5 Different models of stiffness degradation

Figure 2-6 describes the pinching effect. The reloading stiffness degrades with increase in maximum deformation, until the load deformation path hits a target deformation, at which reloading continues with a much higher stiffness. This behavior is observed in reinforced concrete structures, where concrete cracks open when element is loaded in a certain direction but upon reloading in the opposite direction when the cracks close, stiffness is recovered.

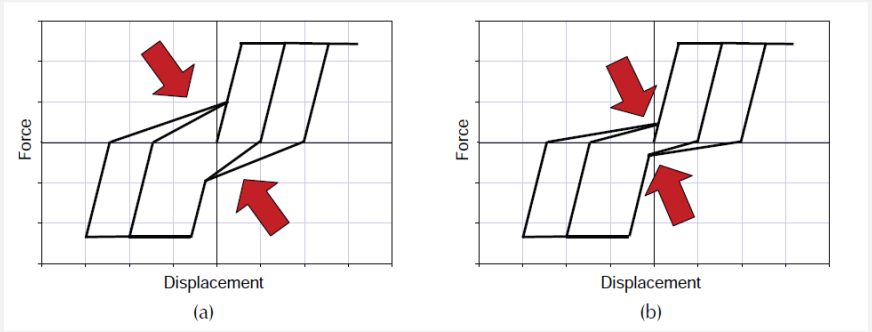

Figure 2-6 Moderate pinching in figure (a) and severe pinching in figure (b)

Figure 2-7 illustrates two sources of cyclic strength degradation. Figure 2-7 (a) shows strength degradation due to increasing nonlinear displacement in consecutive cycles. In Figure 2-7 (b), the level of nonlinear displacement remains constant, yet strength degrades due to increased number of cycles. Several analytical models have been developed that incorporate both types of cyclic

strength degradation. These models generally deteriorate the strength as a function of hysteretic energy dissipation.

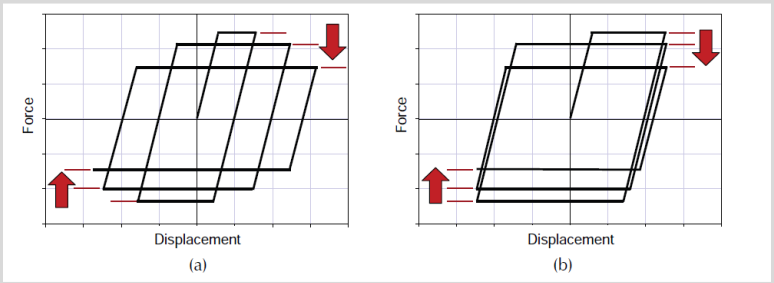

Figure 2-7 Cyclic strength degradation

Figure 2-8 (b) shows in-cycle strength degradation where, a softening (negative stiffness) branch of force deformation response is observed within a single loading excursion. The hysteretic response of a component with cyclic strength degradation under the same loading protocol (Loading protocol 1) is shown in Figure 2-8(a) for comparison.

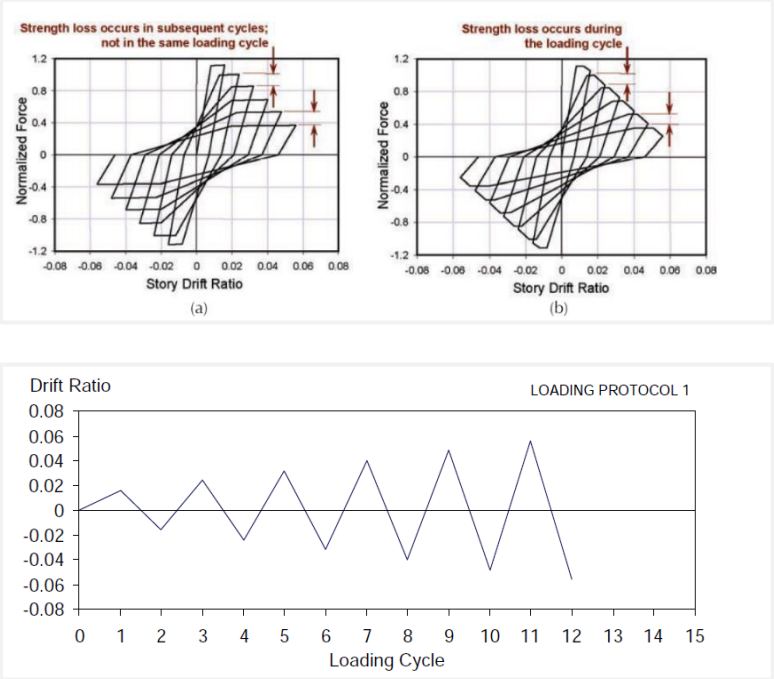

Figure 2-8 Cyclic and in-cycle strength degradation due to loading protocol 1

Note that the curve enveloping the force displacement response is similar for both modes of strength degradation, but the materials behave significantly different if loading protocol 2 is applied. as shown in Figure 2-9.

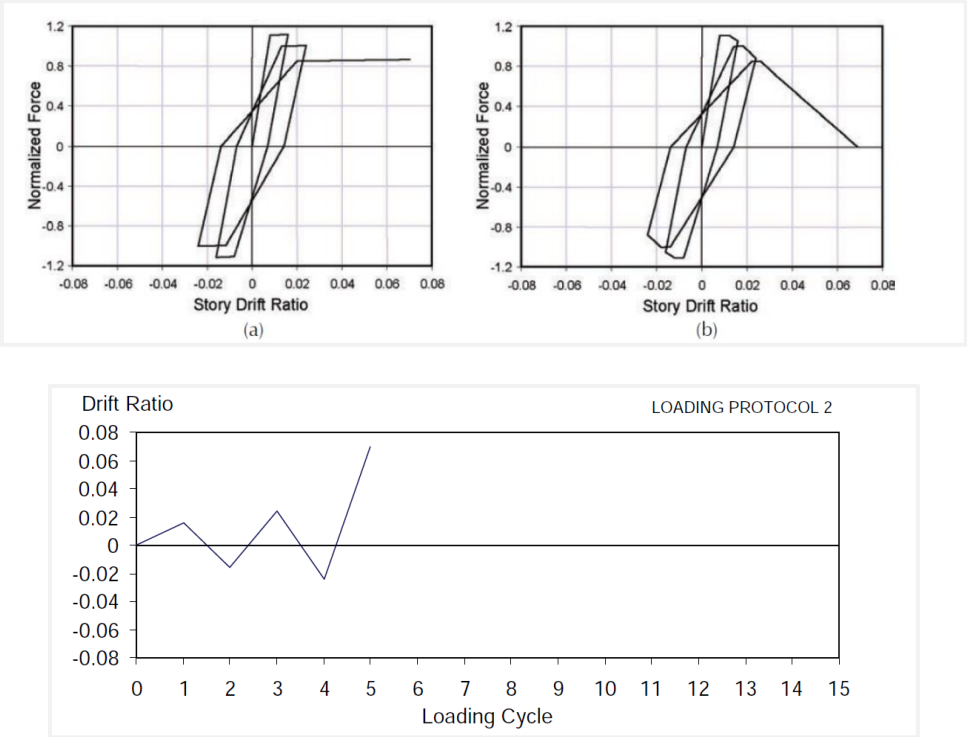

Figure 2-9 Cyclic and in-cycle strength degradation due to loading protocol 2

Although analyses have shown that for medium and long period buildings, the maximum observed deformation is almost equal for the two modes of strength degradation, the model with in-cycle strength degradation experiences much larger residual drift. This may result in dynamic lateral instability (Collapse). In an additional study, eight springs with a combination of strength and stiffness degradation modes were used as components of Single Degree of Freedom oscillators. The SDOFs modeled the nonlinear and degrading response of the following frames.

1. Typical gravity frame (e.g., steel)
2. Non-ductile moment frame (e.g., steel or concrete)

3. Ductile moment frame (e.g., steel or concrete)
4. Stiff non-ductile system (e.g., concentric braced frame)
5. Stiff and highly-pinched non-ductile systems (e.g., Infill wall)
6. Idealized elastic perfectly plastic system
7. Limited ductility moment frame (e.g., concrete)
8. Non-ductile gravity frames (e.g., concrete)

The effect of deterioration on the response and collapse of these frames was investigated.

2.3 Ibarra, Medina, and Krawinkler (2005) [8]

Ibarra, Medina, and Krawinkler developed models that exhibit stiffness and strength degradation of structural components. The basis of their model was three nonlinear models available in the literature. The three models are

1. Bilinear hysteretic model with post-yield strain-hardening and kinematic hardening
2. Peak-oriented hysteretic model
3. Pinching model

Figure 2-10 (a), (b), and (c) show the response of each hysteretic model. These models were modified to include a post-cap softening branch, and hysteretic rules were adjusted to work accordingly. Four modes of strength and stiffness degradation, listed below, were included in the force deformation rules. The reloading stiffness degradation was already captured in the basic peak-oriented and pinching models.

1. Basic strength degradation
2. Post-capping strength degradation
3. Unloading stiffness degradation

4. Accelerated reloading stiffness degradation

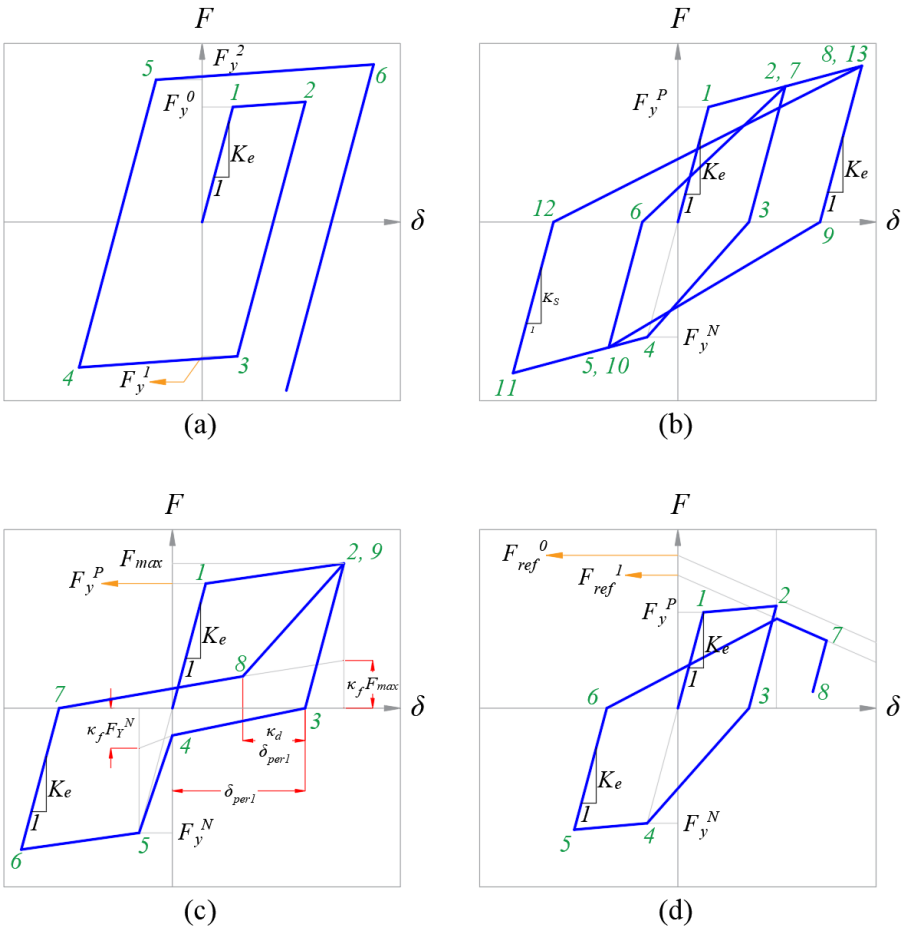

Figure 2-10 Basic models used by Ibarra, Medina, and Krawinkler. (a) Bilinear hysteretic model, (b) Peak-Oriented model, (c) Pinching model, (d) Cyclic deterioration by post-peak softening branch

The parameter that controls strength and stiffness deterioration, β_i, is calculated per Eq. 2-1 using the energy dissipated in excursion i.

$$\beta_i = \left(\frac{E_i}{E_t - \sum_{j=1}^{i} E_j}\right)^c, \qquad F_{ref}^1 = (1-\beta)F_{ref}^0 \qquad \text{Eq. 2-1}$$

In Eq. 2-1, E_i is the energy dissipated in excursion i, and E_t is the total energy dissipation capacity of the structural component, assumed to be independent of the loading protocol. It is expressed as

a function of area enclosed by the linear segment of the force deformation curve, as shown in Eq. 2-2.

$$E_t = \gamma F_y \delta_y \quad \text{Eq. 2-2}$$

Exponent c controls the rate of deterioration, recommended to be set between 1, and 2. The value of γ can be different in calculating different modes of deterioration (Strength or stiffness). An example of the application of Eq. 2-1 and Eq. 2-2, is shown in Figure 2-10 (d) where the post-cap softening segment is deteriorated according to Eq. 2-3. This calculation is done once the force deformation path crosses the horizontal axis (Point 6).

$$F_{ref}^1 = (1 - \beta) F_{ref}^0 \quad \text{Eq. 2-3}$$

The developed models were calibrated using experimental results. The bilinear model was calibrated using results of tests on steel beam column subassemblies. The pinching model was calibrated using results of tests on RC columns and plywood shear walls. A sensitivity study was conducted on the peak-oriented model to investigate the effect of model parameters on global response.

2.4 Sivaselvan and Reinhorn (2000) [10]

All the models discussed above have piece-wise linear force deformation response. Sivaselvan and Reinhorn developed a Smooth Hysteretic Model (SHM) based on the assembly of springs shown in Figure 2-11 to model different nonlinear and degrading behavior of structural components. The in-series assembly of Spring 2 and Spring 3 are connected in parallel with Spring 1 and Spring 4. The Post-Yielding spring models the post-yield hardening effect. The Slip-Lock spring captures crack-closure and bolt slipping. The Gap-Closing spring models the extra stiffening at large deformations which happens, for instance, when expansion joints of a bridge are closed. The

strength and stiffness deterioration are captured in formulation of response by the Hysteretic Spring (Spring 2). Figure 2-12 shows how stiffness and strength degrade in this model. The stiffness degradation is governed by the assumption that force deformation curve at unloading targets a pivot point. The unloading stiffness is calculated according to Eq. 2-4.

$$K_{cur} = R_K K_0 = \frac{M_{cur} + \alpha M_y}{K_0 \varphi_{cur} + \alpha M_y} K_0 \qquad \text{Eq. 2-4}$$

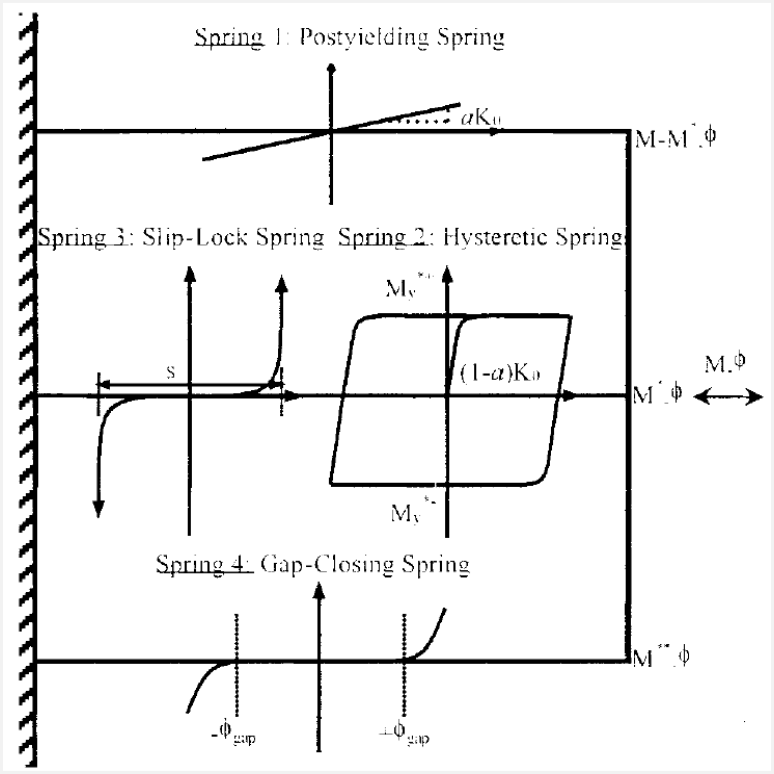

Figure 2-11 SHM model developed by Sivaselvan and Reinhorn

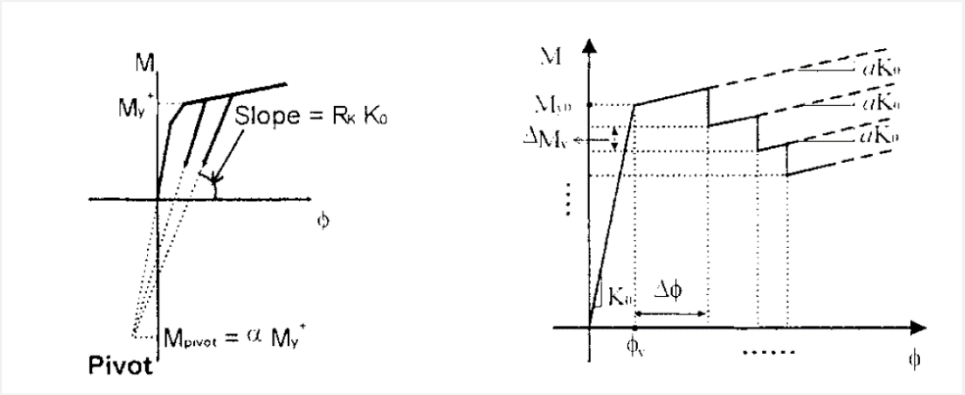

Figure 2-12 Strength and stiffness degradation of hysteretic spring in the SHM model by Sivaselvan and Reinhorn

In Eq. 2-4, αM_y is the ordinate of the Pivot, and α is parameter of the model controlling stiffness degradation. φ_{cur} and M_{cur} are deformation and force at the current state. Strength degradation is governed by Eq. 2-5. Both dissipated energy and nonlinear deformation deteriorate strength independently.

$$M_y^{+/-} = M_{y0}^{+/-}\left[1-\left(\frac{\varphi_{max}^{+/-}}{\varphi_u^{+/-}}\right)^{\frac{1}{\beta_1}}\right]\left[1-\frac{\beta_2}{1-\beta_2}\frac{H}{H_{ult}}\right] \qquad \text{Eq. 2-5}$$

In Eq. 2-5, $\varphi_{max}^{+/-}$ is the maximum hysteretic deformation, and $\varphi_u^{+/-}$ is the maximum deformation capacity of the element being modeled, in positive and negative directions. H_{ult} is the maximum energy dissipated by the element when pushed monotonically up to φ_u, and H is the hysteretic energy dissipated, computed by integrating the energy quotient of Eq. 2-6.

$$\Delta H = \left[\frac{M+(M+\Delta M)}{2}\right]\left(\Delta\varphi - \frac{\Delta M}{R_K K_0}\right) \qquad \text{Eq. 2-6}$$

Parameters β_1 and β_2 control the rate of deterioration. Figure 2-13 shows the analytical and experimental response of a steel beam to column joint, using the model developed by Sivaselvan and Reinhorn.

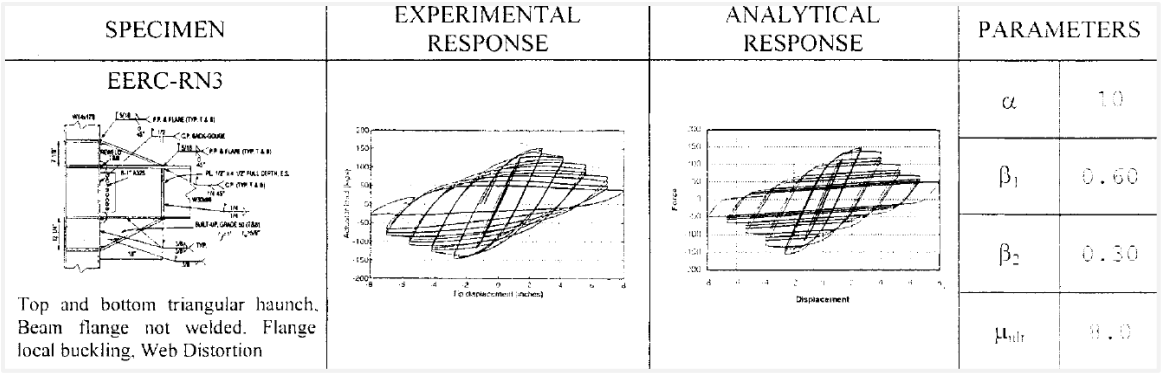

Figure 2-13 Comparison of predicted and measured force deformation response of a joint by Sivaselvan and Reinhorn

2.5 Conclusion

The models discussed above are developed to be used for concentrated springs, that model force deformation response of structural components in one direction only. These models can be used in a simple shear wall model, e.g., the model in Figure 3-1 or Figure 5-2 (c) in which the nonlinear action is lumped in one spring. Modeling of structural walls has evolved such that common practice is to use a model based on fiber sections where a combination of uniaxial elements captures the flexural/axial response. A fiber section model that can capture the strength and stiffness degradation of shear walls and is compatible with backbone curves in the literature has yet to be developed. The objective of this project is to develop such a model.

Chapter 3 Modeling flexure-controlled shear walls to capture strength loss

3.1 Nonlinear models of RC structural walls

A simple model to capture nonlinear behavior of structural walls consists of an elastic beam-column element and nonlinear springs, located at the centerline of element's cross section as shown in Figure 3-1. The black flexural springs account for the nonlinear flexural response. An initial linear force-deformation response may be added for numerical purposes. In this case, the flexural stiffness of the elastic beam-column element is adjusted accordingly. The backbone of nonlinear flexural springs is obtained by computing the moment curvature diagram of the wall section. This analysis is straightforward if the axial load is assumed to be constant. If the axial load is fluctuating, as in a frame wall system, the process of computing the backbone curve and assigning it to the flexural springs becomes complicated. The gray flexural spring at the base, in series with other components, accounts for slippage and extension of bars at the support.

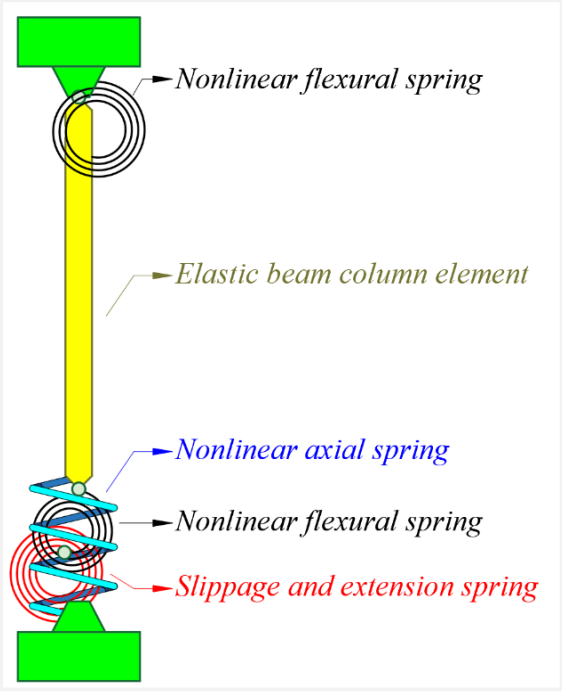

Figure 3-1 A simple shear wall model

Due to small tensile strength of concrete, axial stiffness of RC walls is significantly different in a net compressive axial load than in a net tensile axial load. To consider this behavior, the blue spring of Figure 3-1 is added to the assembly. Appropriate values for axial stiffness are assigned to the elastic beam-column element, and the nonlinear axial spring so that the combination in series of these two components captures the overall axial response of the wall.

The shear response of the wall, if assumed linear, can be captured by the shear stiffness of the elastic beam-column element. If the shear response is nonlinear, a horizontal spring replaces the elastic shear stiffness of the beam-column element. To have a finer model that accounts for shear sliding, a simple shear-slip model at the base can be incorporated. For each of these nonlinear springs, hysteretic force deformation curves are formulated using data from experimental study on similar specimens, or finite element analyses.

Takayanagi and Schnobrich (1979) [12] made the mechanical model of Figure 3-2 to investigate the failure mechanism and nonlinear dynamic response of a ten-story coupled wall system. The wall piers are divided into sub-elements, and finer mesh is used for the bottom stories, where more inelastic deformation is expected to occur.

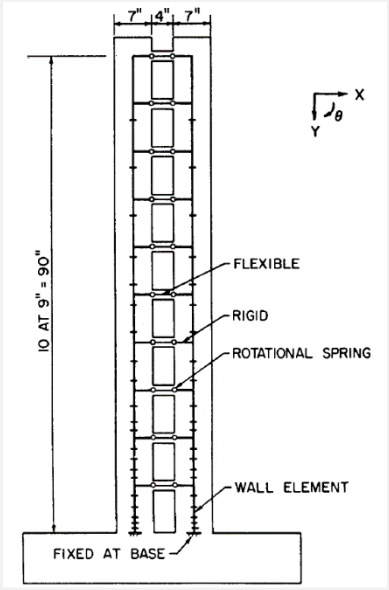

Figure 3-2 Coupled wall model by Takayanagi and Schnobrich

The interaction of axial and flexural load is considered by formulating the force deformation relationship of wall sub – elements according to Eq. 3-1.

$$\begin{bmatrix} m = M(\varphi, & n) \\ n = N(\varphi, & \varepsilon) \end{bmatrix} \qquad \text{Eq. 3-1}$$

Moment is function of axial load, n, and curvature, φ. The axial load is a function of curvature and axial deformation, ε. The stiffness matrix of the wall sub-element, composed by taking partial derivatives of Eq. 3-1, is shown in Eq. 3-2.

$$\begin{bmatrix} \Delta M \\ \Delta N \end{bmatrix} = \begin{bmatrix} \dfrac{\partial M}{\partial \varphi} + \dfrac{\partial M}{\partial n}\dfrac{\partial N}{\partial \varphi} & \dfrac{\partial M}{\partial n}\dfrac{\partial N}{\partial \varepsilon} \\ \dfrac{\partial N}{\partial \varphi} & \dfrac{\partial N}{\partial \varepsilon} \end{bmatrix} \begin{bmatrix} \Delta \varphi \\ \Delta \varepsilon \end{bmatrix} \qquad \text{Eq. 3-2}$$

If the ratio of incremental axial load to the incremental moment does not change significantly, the stiffness matrix of Eq. 3-2 can be turned into a symmetric matrix to increase the efficiency of the solution algorithm. Computation of $\partial M/\partial \varphi$ in Eq. 3-2 needs the moment-curvature diagrams of the wall section to be obtained for different levels of axial loads. Transitions between moment

curvature curves of Figure 3-3 are introduced to formulate the effect of varying axial load on the flexural response.

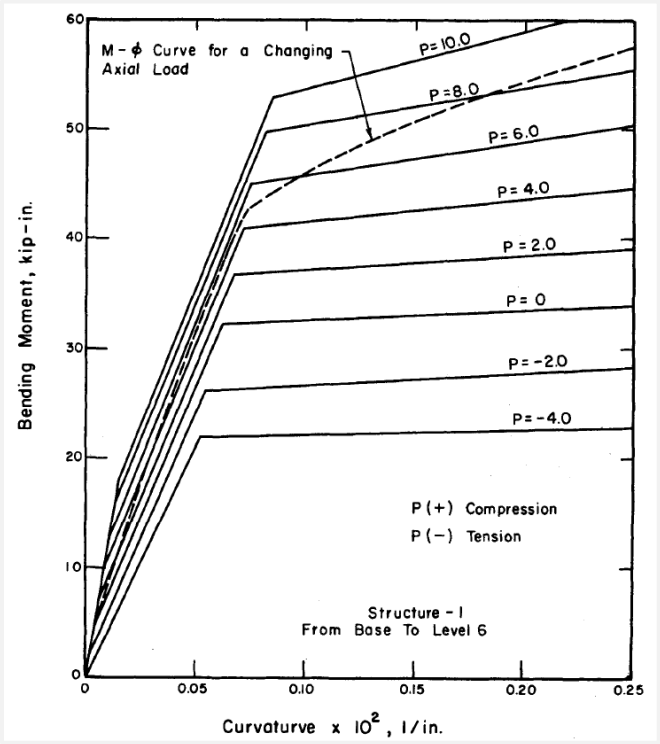

Figure 3-3 Idealized moment curvature relationships of wall segments by Takayanagi and Schnobrich

To analyze a seven story RC frame-wall building tested as part of the US-Japan cooperative research program, Kabeyasawa et al. (1984) [13] developed the TVLEM to model the structural walls. Figure 3-4 shows the plan view of the barbell shaped wall used as the lateral force resisting system in the building.

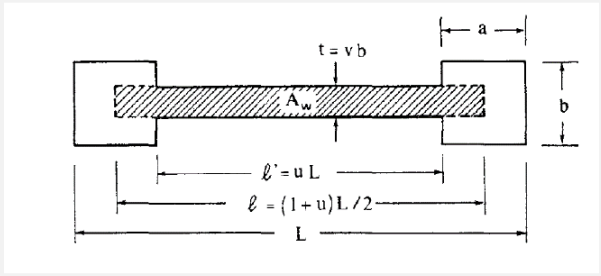

Figure 3-4 Plan view of the lateral force resisting system modelled by Kabeyasawa et al. (1984)

Figure 3-5 shows the layout of their proposed model, which consists of two rigid beams at the top and bottom that enforces a linear varying strain over the section, and three elements to model the boundary columns and the inside panel. The side columns are uniaxial springs. The middle column is a combination of rotational, axial and shear springs. Empirical nonlinear force-deformation relations constitute the response of each spring.

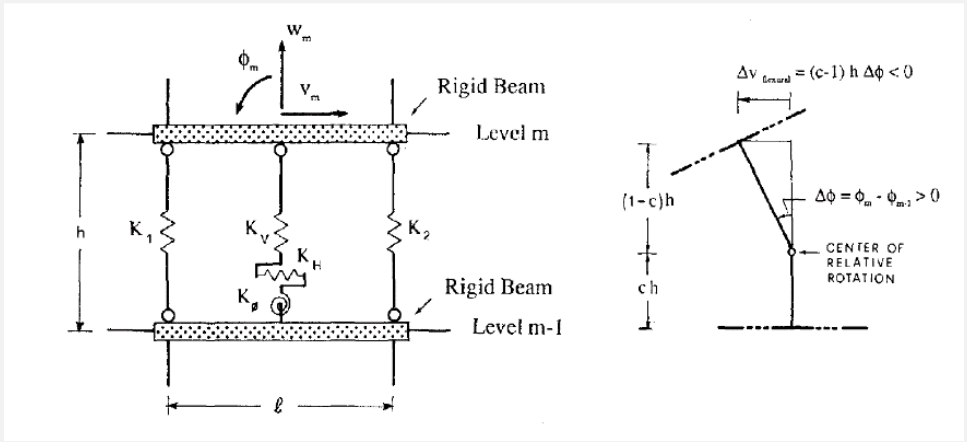

Figure 3-5 TVLEM proposed by Kabeyasawa et al. (1984)

Figure 3-6 describes the Axial Stiffness Hysteretic Model (ASHM) assigned to the axial springs, in the two boundary columns and the middle column. Figure 3-7 describes the Origin Oriented Hysteretic Model (OOHM) assigned to the flexural, and shear springs in the middle column. The empirical cyclic rules and many other assumptions are determined based on experimental tests on other smaller specimens. The parameters in the figure are calculated using the geometry of the wall, reinforcement ratio, and the strength of the material.

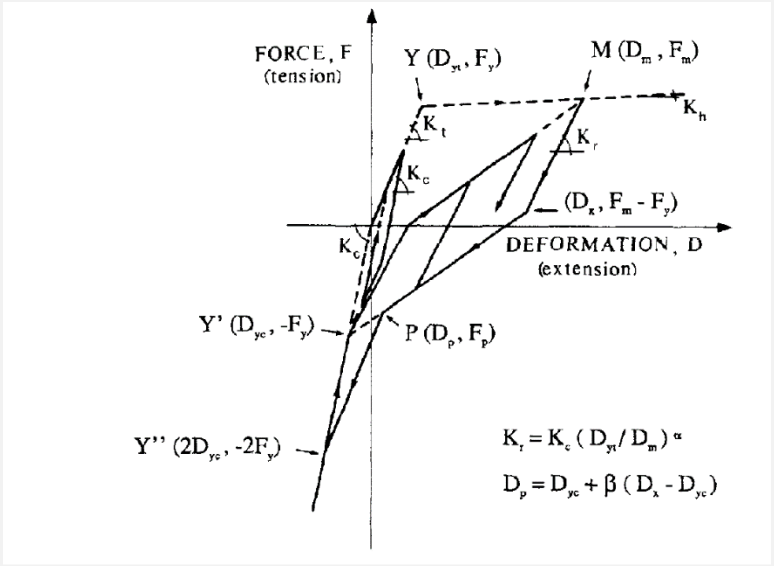

Figure 3-6 Cyclic force deformation relationship used for ASHM in TVLE model

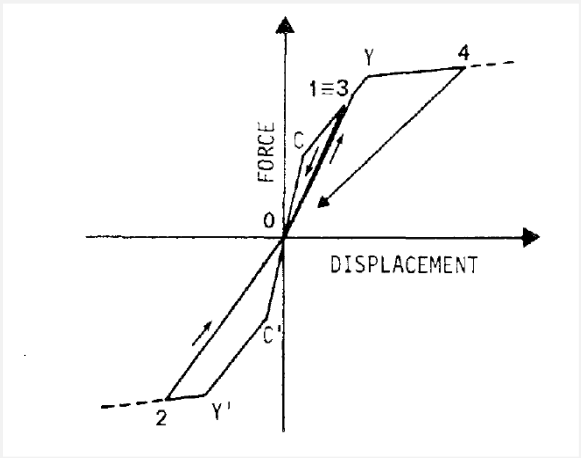

Figure 3-7 Cyclic force deformation relationship used for OOHM in TVLE model to capture the shear response

Vulcano and Bertero (1987) [14] believed that the model developed by Kabeyasawa et al. did not consider deformation compatibility between the central panel and the boundary columns in assigning the properties of the central panel's flexural spring. To further improve the TVLE model, they obtained the moment curvature of the central panel using the computer program UNCOLA, and considering deformation compatibility. A trilinear curve was fitted on the moment curvature diagram, and properties of the flexural spring were assigned. In addition, they used the assembly

of components, shown in Figure 3-8, that has the advantage of modeling bond deterioration and reappearance of contact stress between steel and concrete. The length λh denotes the length over which the bond stress between steel bars and concrete has been deteriorated.

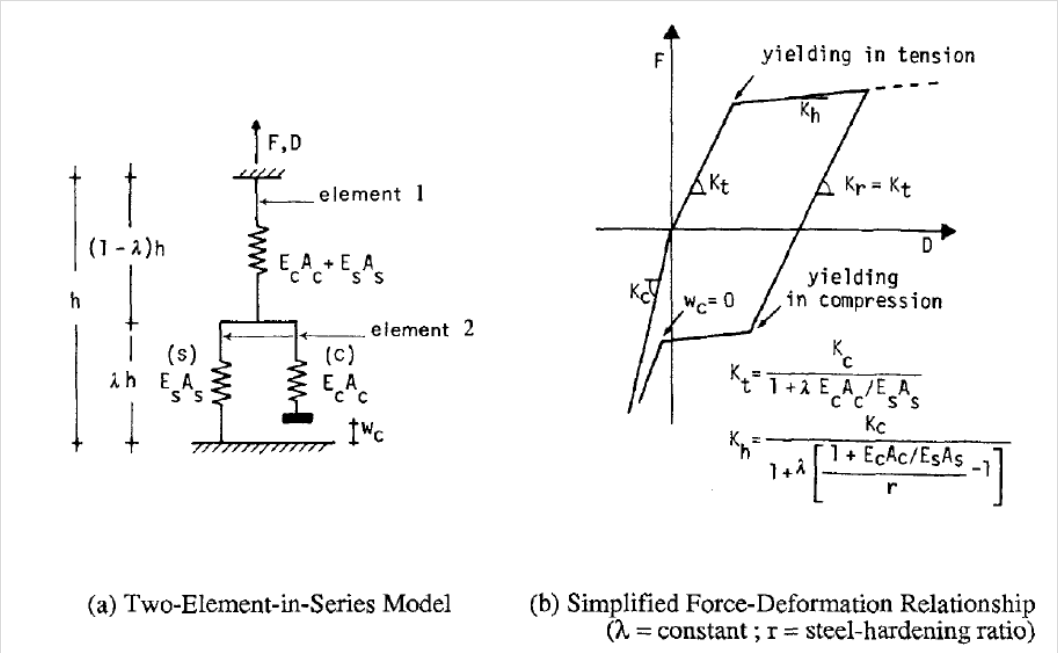

Figure 3-8 Axial Stiffness Hysteresis Model proposed by Vulcano and Bertero (1987)

Although the overall response predicted by the model is in reasonable agreement with test results, the flexural spring representing the flexural behavior of the central panel is troublesome. Computation of the properties of this flexural spring requires assuming a constant axial load on the central panel. It may be acceptable for isolated cantilever walls to assume that the axial load is constant, but the contribution of the central panel's axial load to the total axial load changes.

To modify the model by having a better compatibility of the components, Vulcano et al. (1988) [15] proposed the Multiple Vertical Line Element (MVLE) model, shown in Figure 3-9. The multiple (more than two) vertical lines in the middle overwrites the flexural spring at the base. The

shear spring is elevated to height *ch* in this model. By assigning different valued for c ($0 \leq c \leq 1$), different variations of curvature over the element height (with no change in sign) can be achieved.

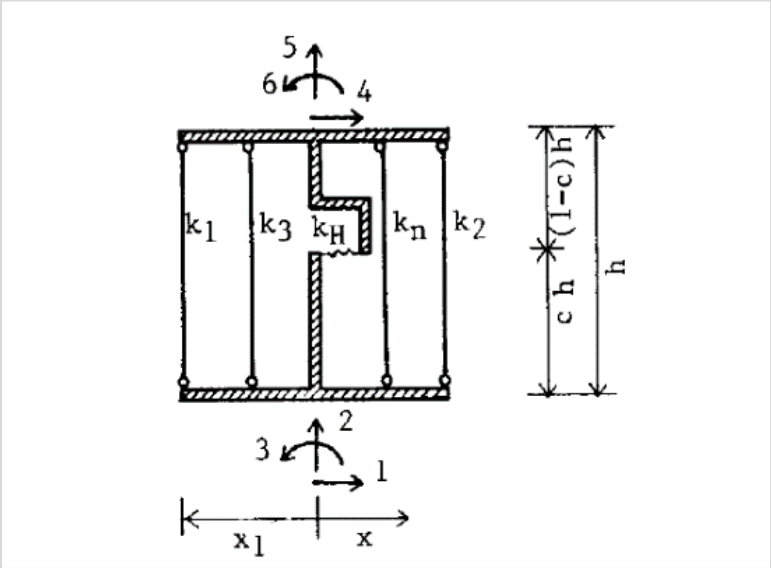

Figure 3-9 Multiple Vertical Line (MVL) element proposed by Vulcano et al.(1988)

Multiple researchers have worked on the efficiency and accuracy of the MVL element model, including Vidic et al. (1989) and Fischinger et al. (1990) [17], that did an analytical study on a 2.4-meter, one-story prototype tested at Tsinghua university in Beijing. The wall cross section is shown in Figure 3-10.

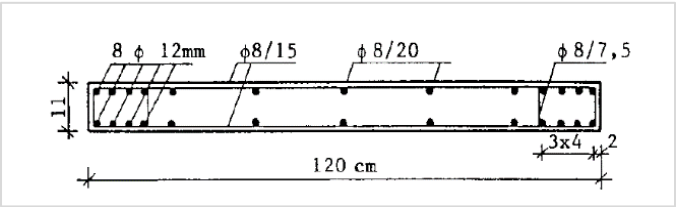

Figure 3-10 Cross section of the wall tested by Zhou (1988) [16] at Tsinghua university in Beijing

Figure 3-11 shows the comparison of the test lateral force versus top displacement, with analytical results obtained by different modeling approaches. The curves shown in the figure are envelopes of cyclic force deformation curves.

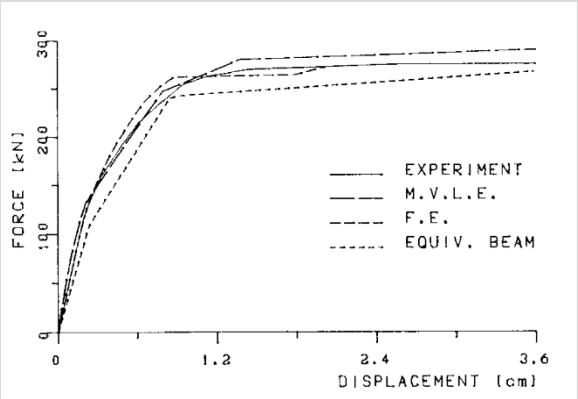

Figure 3-11 Comparison of test results and analytical results by Fischinger et al. (1990) and Vidic et al. (1989)

Orakcal and Wallace (2004) [18][19][20] used the Multi Vertical Line Element model with two steel and concrete fibers in parallel for each generic uniaxial element. The model proposed by Chang and Mander (1994) [30] was used for the concrete material, and a modified version of Menegotto-Pinto (1973) [47][30] for the steel reinforcement. These two are still state of the art models for reinforcing steel and concrete material. The MVLEM used in their study relates the flexural response directly to the material properties, without the need to employ any empirical rules.

They showed that using these two models for the material, the MVLE model can accurately predict the hysteretic flexural force-deformation response of slender walls. As part of their study, they calibrated the model against tests on planar and flanged RC wall. A sensitivity analysis on the element and material parameters was performed to evaluate the effect of these parameters on response of the wall at different states.

3.2 Selected shear wall model: Multiple Vertical Line Element Model

Analytical research has proven the effectiveness and reliability of the MVLE model in analyzing reinforced concrete structural walls. The overall nonlinear response of the structure predicted by

the model is in reasonable agreement with test results. The model captures many aspects of the structural walls including the effect of fluctuating axial load on the flexural strength, and the shift of the neutral axis in cyclic loading. The latter is especially important when performance of connecting elements (e.g., slab elements and coupling beams) matters in the analysis. Furthermore, the constituent uniaxial elements capture the distribution of the vertical stresses on the wall section. This is significant for the purpose of this work because, as will be explained in Chapter 4, the strength loss parameters are determined based on the force-wise compression zone depth (i.e., the depth of section under compressive vertical stress).

It is well known that the shear force-deformation behavior of structural walls at loading stages after yielding is nonlinear due to flexural cracks and loss of aggregate interlock. This is true even for flexure-controlled walls where the maximum shear demand is less than the ultimate shear capacity (Massone and Wallace (2004) [55]). The shear force versus shear distortion diagram for the bottom segment of specimen RW2 tested by Thomsen and Wallace (1995) [22][21], shown in Figure 3-12, serves as an example. The MVLE model originally developed by Vulcano et al. utilizes a nonlinear shear material for the horizontal springs, but the shear force-deformation nonlinearity is uncoupled from the flexural response. Although a horizontal shear spring whose properties depend on element's curvature/axial deformation can provide a solution for this problem but working on shear response is beyond the scope of this dissertation, and the element developed in this study to capture stiffness and strength deterioration has an elastic linear shear spring. This approach will not have a significant impact on the predicted overall response as the behavior of the structures simulated by this model is dominated by the flexural action.

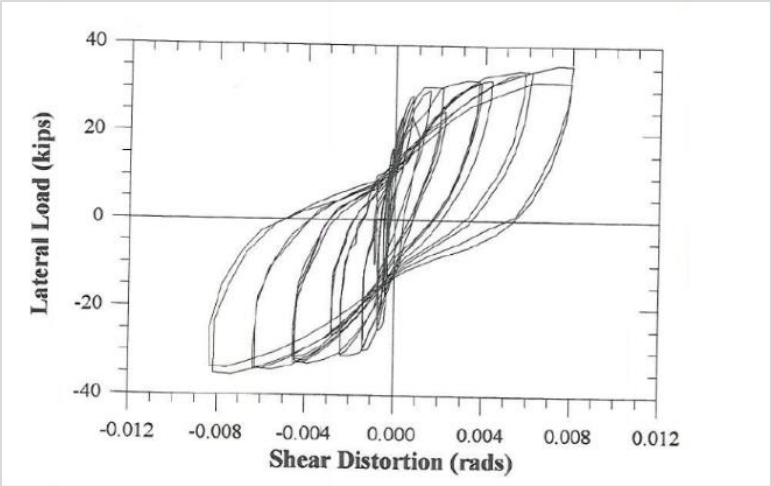

Figure 3-12 Shear force versus shear distortion response of the bottom segment of Specimen RW2 tested by Thomsen and Wallace (1995)

3.3 Description of the model

Figure 3-13 shows the deformed and undeformed layout of an MVL element used in this study. The element is composed of m uniaxial tress members that capture the axial-flexural response. Each uniaxial member, labeled i, is made of concrete and steel material with areas A_c^i and A_s^i, respectively, that constitute the portion of the cross section the fiber represents.

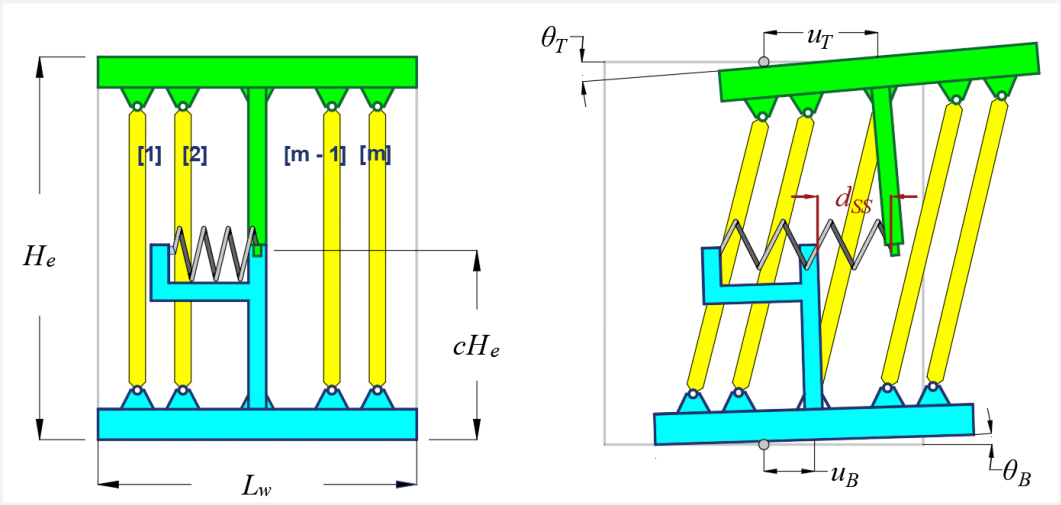

Figure 3-13 Undeformed and deformed configuration of an MVL element

In a 2D space, nodes at the top and bottom of the element have three degrees of freedom each. The internal force of the element is computed based on the nodal displacements. The full formulation of element's vector of internal forces can be found in literature. The important components that need to be discussed here, and will be referred to later, are the shear force, top moment, bottom moment, and the moment at the location of the shear hinge.

Eq. 3-3 gives the internal shear force across the element base on element's nodal displacements and stiffness of the shear spring. Note that since the shear response is assumed to be linear elastic, the element's shear force is stiffness of the shear spring, K_h, times the displacement across the shear spring, d_{SS}.

$$F_{11} = V = K_h d_{SS} = K_h[u_B - cH_e\theta_B - (1-c)H_e\theta_T - u_T] \quad \text{Eq. 3-3}$$

The internal moment at the location of the horizontal spring (at height cH_e from the bottom of the element) is given in Eq. 3-4. Since the moment arm of the shear force in the horizontal spring is zero at this point, the moment at this point is purely due to the uniaxial struts.

$$M_{SS} = \sum_{i=0}^{m} A_c^i \sigma_c^i(\varepsilon^i) x^i + A_s^i \sigma_s^i(\varepsilon^i)\, x^i \quad \text{Eq. 3-4}$$

In Eq. 3-4, m is the number of fibers in the section, and x^i is the local coordinate of each uniaxial element, and ε^i is the total strain of each fiber.

The shear force remains constant in the element (i.e., no lateral force across the element height is assumed). So, the moment diagram is linear with the maximum and minimum moments at the top and bottom. Eq. 3-5 turns the moment at the top of the element.

$$M_T = M_{SS} - V(1-c)H_e = \sum_{i=0}^{m} A_c^i \sigma_c^i + A_s^i \sigma_s^i - K_h[cH_e\theta_B + (1-c)H_e\theta_B + u_T - u_B] \quad \text{Eq. 3-5}$$

The bottom moment of the element is derived in Eq. 3-6 using equilibrium of forces.

$$M_B = M_{SS} + VcH_e = \sum_{i=0}^{m} A_c^i \sigma_c^i + A_s^i \sigma_s^i - K_h[cH_e\theta_B + (1-c)H_e\theta_B + u_T - u_B] \quad \text{Eq. 3-6}$$

As discussed in 3.1, different values of c produce different distribution of curvature across the element. The average curvature is calculated according to Eq. 3-7.

$$\varphi_e = \frac{\theta_T - \theta_B}{H_e} \quad \text{Eq. 3-7}$$

3.4 Element's backbone curve and deformation parameters of strength loss

ASCE 41 (2017) [2] classifies structural actions of elements into force-controlled and deformation-controlled categories. Deformation controlled actions, such as flexural response in flexure-controlled structural walls, are assigned a backbone curve that specifies the envelope of hysteretic force deformation of the element for that action.

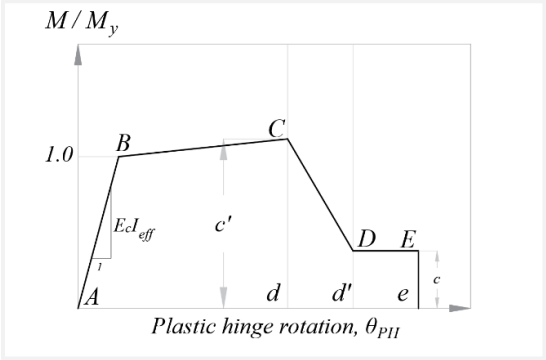

Figure 3-14 Backbone curve of the flexural action of structural walls

Figure 3-14 shows the backbone curve of reinforced concrete structural walls controlled by flexure. The horizontal axis of the backbone curve is the rotation of the plastic hinge. The plastic hinge, shown in Figure 3-15, is the segment of the wall with height l_p over the critical section, where most of nonlinearity occurs.

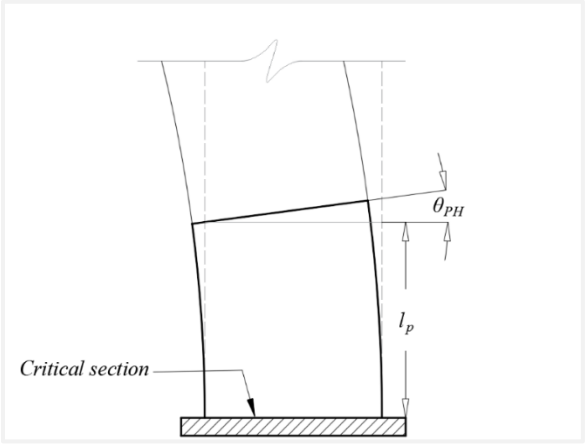

Figure 3-15 Plastic hinge of RC structural walls

ASCE 41 sets l_p equal to half of the flexural depth of the element. A more in-depth discussion regarding appropriate values to be used for the height of the plastic hinge is presented in Chapter 5. In an analytical model of the wall that has only one MVL element used over the plastic hinge, the total rotation of the plastic hinge, θ_{PH}, is calculated from Eq. 3-8.

$$\theta_{PH} = \theta_T - \theta_B = \varphi_e H_e, \qquad H_e = l_p \qquad \text{Eq. 3-8}$$

In Eq. 3-8, φ_e is element's average curvature, and H_e is the height of the element used for the plastic hinge.

The vertical axis of the backbone curve, in Figure 3-14, is the moment normalized by the yield moment. Note that moment varies over element height with a gradient equal to the shear force across the element. Because the height of the plastic hinge is small compared to the effective height of the structure, it would be acceptable to use the moment at the top of the plastic hinge (Eq. 3-5), bottom of the plastic hinge (Eq. 3-6), or anywhere in between for computation purposes. In formulation of the element, the moment at the location of the shear spring, M_{SS} in Eq. 3-4, is assumed for the backbone curve's vertical axis.

The previous work on the reliability and effectiveness of the MVL element has shown that by using the actual strength of the steel, and the test day strength of the concrete material in the model, the backbone curve is automatically captured at deformations smaller than initiation of strength loss (segments AB and BC). Beyond point C, when plastic hinge rotation exceeds d, segment CD of the backbone curve determines the strength loss scheme. Over this segment, a force increment is linearly correlated with an increment of the plastic hinge rotation.

$$dM_{SS} \propto d\theta_{PH} \qquad \text{Eq. 3-9}$$

Inserting Eq. 3-8 into Eq. 3-9 , moment increments are linearly correlated with curvature increments.

$$dM_{SS} \propto d\varphi_e \qquad \text{Eq. 3-10}$$

As discussed before, Eq. 3-4 gives moment at the shear spring, M_{SS}, which is entirely due to the stresses in the various fibers, which are a function of fiber strain. Strain of a fiber in an MVL element (generally any element with a fiber-discretized section whose deformation geometry ignores the second and higher order terms of deflection) is a combination of the axial deformation, and element curvature per Eq. 3-11, and shown in Figure 3-16.

$$\varepsilon^i = \varphi_e x_i + \frac{dv}{H_e} = \varepsilon_1^i + \varepsilon_2^i, \qquad dv = v_{top} - v_{bot}, \qquad \varphi_e = \frac{\theta_{top} - \theta_{bot}}{H_e} \qquad \text{Eq. 3-11}$$

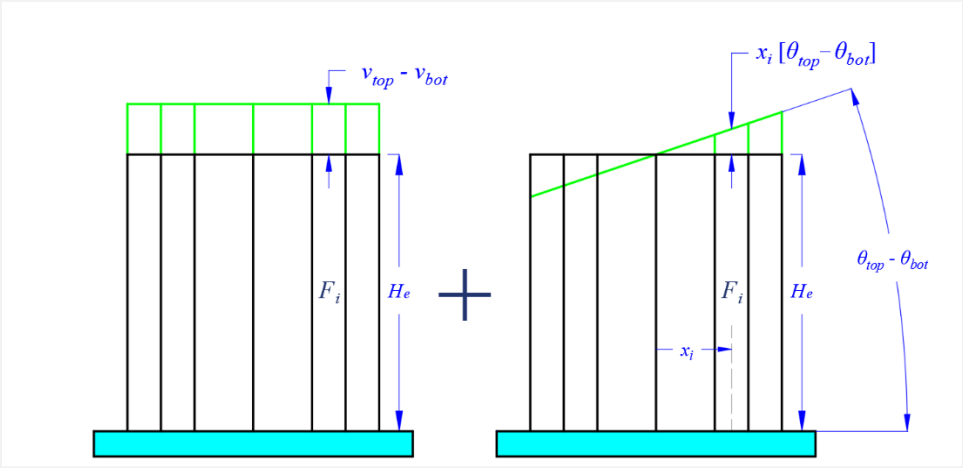

Figure 3-16 Total strain of fiber is the summation of axial strain and flexural strain

In Eq. 3-11, x_i is the local coordinate of the fiber. The strain caused by element curvature is labeled ε_1, and the strain caused by element axial deformation is labeled ε_2. From now, ε_1 is referred to as the flexural strain, and ε_2 is referred to as the axial strain. Eq. 3-12 combines Eq. 3-4 and Eq. 3-11.

$$M_{SS} = \sum_{i=0}^{m} A_c^i \sigma_c^i(\varepsilon_1 + \varepsilon_2) + A_s^i \sigma_s^i(\varepsilon_1 + \varepsilon_2)$$ Eq. 3-12

Segment CD of the backbone curve, relates the rate of strength degradation to the curvature increment only, as shown in Eq. 3-10. With area fibers being constant, this means that segment CD related the materials rate of stress degradation to the curvature increment only.

$$dM_{SS} = \sum_{i=0}^{m} A_c^i d\sigma_c^i \left(d\varphi_e = \frac{d\varepsilon_1}{x_i}\right) + A_s^i d\sigma_s^i \left(d\varphi_e = \frac{d\varepsilon_1}{x_i}\right)$$ Eq. 3-13

To build a model that maintains the properties of the element prior to strength loss, and captures the backbone curve after initiation of strength loss, the total strain is decomposed into flexural strain and axial strain as independent variables of stress, as shown in Eq. 3-14.

$$M_{SS} = \sum_{i=0}^{m} A_c^i \sigma_c^i(\varepsilon_1, \quad \varepsilon_2) + A_s^i \sigma_s^i(\varepsilon_1, \quad \varepsilon_2)$$ Eq. 3-14

Formulation of stress as a function of independent variables ε_1, and ε_2 is explained in 3.5.

3.5 Formulation of the material strain stress equations

Figure 3-17 shows the simplified strain stress curve of a steel material under monotonic compressive and tensile loading.

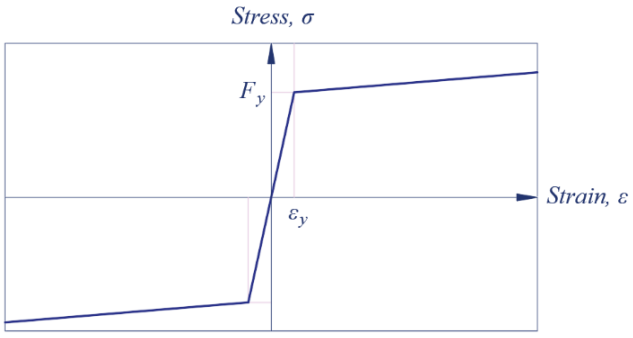

Figure 3-17 Simplified strain stress curve for a steel material loaded from [0, 0]

Starting to load from zero strain and stress ($\varepsilon = 0$ and $\sigma = 0$), material remains elastic until the yield point ($\varepsilon = \pm\varepsilon_y$ and $\sigma = \pm\sigma_y$). Beyond the yield point, strain hardening occurs with a constant post-yield tangent equal to $E_{sh} = bE_s$. Eq. 3-15 show the strain stress equations, over the elastic segment and stain hardening branches respectively.

$$\sigma = E_s\varepsilon$$

$$\sigma = E_{sh}(\varepsilon - \varepsilon_y) + F_y, \qquad \sigma = E_{sh}(\varepsilon + \varepsilon_y) - F_y$$

Eq. 3-15

By decomposing the total strain, ε, into flexural strain, ε_1, and axial strains, ε_2, the 2D strain-stress curve of Figure 3-17 is converted to the 3D strain-strain-stress curve of Figure 3-18.

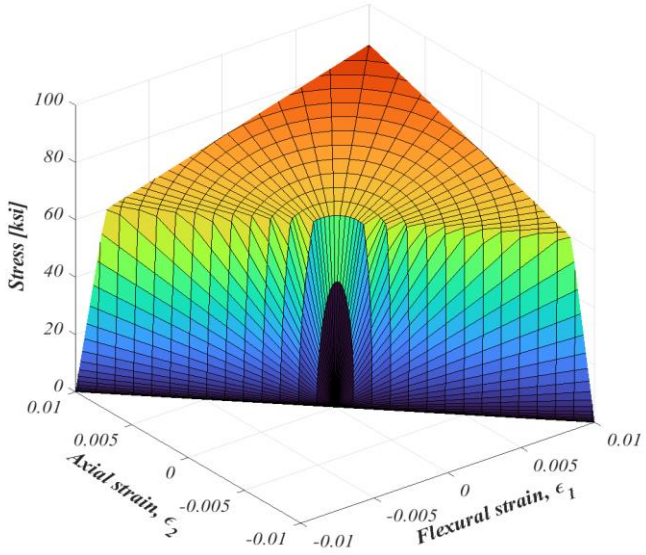

Figure 3-18 Simplified strain - strain - stress curve for steel material loaded from [0, 0]

Note that stress in Figure 3-18 now varies over the strain-strain plane of Figure 3-19.

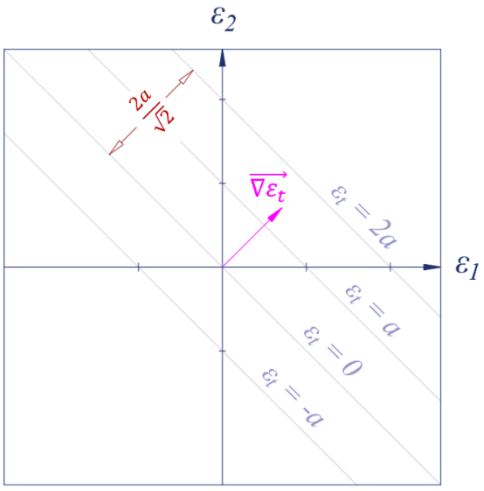

Figure 3-19 Flexural strain - axial strain plane ($\varepsilon_1 - \varepsilon_2$ plane)

On this plane, points with the same total strain lie on lines oriented at a *45°* angle.

$$\varepsilon_1 + \varepsilon_2 = a, \qquad \varepsilon_2 = a - \varepsilon_1$$

With equal total strain, all points above these lines have the same stress. Vector $\overrightarrow{\nabla\varepsilon_t}$ in Figure 3-19 shows the direction of change in total strain, and the gradient of stress.

$$\overrightarrow{\nabla\varepsilon_t} = \frac{\partial e}{\partial \varepsilon_1}\overrightarrow{e_1} + \frac{\partial e}{\partial \varepsilon_2}\overrightarrow{e_2} = \begin{bmatrix}1\\1\end{bmatrix} \qquad \text{Eq. 3-16}$$

3.6 Implementing strength degradation of the material

As shown in Figure 3-14, the deformation parameters (Plastic hinge rotations) at the start and end of the strength loss segment are d and d' respectively. With only one element being used for the plastic hinge, the average element curvatures, corresponding to plastic hinge rotation of d and d' are given in Eq. 3-17.

$$\varphi^{d} = \frac{d}{H_e}, \qquad \varphi^{d'} = \frac{d'}{H_e} \qquad \text{Eq. 3-17}$$

In Eq. 3-17 and the following equations, H_e is the height of the plastic hinge. Now consider a steel fiber is located at local coordinate x_i of the cross section shown in Figure 3-20.

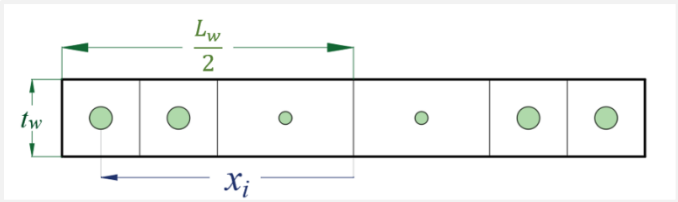

Figure 3-20 Steel fiber at local coordinate x_i of the cross section

The flexural strains, ε_1, due to curvatures of Eq. 3-17 are obtained using the local coordinate of the fiber.

$$\varepsilon_1^{d} = \varphi^{d} x_i = \frac{d}{H_e} x_i, \qquad \varepsilon_1^{d'} = \varphi^{d'} x_i = \frac{d'}{H_e} x_i \qquad \text{Eq. 3-18}$$

Another set of flexural strains are calculated in Eq. 3-19 for the backbone curve of the element in the opposite direction.

$$\varepsilon_1^{-d} = \varphi^{-d} x_i = \frac{-d}{H_e} x_i, \qquad \varepsilon_1^{-d'} = \varphi^{-d'} x_i = \frac{-d'}{H_e} x_i \qquad \text{Eq. 3-19}$$

The flexural strains in Eq. 3-18 and Eq. 3-19 specify regions on the $\varepsilon_1 - \varepsilon_2$ of Figure 3-19, over which the material's strength degrades. These regions are shown in Figure 3-21.

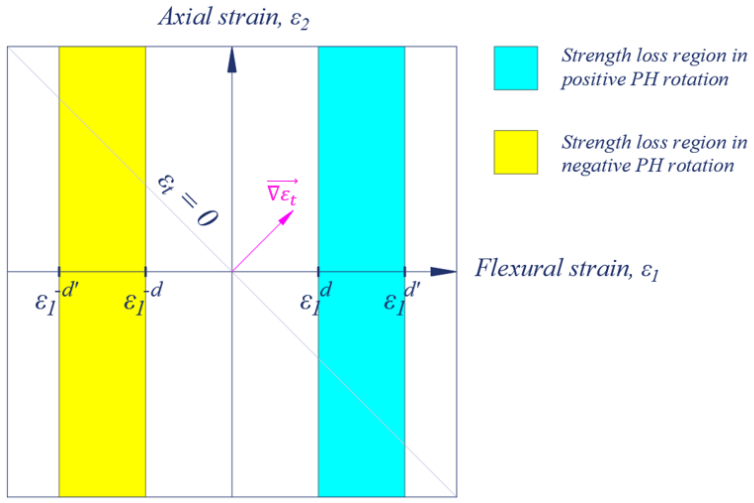

Figure 3-21 Strength loss regions on ε_1 - ε_2 plane

With a uniform stress degradation over the span of flexural strains highlighted in Figure 3-21 followed by a constant residual stress, the strain-strain-stress curve of Figure 3-18 is converted into the strain-strain-stress curve in Figure 3-22. This figure corresponds to a typical steel material with yield stress of 60 ksi, yield strain of 0.002, and flexural strains of 0.01 and 0.02 corresponding to the strength degradation segment of the element backbone curve, for both negative and positive moment. In a different view angle, Figure 3-23 shows how the strength degradation is captured only over the strength loss regions of the $\varepsilon_1 - \varepsilon_2$ plane shown in Figure 3-21. By adopting this formulation, the material's stress degradation is compatible with element's strength degradation. Note that this would not be the case if the total strain was used as the parameter controlling the strength degradation of the material.

Only the tensile action is plotted in Figure 3-22 and Figure 3-23 for clarity. The stress degradation in tension is associated with bar rupture in tension, and the stress degradation in compression, not shown in the figures, is associated with buckling of bars in compression. Both stress degradation schemes are assumed to occur uniformly over backbone curve strength loss segment (i.e., Segment CD in Figure 3-14).

Beyond deformation d', and prior to deformation e, backbone curve shows a constant residual strength. To achieve this response, concrete and steel materials are assumed to have a constant residual stress for strain magnitudes larger than $\varepsilon_1^{d'}$. This is implemented for the steel material shown in Figure 3-22 and Figure 3-23.

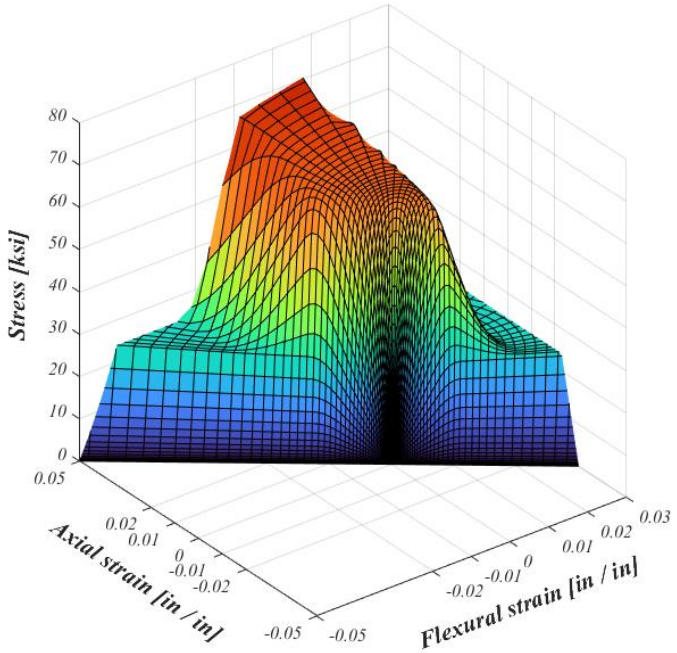

Figure 3-22 Strain-strain-stress curve for a typical steel material with stress degradation

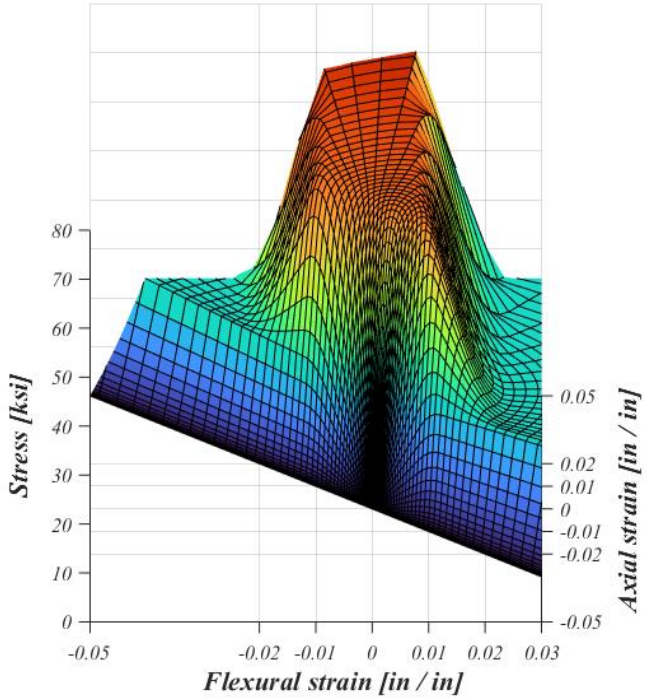

Figure 3-23 Strain-strain-stress curve for a typical steel material with stress degradation

A similar approach is used to formulate the stress equations of the concrete material. The strain-stress equation of the concrete material prior to strength loss is different than steel material's strain-stress equations, yet the governing equations for strength loss are similar for steel and concrete. Furthermore, the concrete materials' strength degradation is assumed to happen only in compression. The tensile stress degradation of concrete is associated with tensile cracking, which happens at load steps prior to yielding.

The kinking at the yield points, evident in Figure 3-17, may cause numerical stability in a nonlinear solution. To avoid this problem, the well-known Menegotto-Pinto equations are used that provide a smooth transition from the elastic branch to the post yield strain hardening segment. Two other transition curves, from strain hardening to the strength degradation segment, and from the strength degradation segment to the constant residual strength region are required if the material captures

strength loss. Implementation of transition curves requires an assumption of the initial strain, where the transition starts. The landing strain, where transition joins the original curve is calculated by assuming a uniform change of tangent. Figure 3-24 shows application of Menegotto-Pinto equations and transition curves in 2D strain stress space. The start and end of transition curves are also specified in this figure with cross signs. Details of calculating the transitions are presented in the appendix (Chapter 7.2). Same approach is used to formulate the transitions in the 3D curves of Figure 3-22 and Figure 3-23.

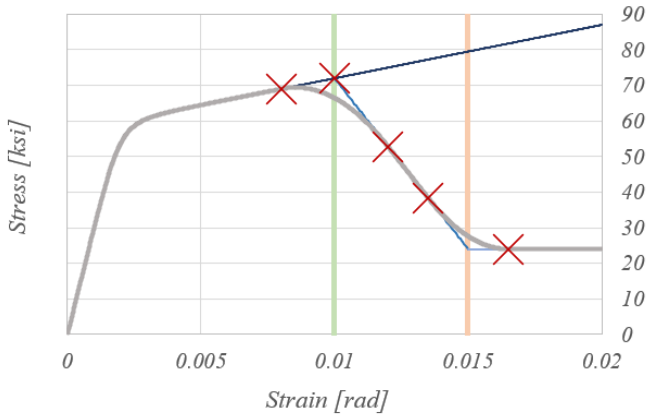

Figure 3-24 Steel strain stress relationship with transition curves

With the material of fibers at other locations showing a consistent stress degradation between flexural strains ε_1^d and $\varepsilon_1^{d'}$, the shear wall's hysteretic flexural force deformation response will by fitted by the correct backbone curve.

3.7 Setting materials' residual stress

Concrete and steel material at the boundary of a cross section is subjected to the highest strains; Therefore, the material at the wall boundaries is assigned smaller residual stresses to produce strength loss. The fibers near the centroid of the cross-section, on the other hand, are likely to be

less damaged. Figure 3-25 shows the deformation of the wall element with compression zone denoted as *C*, and the tensile zone denoted as *T*. With the length of the cross section being L_w, the sum of the compression and tension zone is equal to the total length of the wall, $C + T = L_w$.

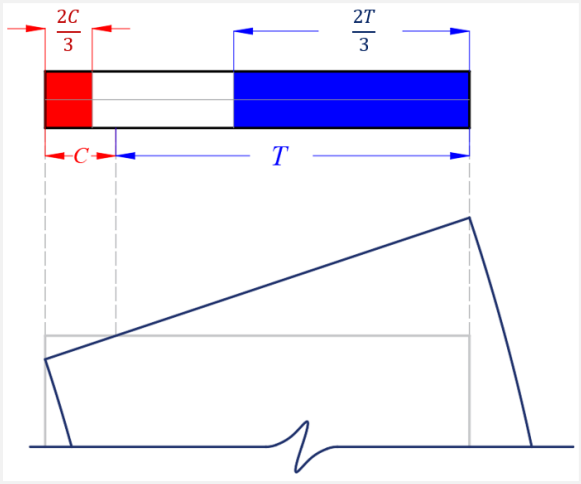

Figure 3-25 deformation of the wall element with denoted compressive and tensile zones

For the proposed model, damage is assumed to occur from the compressive wall edge to $2/3$ of the compression zone depth and from the tensile wall edge to $2/3$ of the tensile zone depth. Damage (or strength loss) is not considered for the material between these zones. With the material of the boundary elements taking more damage, it is assumed that the residual stress is smaller over the boundary regions. Eq. 3-20 is proposed to specify the residual stress of the material over the tensile and compression zones.

$$r(x) = r_A + (r_B - r_A)\left(\frac{x}{L}\right)^n \qquad \text{Eq. 3-20}$$

In Eq. 3-20, r_A is the material residual stress at the face of the wall, r_B is the residual stress at the neutral axis, assumed to be 1.0, L is the depth of the section in Tension / Compression, and x is the location of the material over the Compression / Tension depth. n is a parameter that controls the shape of the curve that determines the residual stress ratio, $r(x)$, over the depth. Figure 3-26 shows

residual stress over section per Eq. 3-20 for different values of n, and an assumed residual stress ratio of 0.2 for the material at the face of the wall.

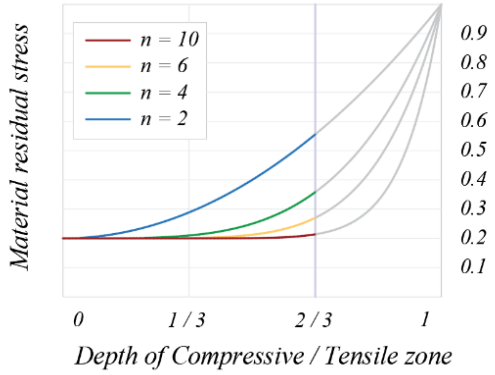

Figure 3-26 Material residual stress over Compression / Tensile zone

The figure also shows the assumed $2/3$ limit over which residual stresses are assigned to the material in fibers. Beyond the $2/3$ limit, both steel and concrete material are assumed to remain intact and behave as regular uniaxial material in 2D strain-stress space.

3.8 Cyclic update of deformation parameter, *d*

Figure 3-27 shows a sample cyclic load deformation and the backbone curve of a shear wall element over the plastic hinge. Vertical axis shows moment at the shear spring of the element, as discussed in 3.4, and the horizontal axis is the plastic hinge rotation, θ_{PH}.

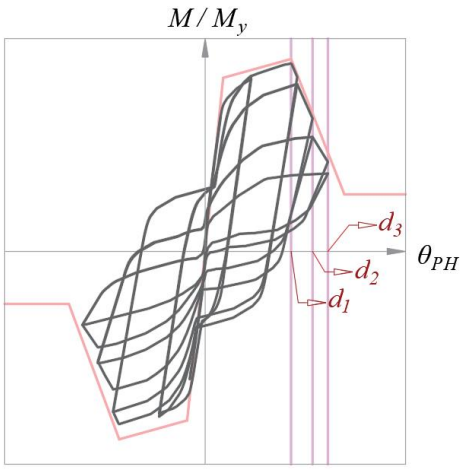

Figure 3-27 Cyclic update of deformation parameter d

Deformation parameter d is initially set equal to d_1. Once d_1 is exceeded in a load step, the element starts following the strength loss curves. Upon an unloading step over the strength loss curve, deformation parameter d is updated to the maximum rotation the element has experienced over the strength loss curves. This updating process ensures that the cyclic force deformation curve is fitted by the element backbone curve. Figure 3-27 shows update of deformation parameter d, to d_2 and d_3 in consecutive unloading steps during the strength loss in positive direction.

3.9 Cyclic Strength and stiffness degradation of the steel material in tension

Assume the steel material of Figure 3-22 starts being loaded from zero strain and stress ($[\varepsilon,\ \sigma] = [0,\ 0]$), and experiences strength degradation in tensile stress. The initial load path, Path A, is indicated by the black arrow on the $\varepsilon_1 - \varepsilon_2$ plane shown in Figure 3-28. The material has a yield stress in tension equal to $F_{y,T}$, and an initial tangent of E_S. The element's backbone curve has the strength loss segment confined by rotations d and d' in the direction of loading, as shown in Figure 3-14. The total strains of the material at plastic hinge rotation of d and d' depend on the load path and the location of the fiber on the cross section. For the load path shown in Figure 3-28, the total strains corresponding to d and d' are denoted by D_1, and R_1, respectively.

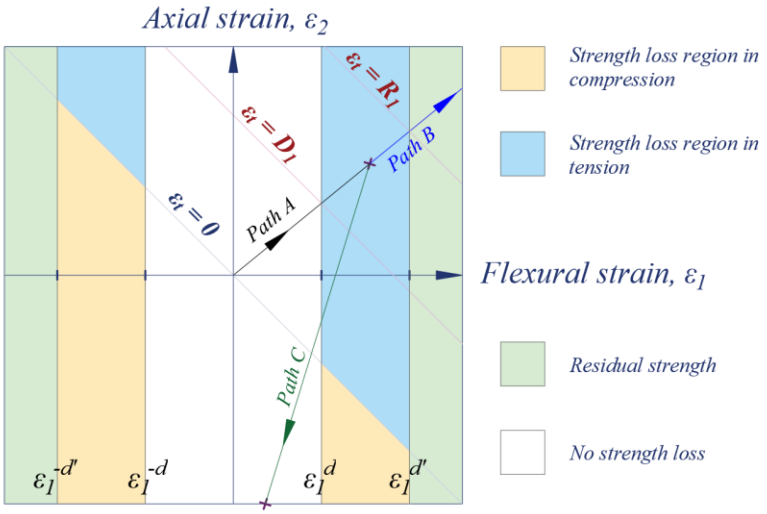

Figure 3-28 Sample load paths of steel material on e_1 - e_2 plane

By plotting stress versus total strain ($\varepsilon_t = \varepsilon_1 + \varepsilon_2$), the strain – stress curve of Figure 3-29 is obtained.

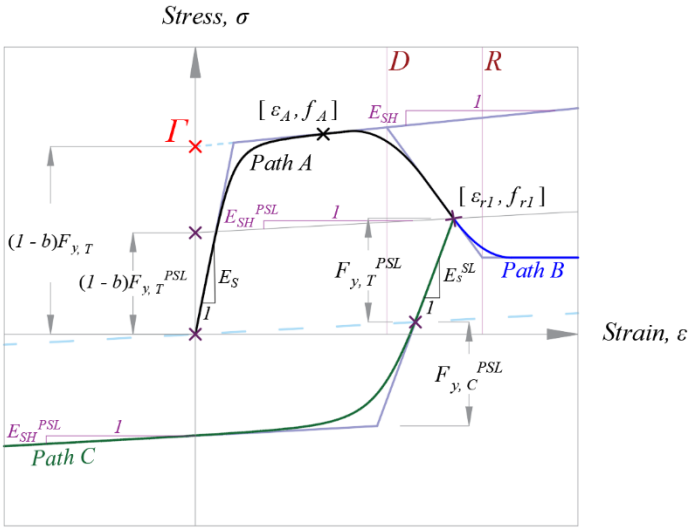

Figure 3-29 Strain - stress curve of steel material with stress degradation in tension

Note that in cyclic loading of steel bars, the yield stress changes due to isotropic hardening. If the material is at a yielding state, such as point $[\varepsilon_A, f_A]$ in Figure 3-29, the yield stress can be derived using the ordinate of point Γ on the strain stress curve shown in Figure 3-29. This method of

obtaining the yield stress will be used later, in Eq. 3-22 to find the Post-Strength-Loss yield stress of the material.

$$(1-b)F_{y,T} = f_A - \varepsilon_A E_{SH}, \qquad F_{y,T} = \frac{f_A - \varepsilon_A b E_S}{1-b} \qquad \text{Eq. 3-21}$$

In Eq. 3-21, E_{SH} is post-yield strain hardening stiffness of the steel bars, and b is the ratio of post-yield tangent, E_{SH}, to the initial tangent, E_S.

If the material follows load *Path B* of Figure 3-28, it will eventually land on residual stress region. The corresponding strain stress curve is shown in Figure 3-29.

Assuming the material is unloaded from a typical point $[\varepsilon_r,\ \sigma_r]$ on the descending branch, and follows load *Path C* of Figure 3-28, the yield stress is updated. The new yield stress, $F_{y,T}^{PSL}$, is calculated using Eq. 3-22.

$$(1-b)F_{y,T}^{PSL} = f_{r1} - \varepsilon_{r1} E_{SH}^{PSL}, \qquad F_{y,T}^{PSL} = \frac{f_{r1} - \varepsilon_{r1} b E_S^{PSL}}{1-b} \qquad \text{Eq. 3-22}$$

Since stress degradation in tension is associated with rupture of bars, the instant unloading stiffness, E_s, must be updated accordingly. It is assumed that stiffness is degraded with the same ratio as the strength. This is stated in Eq. 3-23.

$$\frac{F_{y,T}^{PSL}}{F_{y,T}} = \frac{E_S^{PSL}}{E_S} \qquad \text{Eq. 3-23}$$

By inserting Eq. 3-23 into Eq. 3-22, the updated yield strength of the steel material is derived.

$$F_{y,T}^{PSL} = \frac{f_{r1} - \varepsilon_{r1} b \left(\frac{F_{y,T}^{PSL}}{F_{y,T}}\right) E_S}{1-b}, \qquad F_{y,T}^{PSL} = \frac{f_{r1}}{1 - b + \frac{\varepsilon_{r1} b E_S}{F_{y,T}}} \qquad \text{Eq. 3-24}$$

Once the updated yield strength is derived in Eq. 3-24, the reversal initial stiffness is then calculated by Eq. 3-23.

The yield strength of the material in compression is equal to the updated yield strength in tension, multiplied by a stretching factor to account for isotropic hardening. The rules used in OpenSees material "*Steel02*", shown in Eq. 3-25, are implemented for finding the stretching factor.

$$ST_C = 1 + a_1\left(\frac{\varepsilon_{max} - \varepsilon_{min}}{2a_2\varepsilon_y}\right)^{0.8} = 1 + a_1\left(\frac{\varepsilon_{r1}}{2a_2\varepsilon_y}\right)^{0.8} \quad \text{Eq. 3-25}$$

In Eq. 3-25, a_1 and a_2 are empirical numbers that are input by the user. ε_{max} and ε_{min} are the maximum and minimum strains the material has experienced during load history. The new yield strength in compression is updated per Eq. 3-26.

$$F_{y,C}^{PSL} = ST_C F_{y,C}^{PSL} \quad \text{Eq. 3-26}$$

The reversal and the yielding point in compression, specify the asymptotes of load *Path C*. Assuming another reversal from compression to tension at the end of load *Path C*, the new yield strength in tension is found by calculating the stretching factor in tension.

$$ST_T = 1 + a_3\left(\frac{\varepsilon_{max} - \varepsilon_{max}}{2a_4\varepsilon_y}\right)^{0.8} = 1 + a_3\left(\frac{\varepsilon_{r2} - \varepsilon_{r1}}{2a_4\varepsilon_y}\right)^{0.8} \quad \text{Eq. 3-27}$$

Again, a_3 and a_4 are inputs determined by the user. If material is loaded on *Path D* of Figure 3-30, the plastic hinge rotation does not exceed *d* in positive or negative direction. The strain stress curve of the material on this path is shown in Figure 3-31.

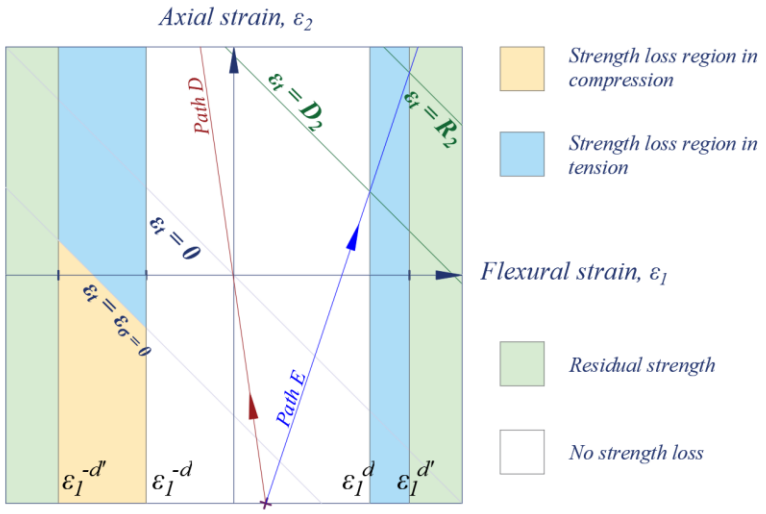

Figure 3-30 Sample load paths of steel material on e_1 - e_2 plane

Note that on *Path D*, the difference in material stress, $d\sigma$, at ε_{r1} is due to the isotropic hardening of the material in tension and compression. If the material is loaded on *Path E*, the plastic hinge rotation exceeds d, and the material degrades its strength again. Note that the total strains of the material corresponding to strength degradation of the element, (*D* and *R*) might be different than those of the previous cycle (*D* and *R*). The material flows on the residual strength region at the end of this load path.

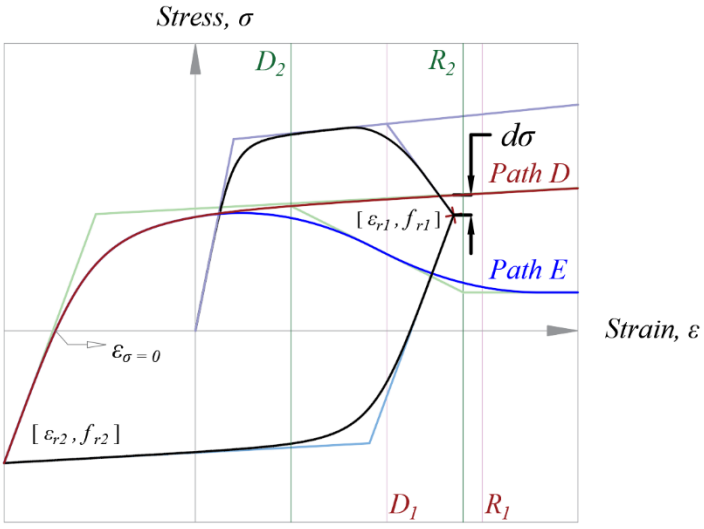

Figure 3-31 Strain - stress curve of steel material with stress degradation in tension

3.10 Cyclic Strength and stiffness degradation of the steel material in compression

Same rules that were used for modeling the strength loss in tension, are applied to model the strength loss in compression. As stated before, the strength loss in compression is associated with buckling of bars. In OpenSees implementation of this project, the steel material object has been designed so that the user can specify whether the steel bars lose strength following buckling or not. If the steel bars strength degrades post buckling, the material follows load *Path A* of Figure 3-32 and the yield strength is updated to $F_{y,T}^{1}$. The same formulation for updating the yield strength of a bar after rupture is used here. The Post Buckling unloading stiffness, E_S^{PB}, is also updated accordingly, per Eq. 3-28.

$$\frac{F_{y,T}^{PB} = F_{y,T}^{1}}{F_{y,T}} = \frac{E_S^{PB}}{E_S} \qquad \text{Eq. 3-28}$$

If the steel bars yield strength does not degrade post buckling, the material follows load *Path B* of Figure 3-32, and the unloading stiffness remains unchanged.

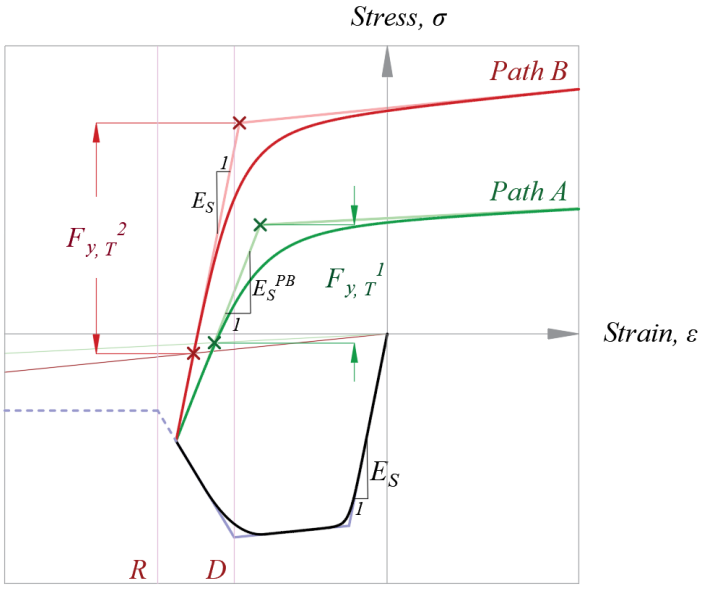

Figure 3-32 Strain - stress curve of steel material with stress degradation in compression

3.11 Cyclic Strength and stiffness degradation of the concrete material in compression

Let us assume that a concrete material starts being loaded from zero strain and stress ($[\varepsilon,\ \sigma] = [0, 0]$), and goes through the strength degradation region in compression, shown in Figure 3-33.

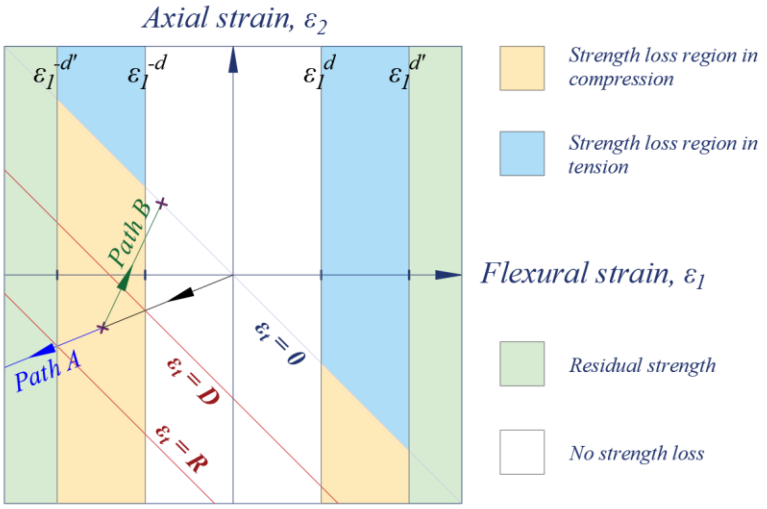

Figure 3-33 Sample load paths of concrete material on e_1 - e_2 plane

The total strains of the material, corresponding to plastic hinge rotation of d, and d' are D and R, respectively. Once the plastic hinge rotation exceeds d on load *Path A* shown in Figure 3-33, the element goes through the descending branch of the backbone curve, and the material's total strain, ε_t, exceeds D. If loading continues in the same direction, the material follows *Path B* of Figure 3-33. The plastic hinge rotation exceeds d', and material's total strain exceeds R, and flows over the residual stress region. The plot of total strain versus stress is shown in Figure 3-34. If the material is unloaded midway toward zero strain, the strain stress curve follows *Path C*. Upon a trial deformation that shows unloading of the material, strain ε_{end} is calculated according to Eq. 3-32.

$$\varepsilon_{end} = \frac{\varepsilon_0}{2}\left(\frac{\varepsilon_{min}}{\varepsilon_0}\right)^2 \qquad 0 \le \frac{0.254}{0.71} < \frac{\varepsilon_{min}}{\varepsilon_0}$$

$$\varepsilon_{end} = \varepsilon_0\left(0.145\left(\frac{\varepsilon_{min}}{\varepsilon_0}\right)^2 + 0.127\left(\frac{\varepsilon_{min}}{\varepsilon_0}\right)\right) \qquad \frac{0.254}{0.71} \le \frac{\varepsilon_{min}}{\varepsilon_0} < 2 \qquad \text{Eq. 3-29}$$

$$\varepsilon_{end} = \varepsilon_0\left(0.707\left(\frac{\varepsilon_{min}}{\varepsilon_0} - 2\right) + 0.834\right) \qquad 2 \le \frac{\varepsilon_{min}}{\varepsilon_0}$$

Once ε_{end} is computed, unloading stiffness, E_{unl}, is determined knowing stress at load reversal.

$$E_{unl} = \frac{\varepsilon_{end} - \varepsilon_r}{0 - f_r} \qquad \text{Eq. 3-30}$$

The approach implemented here for calculation of the material's unloading properties is used in OpenSees material "*Concrete01*".

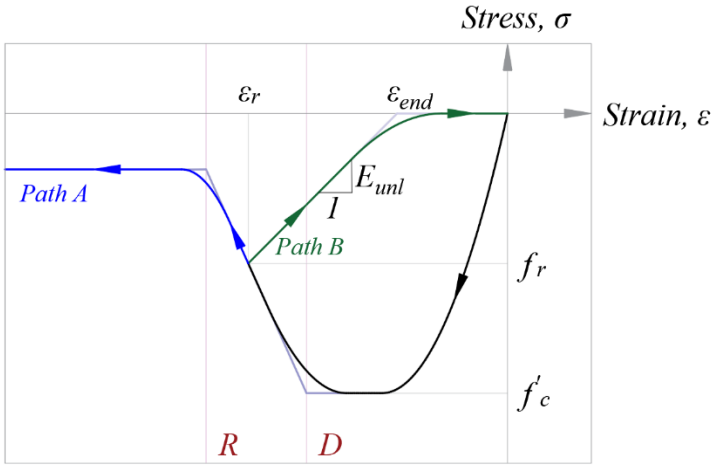

Figure 3-34 Strain - stress curve of steel material with strength degradation

Assume there is another load reversal at zero strain and the material is compressively loaded again. If the element is loaded without exceeding the rotation capacity, the strain stress curve follows *Path A* of Figure 3-35, and there is no stress degradation.

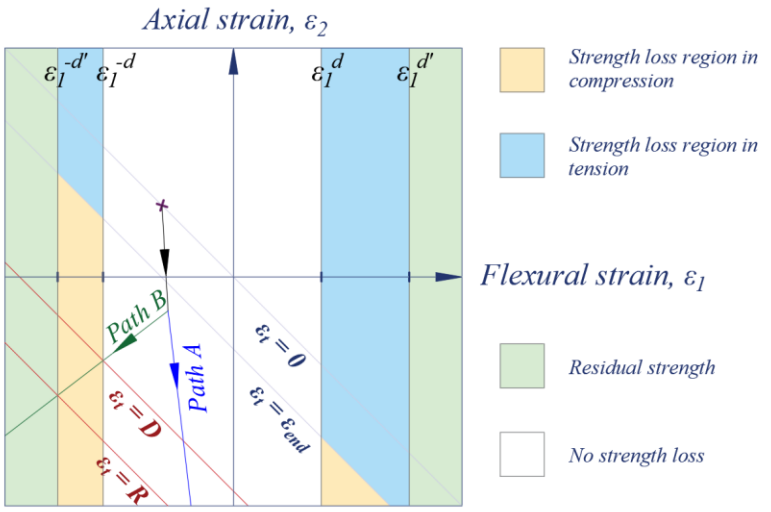

Figure 3-35 A sample load paths of concrete material on e_1 - e_2 plane

If the rotation capacity of the element is exceeded, as is the case for load *Path B* of Figure 3-35, the material loses strength as can be seen in Figure 3-36.

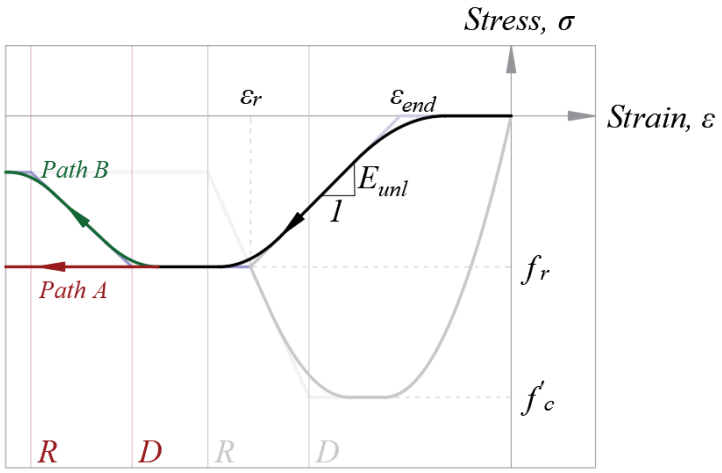

Figure 3-36 Strain - stress curve of steel material with strength degradation

3.12 Element stiffness matrix

The components of the stiffness matrix of the element used in this study are calculated by computing the derivatives of Eq. 3-31.

$$K_{ij} = \frac{\partial F_i}{\partial u_j} \qquad \text{Eq. 3-31}$$

Most of the stiffness matrix components are the same as those of the MVL variant adopted by Fischinger et al. The horizontal force at the top and bottom nodes, F_1 and F_4 are equal to the constant shear force across the element. With the shear spring of the element being elastic linear, Eq. 3-32 turns the internal shear force in terms of the top and bottom nodal displacements. K_h is the stiffness of the elastic linear spring that captures element's shear response.

$$F_1 = -F_4 = V = K_h d_{SS} = K_h[u_B - cH_e\theta_B - (1-c)H_e\theta_T - u_T] \qquad \text{Eq. 3-32}$$

The first column of the stiffness matrix is calculated in Eq. 3-33.

$$\begin{aligned}
K_{11} &= \frac{\partial F_1}{\partial u_1} = \frac{\partial F_1}{\partial u_B} = K_h \\
K_{21} &= \frac{\partial F_1}{\partial u_2} = \frac{\partial F_1}{\partial v_B} = 0 \\
K_{31} &= \frac{\partial F_1}{\partial u_3} = \frac{\partial F_1}{\partial \theta_B} = -K_h c H_e \\
K_{41} &= \frac{\partial F_1}{\partial u_4} = \frac{\partial F_1}{\partial u_T} = -K_h \\
K_{51} &= \frac{\partial F_1}{\partial u_5} = \frac{\partial F_1}{\partial v_T} = 0 \\
K_{61} &= \frac{\partial F_1}{\partial u_6} = \frac{\partial F_1}{\partial \theta_T} = -K_h(1-c)H_e
\end{aligned} \qquad \text{Eq. 3-33}$$

The internal axial load is the sum of fibers' uniaxial load. Eq. 3-34 turns this axial load in terms of the top and bottom nodal displacements.

$$F_2 = -F_5 = \sum_{f=1}^{N_F} A_C^f \, \sigma_C^f(\varepsilon) + \sum_{f=1}^{N_F} A_S^f \, \sigma_S^f(\varepsilon)$$

$$F_2 = -F_5 = \sum_{f=1}^{N_F} A_C^f \, \sigma_C^f\left(\frac{v_T - v_B}{H_e}, \quad \frac{\theta_T - \theta_B}{H_e} x^f\right) + \sum_{f=1}^{N_F} A_S^f \, \sigma_S^f\left(\frac{v_T - v_B}{H_e}, \quad \frac{\theta_T - \theta_B}{H_e} x^f\right) \qquad \text{Eq. 3-34}$$

x^f is the local coordinate of the fiber. Note that a material with strain-strain-stress response of Figure 3-22 and Figure 3-23, in general, has two tangents with respect to the flexural strain and the axial strain. This is in Eq. 3-35.

$$E_1 = \frac{\partial \sigma}{\partial \varepsilon_1}, \quad E_2 = \frac{\partial \sigma}{\partial \varepsilon_2}, \quad \varepsilon_1 = \frac{\theta_T - \theta_B}{H_e} x^f, \quad \varepsilon_2 = \frac{v_T - v_B}{H_e} \qquad \text{Eq. 3-35}$$

If the material is not in the stress degradation region of Figure 3-21, the two tangents are essentially equal, $E_1 = E_2$. Using the chain rule of differentiation, Eq. 3-36 turns the differentiation of the material's stress with respect to the nodal displacements.

$$\frac{\partial \sigma}{\partial v_B} = -\frac{E_2}{H_e}, \quad \frac{\partial \sigma}{\partial v_T} = \frac{E_2}{H_e}, \quad \frac{\partial \sigma}{\partial \theta_B} = -\frac{E_2 x^f}{H_e}, \quad \frac{\partial \sigma}{\partial \theta_T} = -\frac{E_2 x^f}{H_e} \qquad \text{Eq. 3-36}$$

The terms calculated in Eq. 3-36 are used to obtain the second column of the stiffness matrix in Eq. 3-37.

$$K_{12} = \frac{\partial F_2}{\partial u_1} = \frac{\partial F_2}{\partial u_B} = 0$$

$$K_{22} = \frac{\partial F_2}{\partial u_2} = \frac{\partial F_2}{\partial v_B} = \sum_{f=1}^{N_F} \frac{A_C^f}{H_e} E_2^C + \sum_{f=1}^{N_F} \frac{A_S^f}{H_e} E_2^S$$

$$K_{32} = \frac{\partial F_2}{\partial u_3} = \frac{\partial F_2}{\partial \theta_B} = \sum_{f=1}^{N_F} \frac{A_C^f}{H_e} E_1^C x^f + \sum_{f=1}^{N_F} \frac{A_S^f}{H_e} E_1^S x^f$$

$$K_{42} = \frac{\partial F_2}{\partial u_4} = \frac{\partial F_2}{\partial u_T} = 0$$

$$K_{52} = \frac{\partial F_2}{\partial u_5} = \frac{\partial F_2}{\partial v_T} = -\sum_{f=1}^{N_F} \frac{A_C^f}{H_e} E_2^C - \sum_{f=1}^{N_F} \frac{A_S^f}{H_e} E_2^S$$

$$K_{62} = \frac{\partial F_2}{\partial u_6} = \frac{\partial F_2}{\partial \theta_T} = -\sum_{f=1}^{N_F} \frac{A_C^f}{H_e} E_1^C x^f - \sum_{f=1}^{N_F} \frac{A_S^f}{H_e} E_2^S x^f$$

Eq. 3-37

The third component of the internal force vector is the moment at the bottom node, calculated in Eq. 3-38 in terms of the element's displacement components.

$$F_3 = M_B = \sum_{f=1}^{N_F} A_C^f \sigma_C^f(\varepsilon) x^f + \sum_{f=1}^{N_F} A_S^f \sigma_S^f(\varepsilon) x^f + VcH_e = \sum_{f=1}^{N_F} A_C^f \sigma_C^f \left(\frac{v_T - v_B}{H_e}, \quad \frac{\theta_T - \theta_B}{H_e} x^f \right)$$

$$+ \sum_{f=1}^{N_F} A_S^f \sigma_S^f \left(\frac{v_T - v_B}{H_e}, \quad \frac{\theta_T - \theta_B}{H_e} x^f \right) + K_h [u_B - cH_e\theta_B - (1-c)H_e\theta_T - u_T] cH_e$$

Eq. 3-38

Taking the derivative of Eq. 3-38 with respect to the nodal displacements, the third column of the stiffness matrix is shown in Eq. 3-39.

$$K_{13} = \frac{\partial F_3}{\partial u_1} = \frac{\partial F_3}{\partial u_B} = -K_h c H_e$$

$$K_{23} = \frac{\partial F_3}{\partial u_2} = \frac{\partial F_3}{\partial v_B} = \sum_{f=1}^{N_F} \frac{A_C^f}{H_e} E_1^C x^f + \sum_{f=1}^{N_F} \frac{A_S^f}{H_e} E_2^S x^f$$

$$K_{33} = \frac{\partial F_3}{\partial u_3} = \frac{\partial F_3}{\partial \theta_B} = K_h c^2 {H_e}^2 + \sum_{f=1}^{N_F} \frac{A_C^f}{H_e} E_1^C {x^f}^2 + \sum_{f=1}^{N_F} \frac{A_S^f}{H_e} E_2^S {x^f}^2$$

Eq. 3-39

$$K_{43} = \frac{\partial F_3}{\partial u_4} = \frac{\partial F_3}{\partial u_T} = c H_e K_h$$

$$K_{53} = \frac{\partial F_3}{\partial u_5} = \frac{\partial F_3}{\partial v_T} = -\sum_{f=1}^{N_F} \frac{A_C^f}{H_e} E_1^C x^f - \sum_{f=1}^{N_F} \frac{A_S^f}{H_e} E_2^S x^f$$

$$K_{63} = \frac{\partial F_3}{\partial u_6} = \frac{\partial F_3}{\partial \theta_T} = K_h (1-c) c {H_e}^2 - \sum_{f=1}^{N_F} \frac{A_C^f}{H_e} E_1^C {x^f}^2 - \sum_{f=1}^{N_F} \frac{A_S^f}{H_e} E_2^S {x^f}^2$$

Other components of the stiffness matrix can be obtained in the same way.

3.13 Case study 1: Static push-over analysis of a cantilever structural wall

A ten-story building, with the floor plan shown in Figure 3-37 is analyzed and designed according to California Building Code (2019) [23]. The details of analysis and design are presented in 7.3.

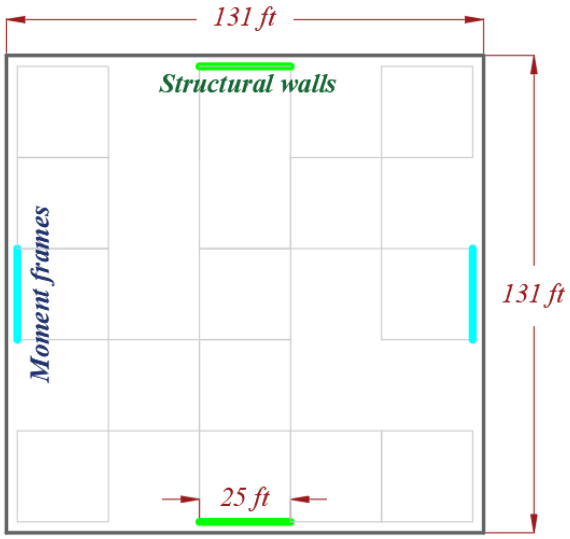

Figure 3-37 Floor plan of the building

The slabs are 10 in. thick, and the superimposed dead load of 25 psf is assumed on the floors. The live load is 40 psf. The lateral force resisting system is comprised of RC structural walls in the EW direction and RC moment frames in the NS direction. ASCE 7's Equivalent Lateral Force Procedure is used to estimate the lateral seismic loads. After some trial and error, the length of the wall is designed to be 324 in. and the thickness is 26 in. The layout of the symmetric cross section of the designed wall is shown in Figure 3-38.

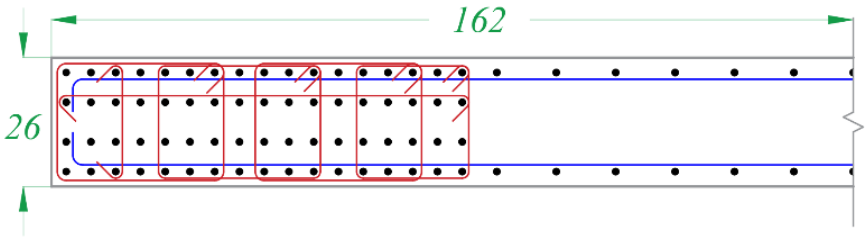

Figure 3-38 Cross section of the designed wall

Detailed analysis and design of the walls is shown in 7.3. The boundary element has 17 layers of No.10 longitudinal bars, spaced at 5 in. This results in a reinforcement ratio of 0.0386 inside the boundary element. The longitudinal reinforcement, outside the boundary element, consists of two curtains of No.10 bars spaced at 10 in., which is equivalent to a reinforcement ratio of 0.008141. The cross section of the walls is discretized into fibers, with properties in Table 3-1, to make a nonlinear model of structural walls.

Table 3-1 Properties of the cross-section fibers used in nonlinear modeling of the structural walls of case study 1

Fibers	t_F	w_F	ρ_F	A_S	A_t
	in	*in*		in^2	in^2
1	*26*	*21.5*	*0.0386*	*21.59*	*537.4*
2	*26*	*21.5*	*0.0386*	*21.59*	*537.4*
3	*26*	*21.5*	*0.0386*	*21.59*	*537.4*
4	*26*	*21.5*	*0.0386*	*21.59*	*537.4*
5	*26*	*38*	*0.00814*	*8.043*	*980.0*
6	*26*	*38*	*0.00814*	*8.043*	*980.0*
7	*26*	*38*	*0.00814*	*8.043*	*980.0*
8	*26*	*38*	*0.00814*	*8.043*	*980.0*
9	*26*	*21.5*	*0.0386*	*21.59*	*537.4*
10	*26*	*21.5*	*0.0386*	*21.59*	*537.4*
11	*26*	*21.5*	*0.0386*	*21.59*	*537.4*
12	*26*	*21.5*	*0.0386*	*21.59*	*537.4*

In Table 3-1, ρ_F is the reinforcement ratio of each fiber, A_s is the area of steel in each fiber, and A_t is the total area of each fiber. To conduct a pushover analysis of the wall, a nonlinear model of the system is created for analysis in OpenSees, an open-source software for earthquake engineering. The wall system is loaded with a triangular distribution of lateral loads that simulate seismic excitation. One element is used over each story, including the bottom story where the concentration

of demands is higher and damage accumulate. Wallace and Moehle (1992) [51] recommend Eq. 3-40 for the size of the plastic hinge (the most bottom element).

$$L_p = 0.5L_w = 0.5 \times 324 = 168\ in. \qquad \text{Eq. 3-40}$$

The deformation parameters of the backbone curve developed by Abdullah and Wallace are also obtained assuming expression of Eq. 3-40 for the plastic hinge. In 7.3, these parameters are adjusted to be used for the backbone curve of the element used in this study.

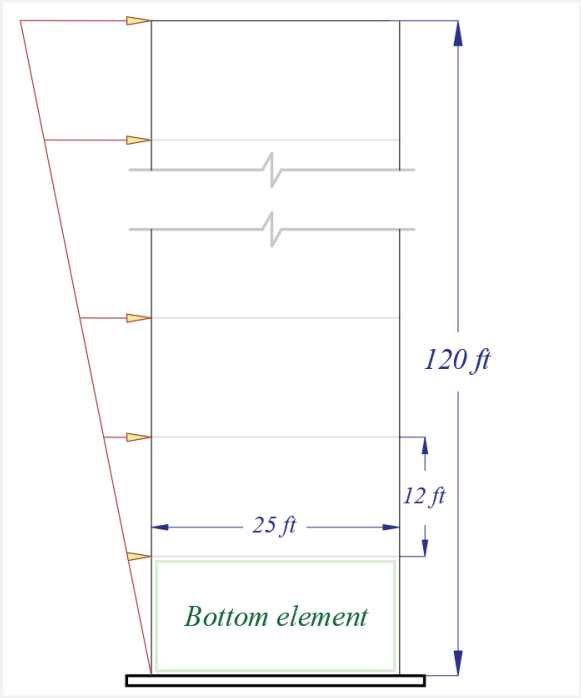

Figure 3-39 Elevation view of the wall and the distribution of lateral loads

For the static pushover analysis, the lateral displacement at the roof is the controlled degree of freedom. The loading protocol of Figure 3-40 is applied for the analysis. Amplitude of cycles is arbitrarily selected so that strength deterioration is observed at the end of analysis.

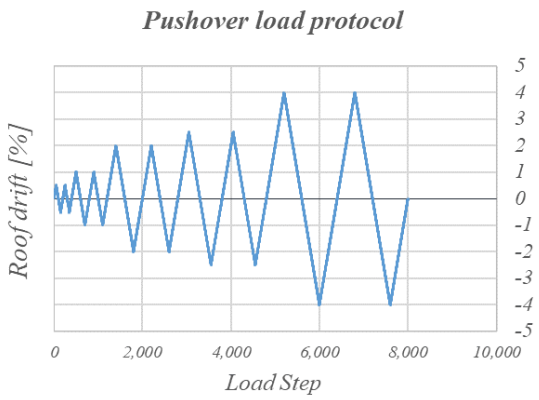

Figure 3-40 Loading protocol in study case 1, with the control deformation being the roof drift

The magnitude and the number of the cycles is shown in Table 3-2.

Table 3-2 Pushover loading cycles

Amplitude [in]	*Number of Cycles*	*Cycle type*	*Displacement increment [in]*
0.005	*2*	*Full*	*0.144*
0.01	*2*	*Full*	*0.144*
0.02	*2*	*Full*	*0.144*
0.025	*2*	*Full*	*0.144*

The residual stress of the material is set over the compressive/Tensile zone according to Eq. 3-20, and Figure 3-26. The parameters of the equation are $r_A = 0.1$, and $r_B = 0.4$, and $n = 2$. The distribution of the material residual stress is shown Figure 3-41.

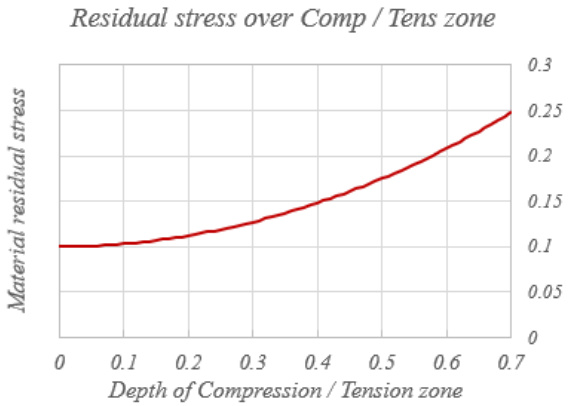

Figure 3-41 The residual stress over depth of compressive/Tensile zone

Once the analysis is complete, the element output is obtained and plotted. Figure 3-42 shows the moment rotation response of the wall plastic hinge. The deformation parameters *d* and *d'* of the backbone curve are specified with green and red lines respectively.

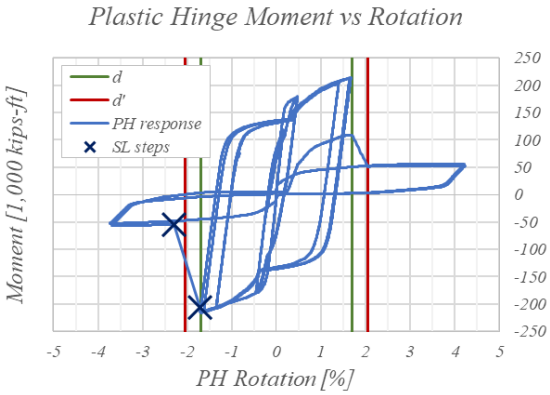

Figure 3-42 Moment curvature response of the plastic hinge to cyclic pushover loading with roof drift as the controlled degree of freedom

The strain stress response of selected steel and concrete fibers, highlighted in Figure 3-43, is presented in Figure 3-44 and Figure 3-45, respectively.

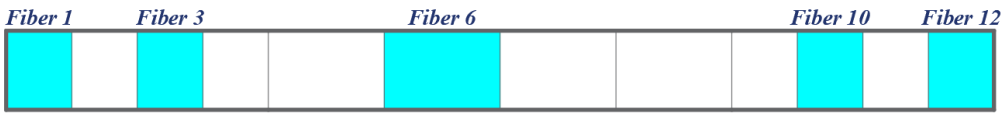

Figure 3-43 Selected fibers to plot the responses

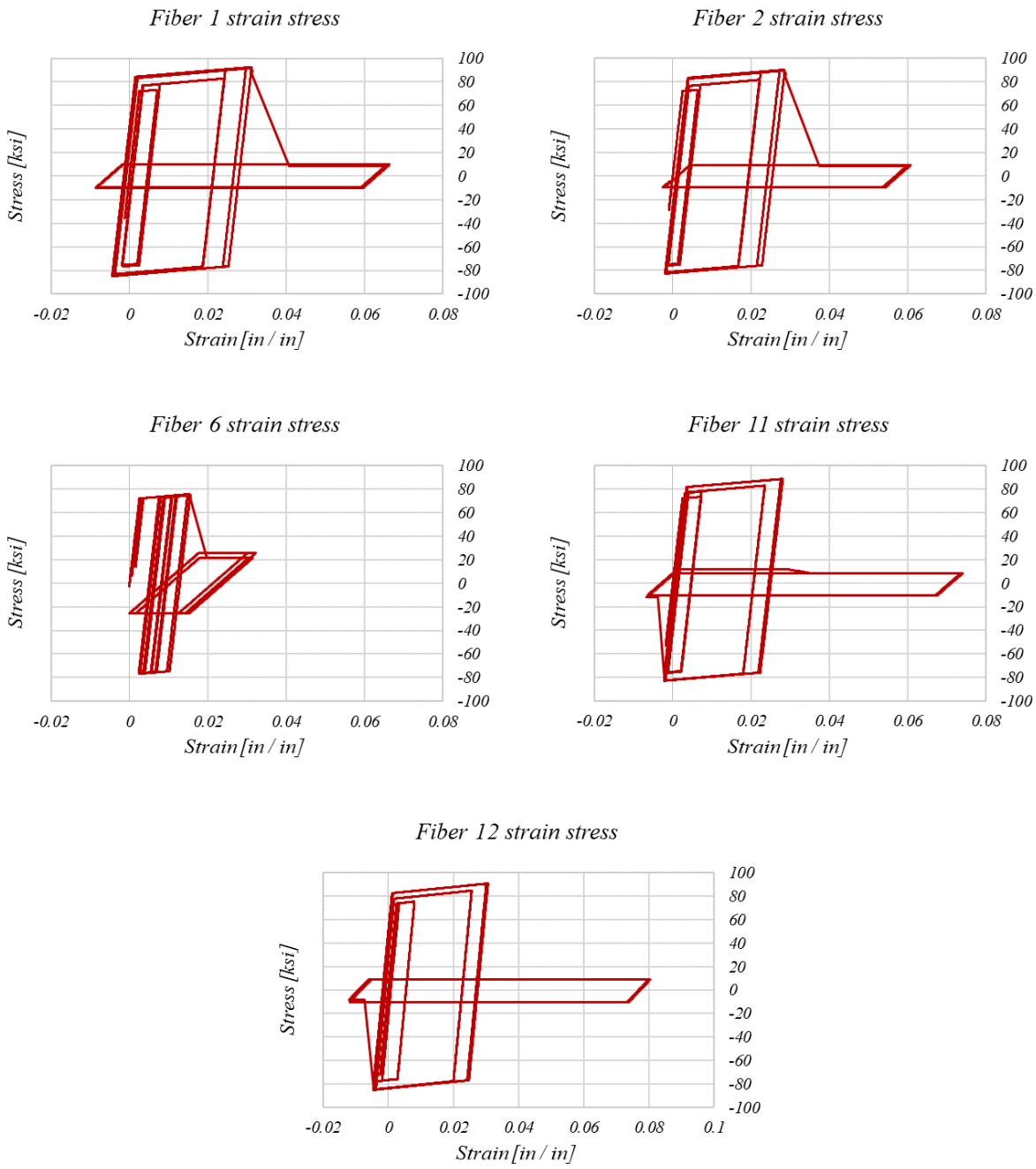

Figure 3-44 Response of selected steel fibers to static pushover loading with roof drift as the controlled degree of freedom

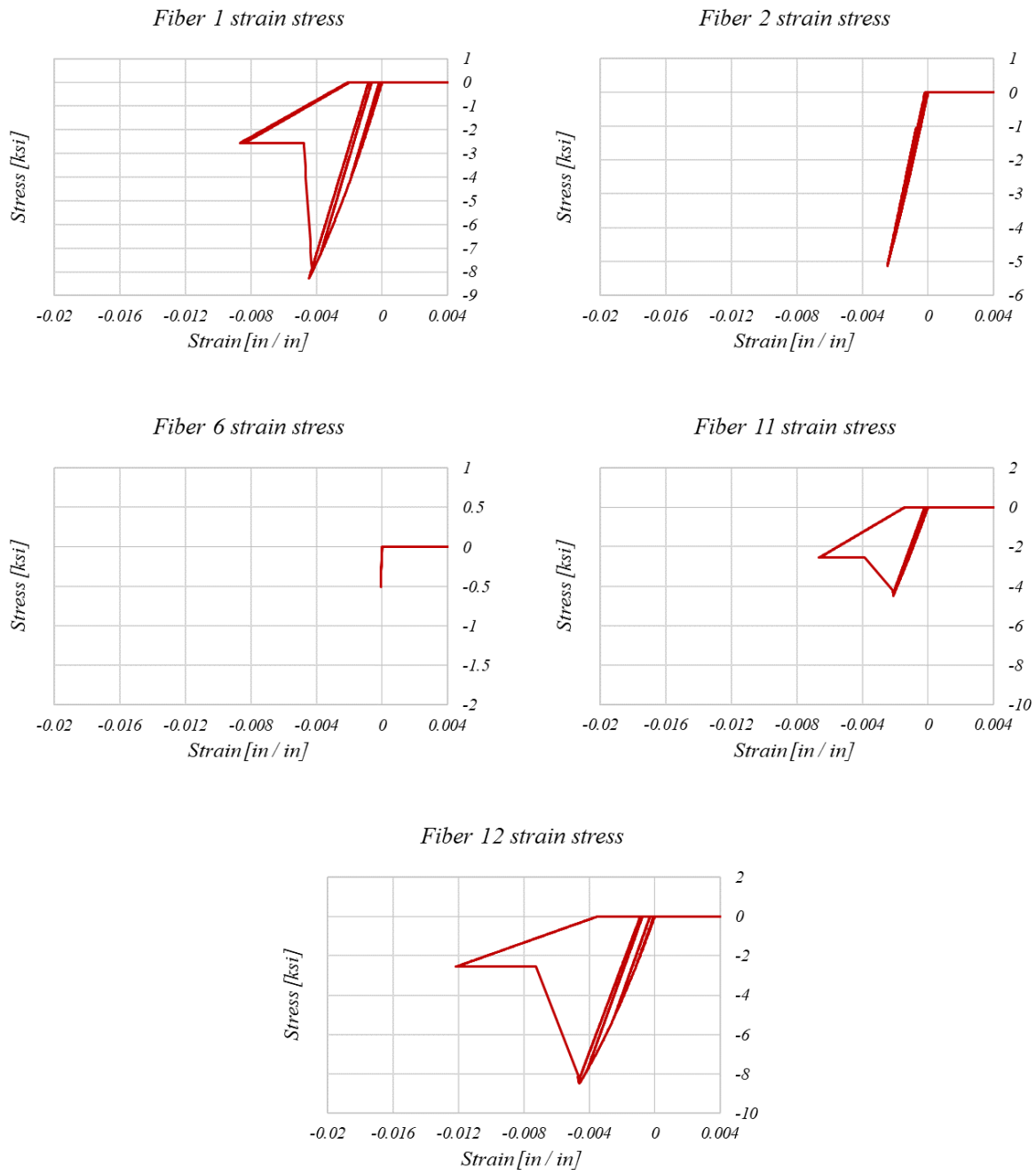

Figure 3-45 Response of selected concrete fibers to static pushover loading with roof drift as the controlled degree of freedom

The moment-rotation response of the plastic hinge in Figure 3-42 shows the entire strength-deterioration within one load step. The rotation of the plastic hinge at the end of that load step is larger than d' of Figure 3-14. This is because the control degree of freedom for the pushover

analysis is the lateral displacement at the roof. In a wall with steep strength degradation, like the designed wall in this study, a small increment in the roof displacement corresponds to a large increment of the plastic hinge rotation. To better observe the strength deterioration response of the wall element, the rotation of the plastic hinge is set as the controlled degree of freedom, and a pushover analysis is done. As a matter of experiment, the gravity axial load on the wall is also increased at each level, so that total gravity load at the base is $P_u = 25{,}000\ kips = 0.38 A_f f'_c$. The loading protocol is shown in Figure 3-46.

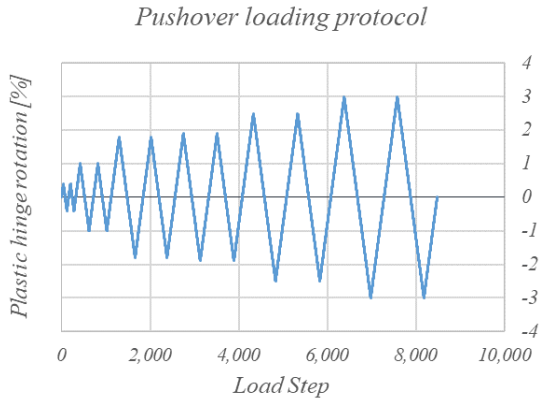

Figure 3-46 Loading protocol of wall in study case 1, the control degree of freedom is the rotation of the plastic hinge

The magnitude and the number of the cycles is shown in Table 3-3.

Table 3-3 Pushover loading cycles

Amplitude	*Number of Cycles*	*Cycle type*	*Deformation increment*
0.004	*2*	*Full*	*0.0001*
0.01	*2*	*Full*	*0.0001*
0.018	*2*	*Full*	*0.0001*
0.019	*2*	*Full*	*0.0001*
0.025	*2*	*Full*	*0.0001*
0.03	*2*	*Full*	*0.0001*

The amplitude of cycles is selected so that unloading within strength deterioration is observed in the analysis. Figure 3-47 shows the moment rotation response of the wall plastic hinge. The deformation parameters d and d' of the backbone curve are specified with green and red lines respectively.

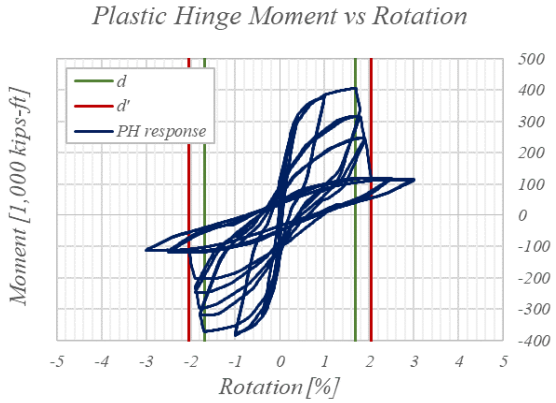

Figure 3-47 Moment curvature response of the plastic hinge to cyclic pushover loading with PH rotation as the controlled degree of freedom

The strain stress response of some selected fibers is shown in Figure 3-48.

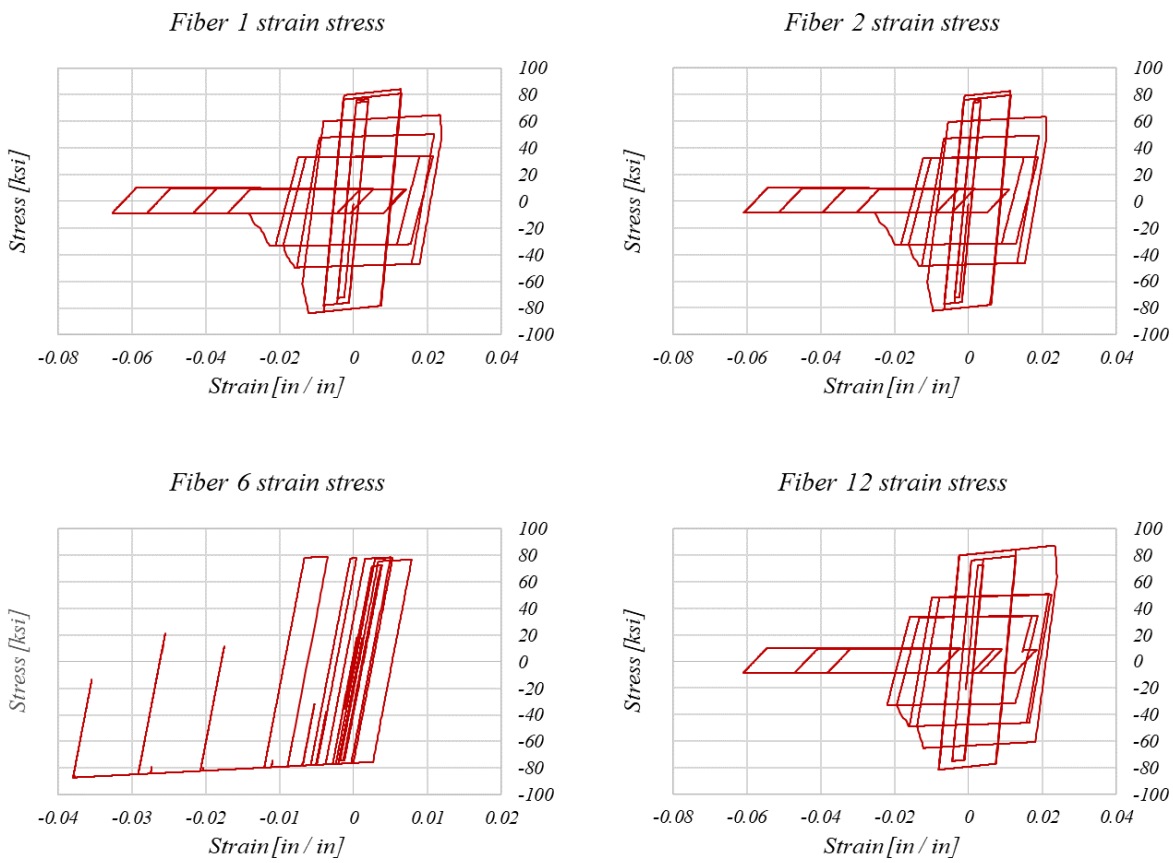

Figure 3-48 Response of selected steel fibers to static pushover loading with PH rotation as the controlled degree of freedom

The strain stress response of some selected fibers is shown in Figure 3-49.

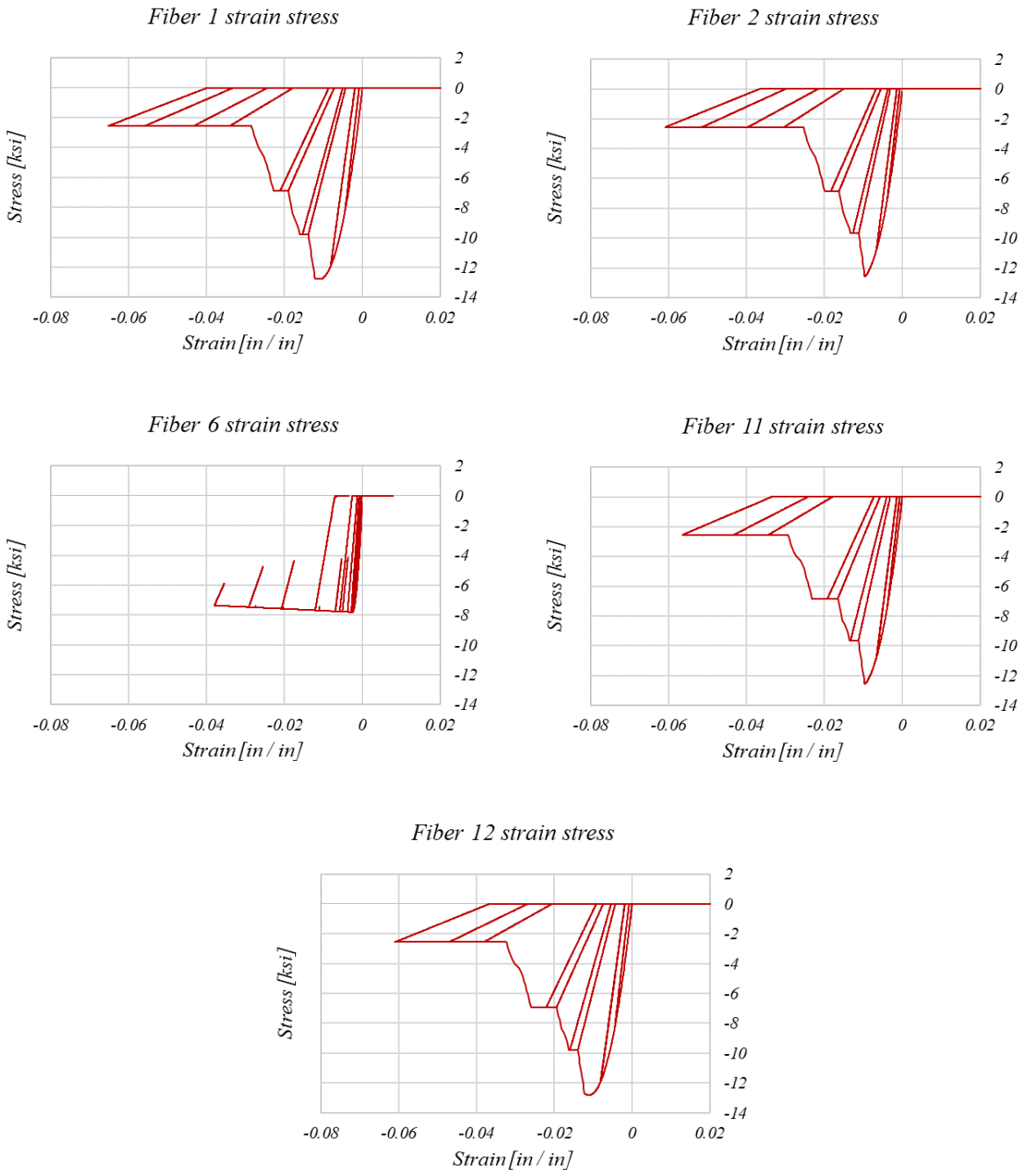

Figure 3-49 Response of selected concrete fibers to static pushover loading with PH rotation as the controlled degree of freedom

3.14 Case study 2: Nonlinear dynamic analysis of a cantilever structural wall

The response of the structural wall of 3.13 to dynamic loading is analyzed in this section. Fifteen ground motions are selected from the NGA West 2 database [44][45], and scaled to match the target MCE_R level response spectrum. Since a 2D analysis is performed, only the H_1 component of each RSN (Record Sequence Number) is scaled. Scaling is done to minimize MSE (Mean Squared Error of Record) within the period range recommended by ASCE 7 Chapter 16 ([$0.2T_1$, $2T_1$]).

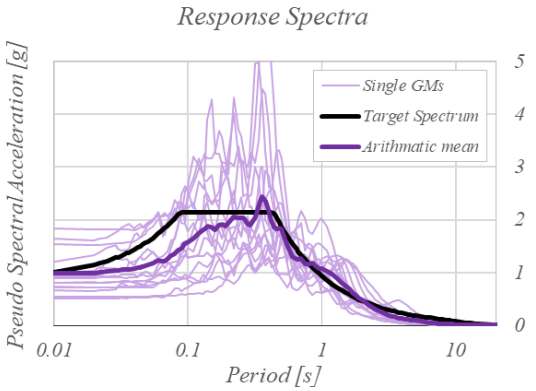

Figure 3-50 Target response spectrum and the response spectra of the selected GMs

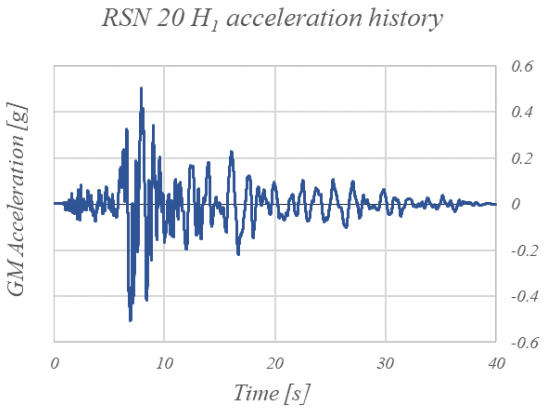

Figure 3-51 RSN 20 scaled acceleration history in H_1 direction

Figure 3-50 shows the spectra of the selected ground motions, the arithmetic mean of the spectra, and the target spectrum. Figure 3-51 shows the scaled acceleration history of ground motion RSN 20, that caused strength degradation for the wall. The moment curvature response of the wall plastic hinge is demonstrated in Figure 3-52.

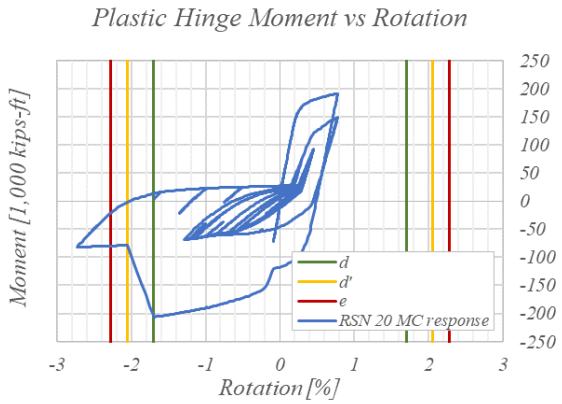

Figure 3-52 Moment curvature response of the wall plastic hinge due to dynamic loading

The response of the plastic hinge does not show any strength loss for other ground motions. This makes sense because the wall has already been designed for demands of ASCE 7 chapter 12. The plastic hinge rotation for RSN 20 exceeds the maximum capacity of the wall for bearing gravity loads (Deformation *e* of the backbone curve of Figure 4-2) and the wall collapses. In performance design of a building, consistent with TBI guidelines, this is considered an unacceptable run. In a risk category II building, one unacceptable run in a suit of 11 ground motions is permitted. But the design must be checked against amplified demands of other ground motions in the suite. One other option would be to design the wall to have more ductility capacity.

The response of selected fibers (Figure 3-43) for the RSN 20 ground motion is shown in Figure 3-53 and Figure 3-54.

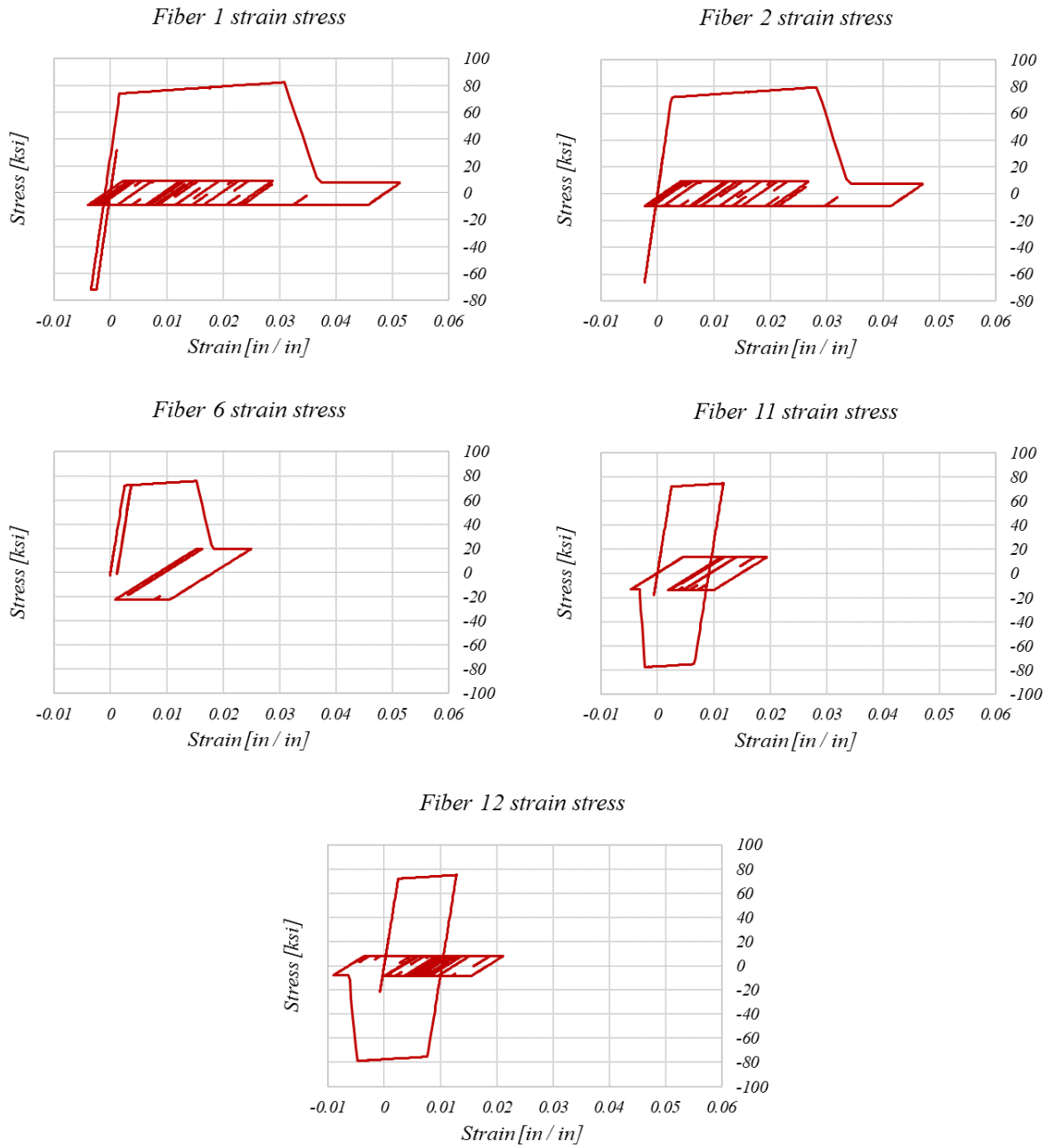

Figure 3-53 Response of selected steel fibers of wall's bottom element due to ground motion RSN 20

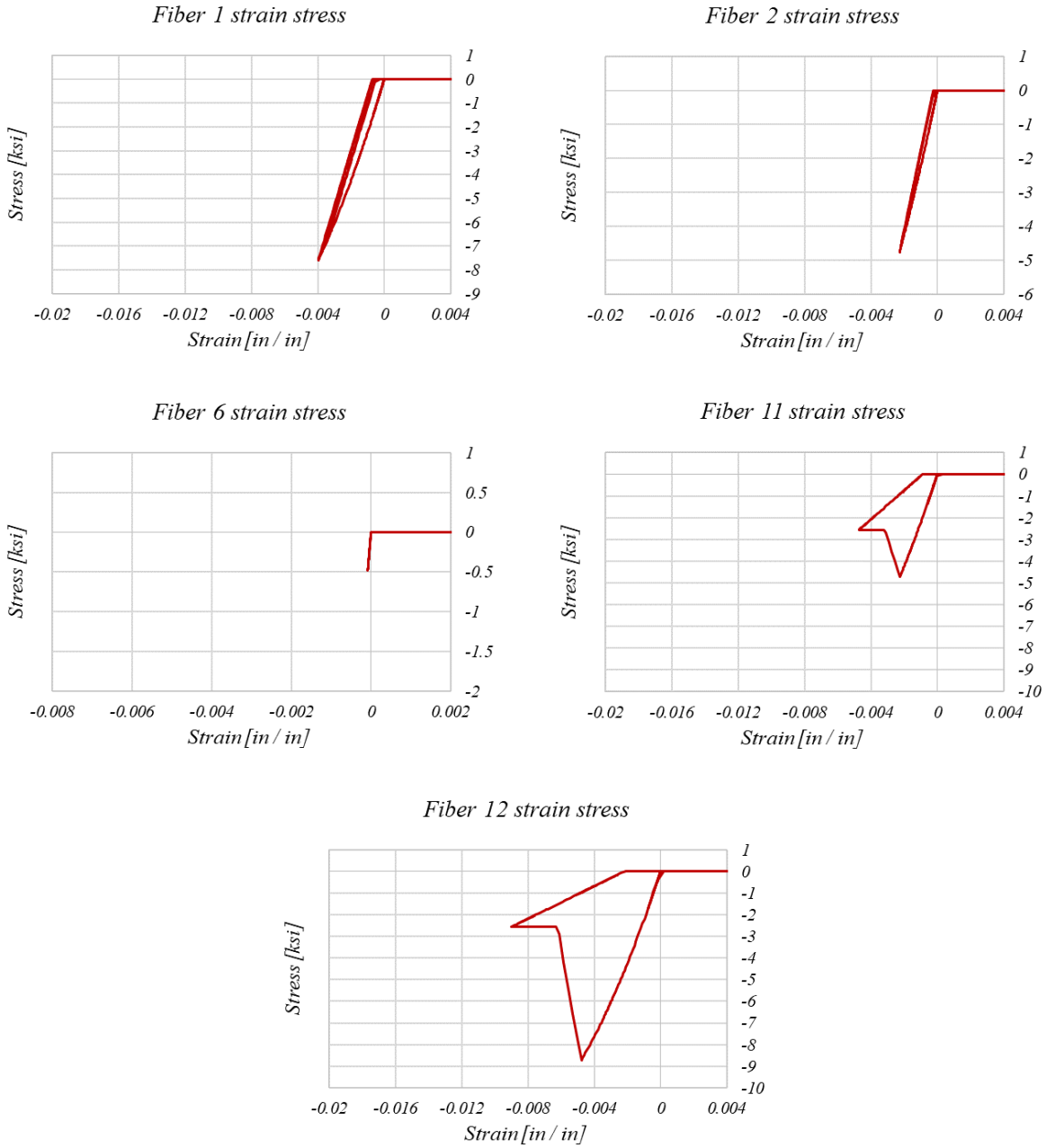

Figure 3-54 Response of selected concrete fibers of walls bottom element due to ground motion RSN 20

Chapter 4 Computing deformation parameters of the backbone curve in real time

ASCE 41-17 [2] Table 10-19, shown in Figure 4-1, specifies the deformation parameters that setup the backbone curve of flexure-controlled shear walls.

Conditions			Plastic Hinge Rotation (radians)		Residual Strength Ratio	Acceptable Plastic Hinge Rotation[a] (radians) Performance Level		
			a	*b*	*c*	IO	LS	CP
i. Structural walls and wall segments								
$\frac{(A_s - A'_s)f_{yE} + P}{t_w l_w f'_{cE}}$	$\frac{V}{t_w l_w \sqrt{f'_{cE}}}$	Confined Boundary[b]						
≤0.1	≤4	Yes	0.015	0.020	0.75	0.005	0.015	0.020
≤0.1	≥6	Yes	0.010	0.015	0.40	0.004	0.010	0.015
≥0.25	≤4	Yes	0.009	0.012	0.60	0.003	0.009	0.012
≥0.25	≥6	Yes	0.005	0.010	0.30	0.0015	0.005	0.010
≤0.1	≤4	No	0.008	0.015	0.60	0.002	0.008	0.015
≤0.1	≥6	No	0.006	0.010	0.30	0.002	0.006	0.010
≥0.25	≤4	No	0.003	0.005	0.25	0.001	0.003	0.005
≥0.25	≥6	No	0.002	0.004	0.20	0.001	0.002	0.004
ii. Structural wall coupling beams[c] Longitudinal reinforcement and transverse reinforcement[d]	$\frac{V}{t_w l_w \sqrt{f'_{cE}}}$		[d]	[e]	[c]			
Nonprestressed longitudinal reinforcement with conforming transverse reinforcement	≤3		0.025	0.050	0.75	0.010	0.025	0.050
	≥6		0.020	0.040	0.50	0.005	0.020	0.040
Nonprestressed longitudinal reinforcement with nonconforming transverse reinforcement	≤3		0.020	0.035	0.50	0.006	0.020	0.035
	≥6		0.010	0.025	0.25	0.005	0.010	0.025
Diagonal reinforcement	NA		0.030	0.050	0.80	0.006	0.030	0.050

[a] Linear interpolation between values listed in the table shall be permitted.
[b] A boundary element shall be considered confined where transverse reinforcement exceeds 75% of the requirements given in ACI 318 and spacing of transverse reinforcement does not exceed $8d_b$. It shall be permitted to take modeling parameters and acceptance criteria as 80% of confined values where boundary elements have at least 50% of the requirements given in ACI 318 and spacing of transverse reinforcement does not exceed $8d_b$. Otherwise, boundary elements shall be considered not confined.
[c] For coupling beams spanning 8 ft 0 in., with bottom reinforcement continuous into the supporting walls, acceptance criteria values shall be permitted to be doubled for LS and CP performance.
[d] Nonprestressed longitudinal reinforcement consists of top and bottom steel parallel to the longitudinal axis of the coupling beam. Conforming transverse reinforcement consists of (a) closed stirrups over the entire length of the coupling beam at a spacing ≤ *d*/3, and (b) strength of closed stirrups $V_s \geq 3/4$ of required shear strength of the coupling beam.

Figure 4-1 ASCE 41-19 Table 10-19 Modeling parameters and numerical acceptance criteria for reinforced concrete structural walls controlled by Flexure

Researchers have based this table on limited number of experiments. Therefore, the deformation parameters calculated according to the table are deemed conservative. Abdullah and Wallace (2018) [50] established a comprehensive database that consists of more than 1,000 tested RC wall specimens. Analyzing the tests' data, the authors have generated Table 4-1 and Table 4-2, and

provided a more realistic tool for assessment of shear walls. The tables determine the deformation parameters controlling the shape of a backbone curve which is slightly different that the backbone curve in ASCE 41-14, as shown in Figure 4-2.

Table 4-1 Modeling parameter d for conforming reinforced concrete structural walls controlled by flexure

$\lambda = \frac{L_w C_E}{b^2}$	$\frac{\omega_v V_{M_{ult}}}{A_{cv}\sqrt{f'_c}}$	*Use of overlapping hoops*	d
≤ 10	≤ 4	*YES*	0.032
≤ 10	≥ 6	*YES*	0.026
≥ 70	≤ 4	*YES*	0.018
≥ 70	≥ 6	*YES*	0.014
≤ 10	≤ 4	*NO*	0.032
≤ 10	≥ 6	*NO*	0.026
≥ 70	≤ 4	*NO*	0.012
≥ 70	≥ 6	*NO*	0.011

Table 4-2 Modeling parameters c, d', and e for conforming reinforced concrete structural walls controlled by flexure

$\lambda = \frac{L_w C_E}{b^2}$	$\frac{P}{A_g f'_{cE}}$	c	d'	e
≤ 10	≤ 0.1	0.5	0.036	0.040
≤ 10	≥ 0.2	0.1	0.030	0.032
≥ 70	≤ 0.1	0.0	0.018	0.020
≥ 70	≥ 0.2	0.0	0.014	0.014

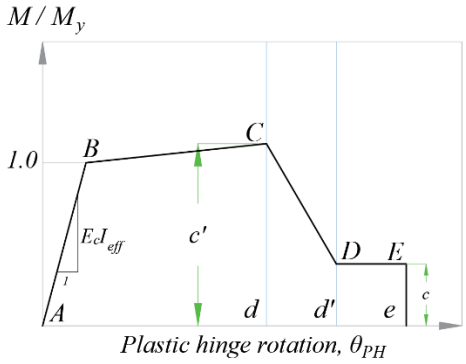

Figure 4-2 Backbone curve proposed by Abdullah and Wallace (2019)

4.1 A discussion on table parameters

The tables correlate deformation parameters of the backbone curve to the probable maximum axial load on the shear wall, P, the probable maximum shear demand, $\omega_v V_{M_{ult}}$, and the compression zone parameter, λ. An increase in any of these parameters results in a decrease in the energy absorption capacity of the element.

The axial load on the shear wall, p, is due to the gravity load, and the shear demand of connecting horizontal elements. For an isolated cantilever wall, it is acceptable to assume that the axial load is purely due to gravity load and remains constant if vertical component of ground motion is ignored. In the case of coupled walls or wall frame structures, the axial load fluctuates with lateral deformation of the building.

The second parameter, $\omega_v V_{M_{ult}}/A_{cv}\sqrt{f'_c}$, turns the maximum probable shear stress of the wall. To estimate this shear, one may use ASCE's Equivalent Lateral Force Procedure, or Linear Modal Dynamic Analysis. The shear stress calculated using either approach must be adjusted to account for design over strength, and the overstrength of the material. Furthermore, the dynamic shear amplification factor, ω_v, must be considered to account for the effect of higher modes. ACI 318-19 [9] section 18.10.3.1.3 estimates this factor based on the number of stories. Note that in a

nonlinear dynamic analysis, the element internal shear force calculated using the elements nodal displacements inherently considers the dynamic shear amplification factor and the over strength factor and no adjustment is required.

Using a database of 20 almost code compliant, flexure-controlled RC walls Segura and Wallace (2018) [35] showed that increase in depth of compression zone over the wall thickness, c/b, decreases the plastic deformation capacity of walls. Figure 4-3 shows this trend for walls with overlapping hoops and walls with hoop and cross-ties.

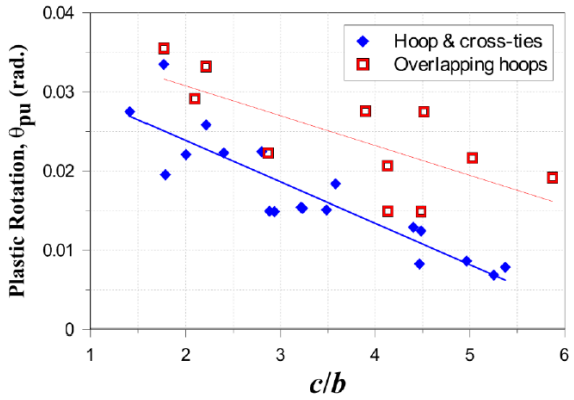

Figure 4-3 Deformation capacity of flexure-controlled walls versus c / b by Segura and Wallace (2018)

Abdullah and Wallace (2019) came up with the same conclusion by using a different approach. They used a different parameter, λ in Table 4-1, to formulate the deformation capacity. A more in-depth discussion on the compression zone depth is presented in 4.5.

In section 4.2 the solution algorithm that includes the dynamic computation of the backbone's deformation parameters is presented. A dynamic computation of deformation capacity of a wall element requires the dynamic computation of each controlling parameters in Table 4-1 and Table 4-2. Deriving each parameter in terms of curvature is explained in section 4.4, 4.5, and 4.6.

4.2 Solution procedure for a nonlinear analysis

Figure 4-4 shows the solution procedure for nonlinear force-controlled analysis of a structure. Although this algorithm is slightly different for a deformation-controlled analysis, the basics are the same. The nonlinear equation to be solved at any load step is shown in Eq. 4-1.

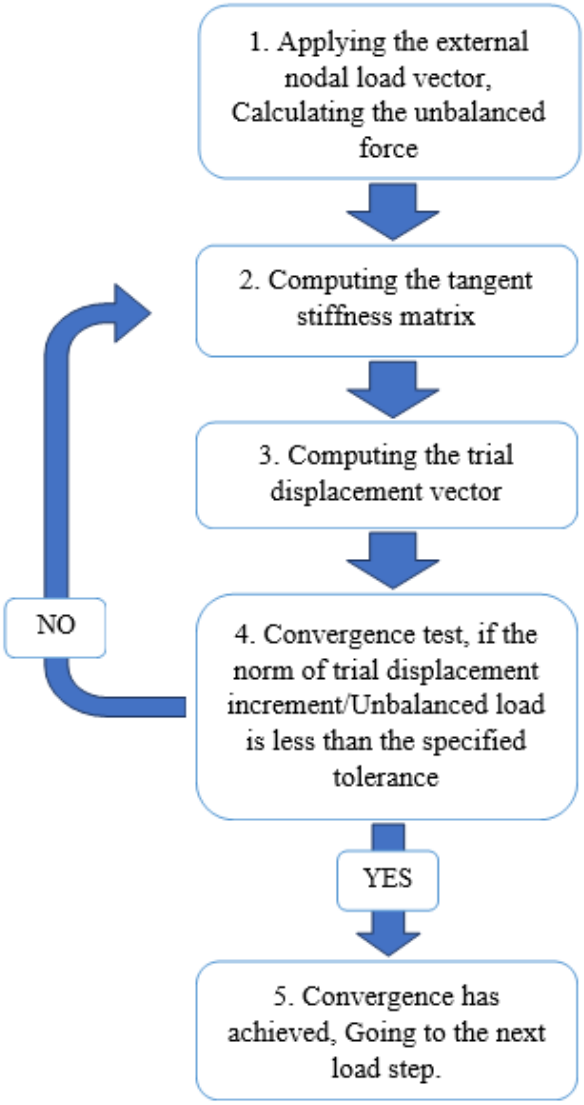

Figure 4-4 Solution algorithm for nonlinear analysis of a structure

$$U(u) = F_{ext} - F_{int}(u) = 0 \qquad \text{Eq. 4-1}$$

In Eq. 4-1, F_{ext} is the external load vector applied at nodes, and $F_{int}(u)$ is the internal load vector. $U(u)$ specifies the unbalance load at any load step. Eq. 4-2 uses Newton's algorithm to numerically solve for u.

$$u^N = u^{N-1} - \frac{U(u^{N-1})}{U'(u^{N-1})} \quad \text{Eq. 4-2}$$

In Eq. 4-2, u^N is the trial deformation at iteration N. $U'(u^{N-1})$ is the tangent stiffness of the system calculated at iteration $N-1$. In a multi degree of freedom system, $U'(u^{N-1})$ is the tangent stiffness matrix, calculated per Eq. 4-3.

$$K = \frac{\partial F_i}{\partial u_j}[e_i \otimes e_j] \quad \text{Eq. 4-3}$$

The root is found once the norm of the change in trial deformation vector $u^N - u^{N-1}$ or the norm of the unbalanced load $U(u)$ is less than a specified tolerance.

Figure 4-5 shows the deformed shape of a shear wall element in 3D space. Let the top and bottom nodes displacements be u_t, v_t, θ_t, and u_b, v_b, θ_b respectively. To ease the computations, deformation of the element is specified in a new coordinate system with axes p, q, and r defined as below.

$$p = 0.5\varphi L_w = 0.5\left[\frac{\theta_t - \theta_b}{H_e}\right]L_w \quad \text{Eq. 4-4}$$

$$q = \frac{v_e}{H_e} = \frac{v_t - v_b}{H_e} \quad \text{Eq. 4-5}$$

$$r = \frac{d_{SS}}{H_e} = \frac{u_t - u_b + \theta_b c + \theta_t[1-c]}{H_e} \quad \text{Eq. 4-6}$$

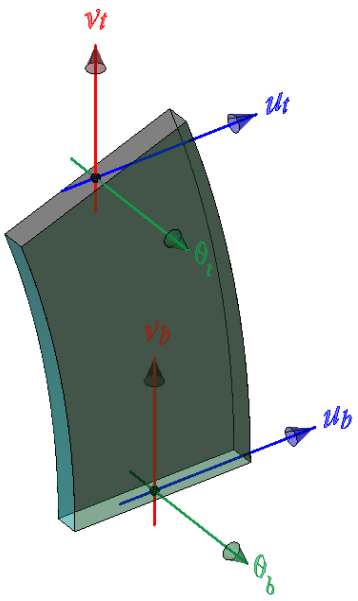

Figure 4-5 Deformed shape of the element

p is an indicator of the flexural deformation, and is equal to the maximum flexural strain over the length of the section. *q* is axial deformation of the element, and *r* is the displacement of element's shear hinge, d_{SS} divided by element height. Any trial nodal displacement calculated in step 3 of the solution flowchart specifies an arrow from the committed state of the element, *C*, to the trial state of the element, *T*, in the new deformation coordinate system, as shown in Figure 4-6. Vector $\vec{D}$ is the deformation vector in *p* – *q* – *r* coordinate system.

$\overrightarrow{D_{pq}}$ is the projection of $\vec{D}$ in the *p* – *q* plane, and $\overrightarrow{D_{pr}}$ is the projection of $\vec{D}$ in the *p* – *r* plane.

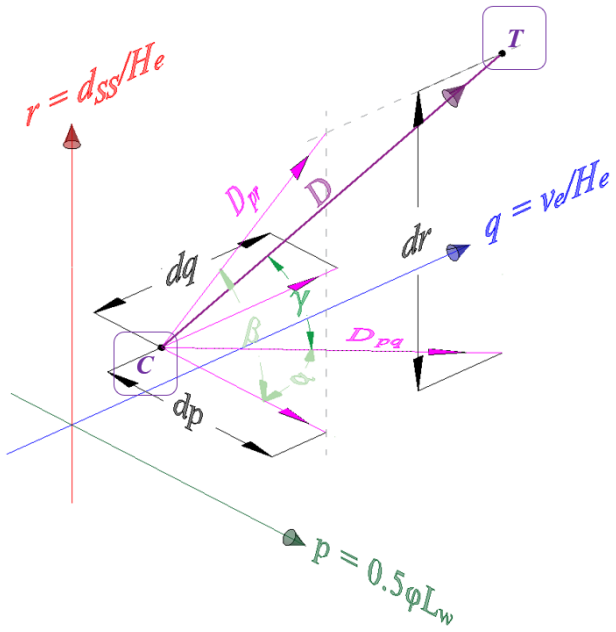

Figure 4-6 Element deformation vector

4.3 Updating the solution procedure

Figure 4-7 shows the backbone curve of a shear wall element. The horizontal axis is the element rotation, defined as element's top node rotation minus the element's bottom node rotation. The black mark shows the assumed state of the element at the end of the load step, just prior to initiation of strength loss. Given a trial change in the deformation of the element calculated in step 3 of the solution flowchart, parameter d is calculated in the direction of the deformation vector shown in Figure 4-6. Chapter 4.7 describes how to solve for d once p_u, v_u, and λ are all expressed in terms of element curvature, φ. If d is exceeded in the current iteration, $U = F_{ext} - F_{int}$ is calculated at the trial deformation, using "*Strength Loss"* equations of strain stress (Referred to as "*SL*" equation in the flowchart), and with parameter d' being calculated using table 10-19 with v_u, p_u, and λ at rotation d. If d is not exceeded, regular strain stress equations of the material (Referred to as "*NSL*" equation in the flowchart) are used.

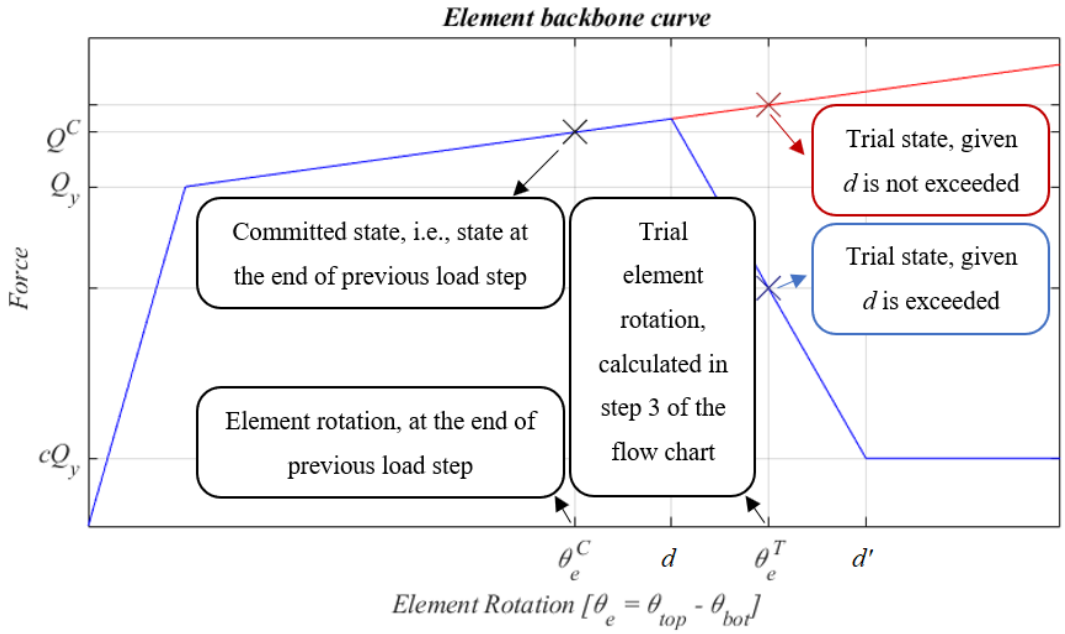

Figure 4-7 Backbone curve of a shear wall element with strength loss

Once strength loss parameters are exceeded in both directions, the procedure settles down to the flowchart of Figure 4-4.

To accommodate the dynamic computation of the strength loss parameters (i.e., d, d', and c), the solution procedure is slightly modified as shown in Figure 4-8.

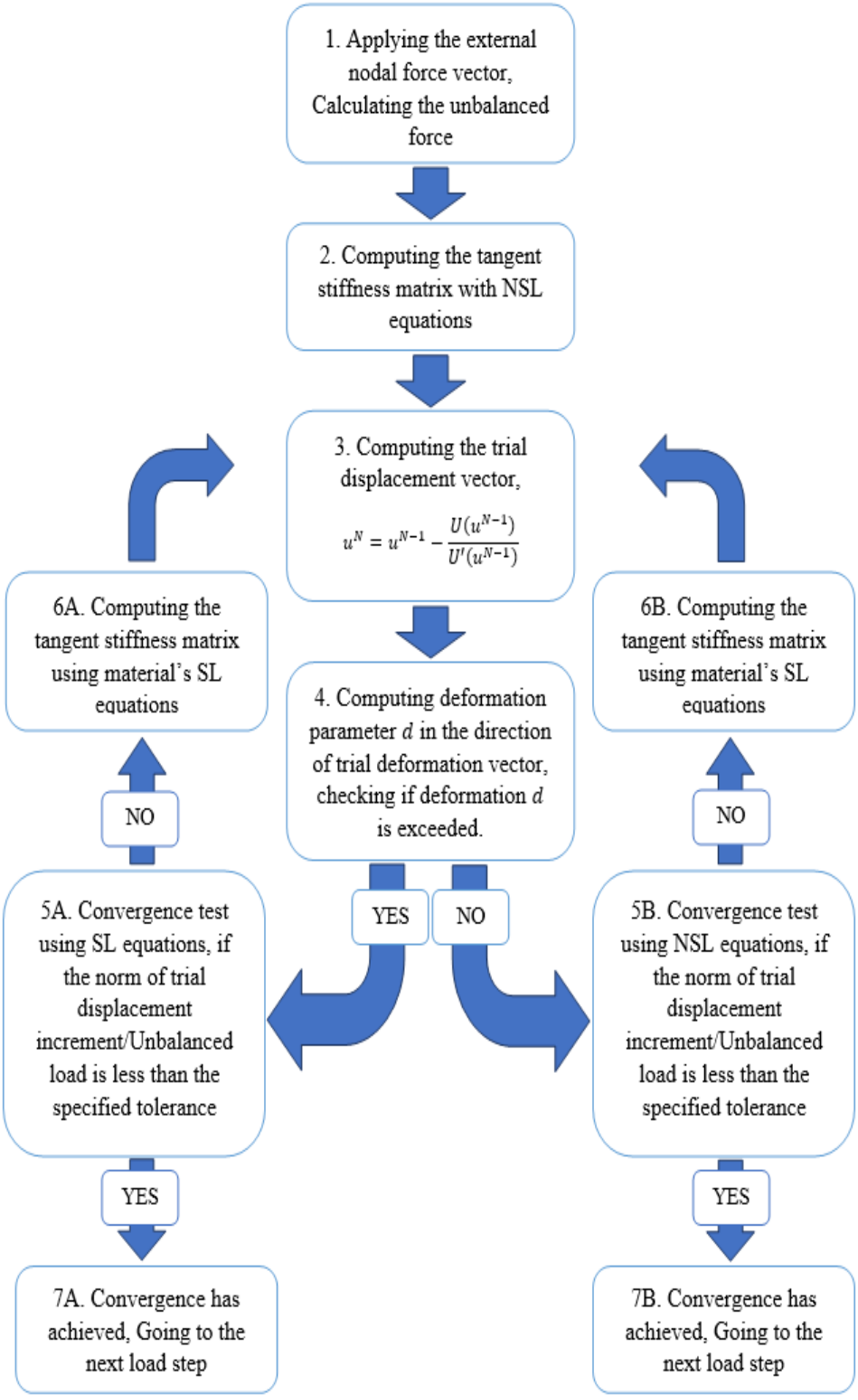

Figure 4-8 Solution algorithm for nonlinear analysis of structure with dynamic calculation of strength loss parameters

4.4 Computing the axial load

Figure 4-9 shows the fiber-discretized cross section of a deformed shear wall element.

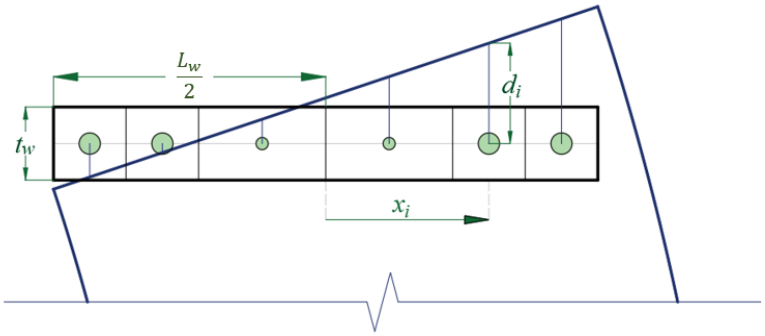

Figure 4-9 Fiber-discretized cross section of a deformed shear wall

Given the concrete area, steel area, concrete stress, and steel stress of the cross section, Eq. 4-7 turns the internal axial load.

$$P = \sum_{f=1}^{N_F} A_C^f \, \sigma_C^f + \sum_{f=1}^{N_F} A_S^f \, \sigma_S^f \qquad \text{Eq. 4-7}$$

In Eq. 4-7, area of fibers remains constant, but the stresses are functions of strains. In a computer implementation of nonlinear structural analysis, material objects turn the stress using implemented functions of strain, $\sigma = f(\varepsilon)$. To solve for backbone curve parameters, the stress-strain functions will be converted to stress-curvature functions to determine the axial load given element's curvature. Figure 4-10 shows a typical strain-stress curve for a concrete material.

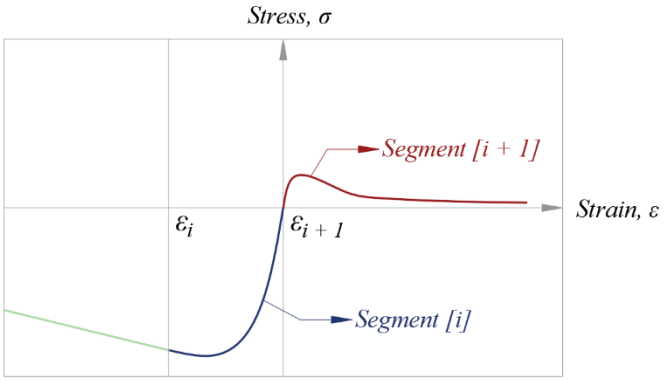

Figure 4-10 Typical strain stress relationship of a concrete material

The curve may consist of multiple segments with different function. To obtain a stress-curvature relation from a stress-strain relation, each segment of the strain stress relationship is expressed in polynomial forms as shown in Eq. 4-8.

$$\sigma_c(\varepsilon) = \begin{cases} \dots \\ \dots \\ \dots \\ \sum_{j=0}^{N} C_{[i][j]}\varepsilon^j & \varepsilon_{i-1} \le \varepsilon < \varepsilon_i \\ \sum_{j=0}^{N} C_{[i+1][j]}\varepsilon^j & \varepsilon_i \le \varepsilon < \varepsilon_{i+1} \\ \dots \\ \dots \\ \dots \end{cases} \qquad \text{Eq. 4-8}$$

Any other material used in section's fibers have stain – stress relationships defined by polynomials. By expressing the strain in terms of element curvature, the material's stress-curvature functions will be derived. To get strain-curvature relationship, consider Figure 4-11 that shows the deformation vector in p – q plane.

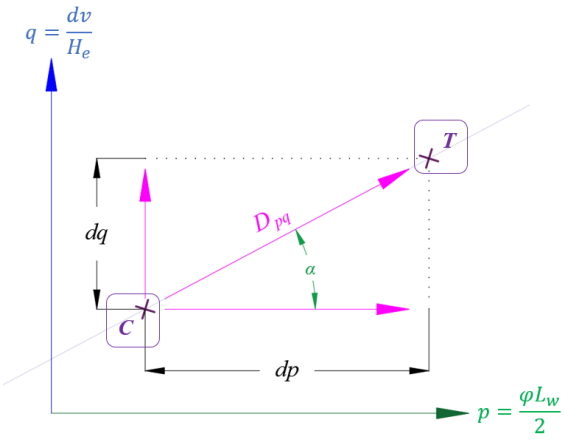

Figure 4-11 Deformation vector in p – q plane

The deformation vector $\vec{D}_{pq}$ lies on a line governed by Eq. 4-9.

$$\frac{dv}{H_e} = A\left[\varphi\frac{L_w}{2}\right] + B \qquad \text{Eq. 4-9}$$

Parameters A and B can be calculated in terms of the committed and trial state of the deformed element as shown in Eq. 4-10.

$$dp = p^C - p^T, \quad dq = q^C - q^T, \quad A = \tan\alpha = \frac{dq}{dp}, \quad B = q^C - \frac{dq}{dp}p^C \qquad \text{Eq. 4-10}$$

Knowing A and B, Eq. 4-11 determines the strain of each fiber in terms of element's curvature. All other variables are known.

$$\varepsilon^f = \varphi X^f + \frac{dv}{H_e} = \varphi\left(X^f + A\frac{L_w}{2}\right) + B = C_1\varphi + C_2, \quad C_1 = X^f + \frac{dq}{dp}\frac{L_w}{2}, \quad C_2 = q^C - \frac{dq}{dp}p^C \qquad \text{Eq. 4-11}$$

Given a certain strain for a fiber, the corresponding element curvature is calculated by Eq. 4-12. Eq. 4-12 is also used to convert the strain stress segment' start and end strain to corresponding start and end curvature.

$$\varphi_j = \frac{\varepsilon_j^f - C_2}{C_1}$$ Eq. 4-12

Knowing the stress-strain equations of the fibers' material in polynomial form of Eq. 4-8, the stress-curvature equations for fibers' material are obtained in Eq. 4-13.

$$\sigma_C(\varphi) = \begin{cases} \dots \\ \dots \\ \dots \\ \sum_{j=0}^{N} C_{[i][j]}\varphi^j & \varphi_{i-1} \le \varphi < \varphi_i \\ \sum_{j=0}^{N} C_{[i+1][j]}\varphi^j & \varphi_i \le \varphi < \varphi_{i+1} \\ \dots \\ \dots \\ \dots \end{cases}$$ Eq. 4-13

Note that for a different loading direction (i.e., for a different $\vec{D}$), the strain would be expressed by a $C_1\varphi + C_2$ function with different coefficients of C_1 and C_2.

4.5 Computing the compression zone depth

For a given state of a wall element, shown in Figure 4-12, the strain at a point x over the length of the wall section comes from Eq. 4-14.

$$\varepsilon_x = \varphi x + \varepsilon_0$$ Eq. 4-14

In this equation, φ is the curvature of the element, x is the local coordinate of point x, and ε_0 is the strain at the centroid of the section.

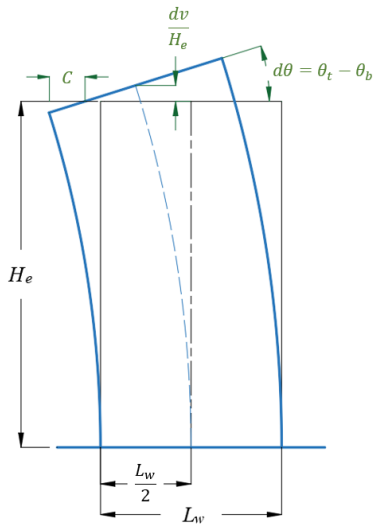

Figure 4-12 Deformed state of a shear wall element

As stated before, the curvature and the midpoint are strains are obtained from the nodal displacement using Eq. 4-15.

$$\varphi = \frac{\theta_t - \theta_b}{H_e}, \qquad \varepsilon_0 = \frac{v_t - v_b}{H_e} \tag{Eq. 4-15}$$

The deformation-wise compression zone, i.e., the depth of the section with negative strain is calculated by finding the points with zero-strain, as shown in

$$\varepsilon_x = \varphi x + \varepsilon_0 = 0, \qquad x_{\varepsilon=0} = \frac{-\varepsilon_0}{\varphi} \tag{Eq. 4-16}$$

If a wall element is in positive curvature, as shown in Figure 4-12, the depth of deformation-wise compression zone is obtained by Eq. 4-17.

$$C = x_{\varepsilon=0} - \left(\frac{-L_w}{2}\right) \tag{Eq. 4-17}$$

For negative curvature, Eq. 4-18 is used to calculated the depth of deformation-wise compression zone.

$$C = \left(\frac{L_w}{2}\right) - x_{\varepsilon=0} \qquad \text{Eq. 4-18}$$

If the coordinate of the zero-strain point, $x_{\varepsilon=0}$, is beyond the scope of the section, (i.e., $x_{\varepsilon=0} > 0.5L_w$ or $x_{\varepsilon=0} < -0.5L_w$) the entire section is in tensile or compressive strains and $C = 0$ or $C = L_w$.

The compression zone depth used in Table 4-1 and Table 4-2, to calculate the deformation parameters is the force-wise compression zone, (i.e., the depth of section with compressive stresses). In a monotonic loading of a shear wall element, the deformation-wise and force-wise compression zone are essentially equal. In the case of seismic loading, the cyclic characteristic of load may cause portions of the section to be under tensile strain while under compressive stress, or under compressive strain while under tensile stress. Figure 4-13 shows the cyclic loading of concrete material developed by Chang and Mander. The regions of "Tensile strain / Compressive stress" and "Compressive strain / Tensile stress" are indicated in the figure. Note that the compression depth calculated using concrete fibers stress is different than that using steel fibers stress. Since steel material has a larger unloading stiffness after a load reversal, the depth of steel fibers under compressive stress is always larger than the depth of concrete fibers under compressive stress. Figure 4-23 that plots the history of compression zone depth, calculated based on concrete compressive stresses and steel compressive stresses, for the right pier of the coupled-wall system in the case study of this chapter serves as an example.

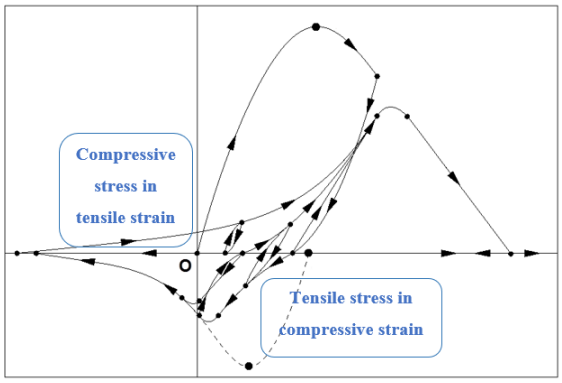

Figure 4-13 Cyclic strain stress of concrete material proposed by Chang and Mander

4.5.1 Computing the force wise compression zone

To obtain the depth of force-wise compression zone, the strain corresponding to zero stress, $\varepsilon^{\sigma=0}$, for the material (steel or concrete) at the committed state of the element (the end of the previous load step) is obtained. This is the strain at which the stress of the material would go back to zero if the material were loaded or unloaded to that strain. Figure 4-14 shows the strain stress history of the concrete material, located at local coordinate x^f of the element cross section, up until the last converged state, *C*. The zero-stress strain, $\varepsilon^{\sigma=0}$, for the concrete material at that point and at state *C* is shown in the figure.

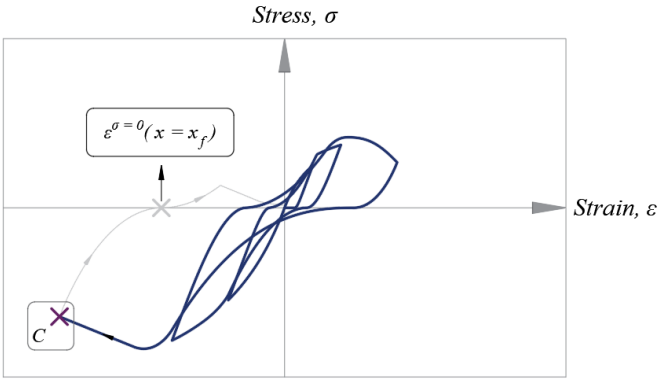

Figure 4-14 Strain stress history of concrete material at local coordinate X_F of cross section

Knowing the zero-stress strains of the material for the entire section, Figure 4-15 shows the zero-stress strain profile ($\varepsilon^{\sigma=0}$ profile) of the element. With the section discretized into fibers, the $\varepsilon^{\sigma=0}$ profile takes a piecewise form with equations shown in the figure.

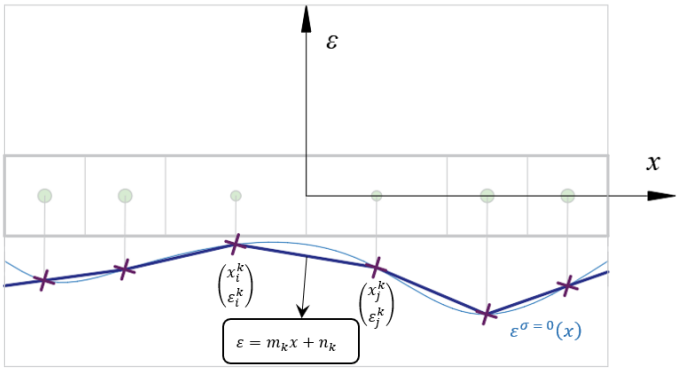

Figure 4-15 The zeros stress strain profile of the shear wall section

Given the profile shown in the figure corresponding to the converged (committed) state of the element, if the strain at any point of the section, for a trial state of the element, is below the profile at that point, the point is in compressive stress. If the trial strain is above the profile, the point is not in compressive stress (zero, or tensile stress).

4.5.2 Determining the compression zone as a function of curvature

Figure 4-16 shows the strain over the depth of the element section at the converged state ***C***, and for a trial state ***T*** of the element. The strain profiles are governed by Eq. 4-19.

$$\varepsilon^C = \varphi^C x + {\varepsilon_0}^C, \qquad \varepsilon^T = \varphi^T x + {\varepsilon_0}^T \qquad \text{Eq. 4-19}$$

By moving along the deformation vector of the element shown in Figure 4-6 and Figure 4-11, the strain profile of the section rotates about the "*Hinge Point*" shown in Figure 4-16. This point is the intersection of the trial strain profile and the strain profile of the committed state.

$$x_H = \frac{d\varepsilon_0}{d\varphi}, \qquad \varepsilon_H = \varphi^C x_H + {\varepsilon_0}^C \qquad \text{Eq. 4-20}$$

Note that for a different deformation vector of Figure 4-6, the trial strain profile, ***T***, and the location of the hinge would be different. So, the hinge must be located every time a trial deformation is computed in Step 3 of the solution algorithm.

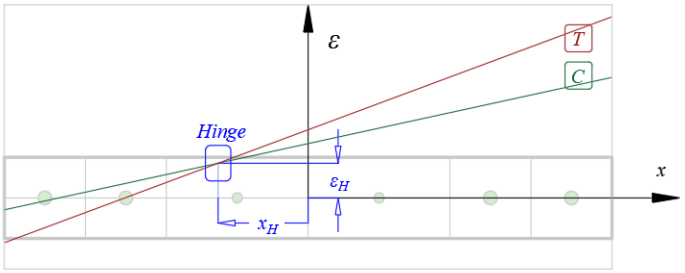

Figure 4-16 Committed and trial strain profile over element cross section

Figure 4-17 shows two trial strain profiles, ***T₁*** and ***T₂***, passing through the hinge (at a different location than that in Figure 4-16 for clarity), and the committed state of the zeros – stress strain profile. ***T₁*** crosses segment k of the committed zero – stress strain profile with start and end coordinates x_i^k and x_j^k. The local coordinate where the two profiles cross, x_{CZ}, is calculated in Eq. 4-21.

$$m_k x_{CZ}^k + n_k = \varphi(x_{CZ}^k - x_H) + \varepsilon_H, \qquad x_{CZ}^k = \frac{x_H\varphi + n_k - \varepsilon_H}{\varphi - m_k} \qquad \text{Eq. 4-21}$$

The depth of the compression zone is where the strain profile is below the zero – stress strain profile and is calculated in Eq. 4-22.

$$CZ(\varphi) = x_{CZ}^k - \left(-\frac{L_w}{2}\right) = \frac{x_H\varphi + n_k - \varepsilon_H}{\varphi - m_k} + \frac{L_w}{2} \qquad \text{Eq. 4-22}$$

Note that the strain profile may cross the zero – stress profile at multiple segments as is the case for the trial deformation T_2. The depth of the compression zone for T_2 is obtained in Eq. 4-23.

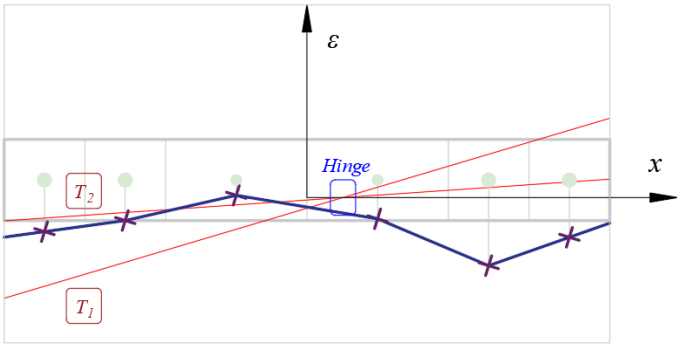

Figure 4-17 Setting compression zone as a function of curvature

$$CZ(\varphi) = x_{CZ}^{k} - x_{CZ}^{k-1} = \frac{x_H\varphi + n_k - \varepsilon_H}{\varphi - m_k} - \frac{x_H\varphi + n_{k-1} - \varepsilon_H}{\varphi - m_{k-1}} \qquad \text{Eq. 4-23}$$

In the computer implementation, a subroutine traverses all segments of the zero-stress strain profile to find the coefficients a_0, a_1, a_2, and a_3. This obtains the general form of the compression zone versus curvature relationship, shown in Eq. 4-24.

$$CZ(\varphi) = \sum_{k=1}^{NF-1} a_0^k + \frac{a_1^k\varphi + a_2^k}{\varphi + a_3^k} \qquad \text{Eq. 4-24}$$

The derivative of the compression zone with respect to curvature is in Eq. 4-25.

$$\frac{\partial CZ(\varphi)}{\partial\varphi} = \sum_{k=1}^{NF-1} \frac{a_1^k a_3^k - a_2^k}{(\varphi + a_3^k)^2} \qquad \text{Eq. 4-25}$$

4.6 Computing the shear force

Figure 4-18 shows the deformation vector in $r - p$ plane. The deformation vector $\vec{D}_{pr}$ lies on a line governed by Eq. 4-26.

$$\frac{d_{SS}}{H_e} = C\left[\varphi\frac{L_w}{2}\right] + D \qquad \text{Eq. 4-26}$$

Parameters C and D are calculated in terms of the committed and trial state of the deformed element as shown in Eq. 4-27.

$$dp = p^C - p^T, \qquad dr = r^C - r^T, \qquad C = \tan\beta = \frac{dr}{dp}, \qquad D = r^C - \frac{dr}{dp}p^C \qquad \text{Eq. 4-27}$$

Knowing C and D, the stress demand of Table 4-2 is given by Eq. 4-28.

$$v_u(\varphi) = \frac{\omega_v V_{@M_{ult}}}{A_{cv}\sqrt{f'_c}} = \frac{K_{SS}H_e\left(C\left[\varphi\frac{L_w}{2}\right] + D\right)}{A_{cv}\sqrt{f'_c}} \qquad \text{Eq. 4-28}$$

The derivative of the shear stress with respect to curvature is in Eq. 4-29.

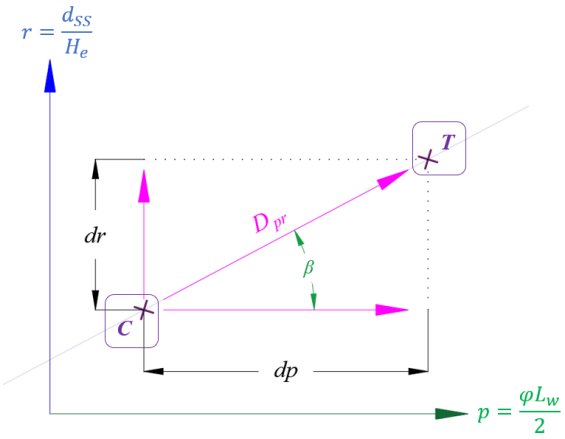

Figure 4-18 Deformation vector in r - p plane

$$\frac{\partial v_u}{\partial \varphi} = \frac{H_e C L_w}{2A_{cv}\sqrt{f'_c}} \qquad \text{Eq. 4-29}$$

This derivative is then used to solve for a $D/C = 1$ for the desired deformation parameter. This will be shown later in 4.7.

4.7 Solving for deformation parameters

The final form of the equation to solve for deformation parameter d within any load step is shown in Eq. 4-30.

$$F = \varphi - d(\varphi) = 0 \qquad \text{Eq. 4-30}$$

Newton's approach in Eq. 4-31 is used to solve for curvature at which d is exceeded.

$$\varphi_{N+1} = \varphi_N - \frac{F_N}{F'_N} \qquad \text{Eq. 4-31}$$

The sample problem in **Error! Reference source not found.** shows the procedure.

4.8 Case study: analysis of a coupled wall system

This chapter concludes with a case study to show how the element works. The 12-story coupled wall system, shown in Figure 4-19, is analyzed for dynamic analysis. The cross section of the wall piers is shown in Figure 4-20. The piers are symmetric with respect to the centroid of the coupling beams. The exterior boundary of the walls is reinforced with 27 No. 11 bars spaced at 6 in. and the interior boundary is reinforced with 15 No. 11 bars, spaced at 6 in. This results in a reinforcement ratio of 4.875 %.

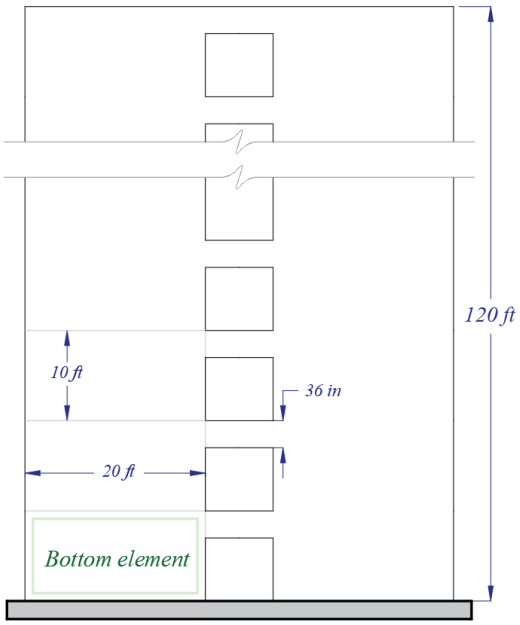

Figure 4-19 The coupled wall system analyzed in 4.8

The vertical reinforcement in the web is No. 6 bars spaced at 15 in. The wall has been designed with 60 ksi steel bars and 6 ksi concrete. In nonlinear modeling, the expected strength of the material is used by assuming an over strength factor of 1.3, according ASCE 41 recommendation.

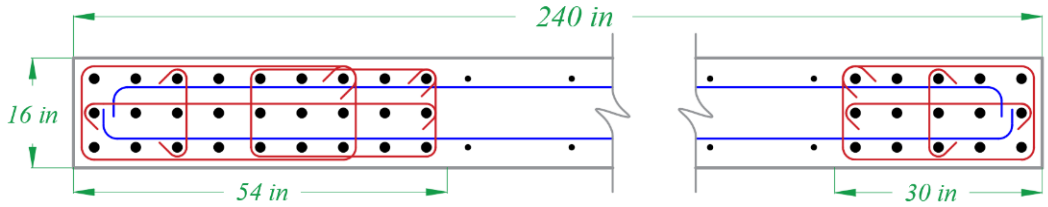

Figure 4-20 The cross section of wall piers of the coupled wall system in 4.8

The ground motion history used for dynamic analysis is RSN 20, with acceleration history shown in Figure 3-51. Each pier has a tributary area that takes 160 kips of gravity loads. This gravity load is applied as vertical point loads at the geometric centroid of each pier. The expected shear strength of each coupling beam is 350 kips per design. For the case of simplicity, all the coupling beams are assumed to have the same shear strength.

It will be discussed later, in 5.5, that the deformation parameters of the backbone curve need to be adjusted to account for distribution of nonlinearity above the bottom element. To do so, Eq. 5-28 requires the yield rotation of the element used in the study, and the element assumed in generating tables Table 4-1 and Table 4-2. Because both elements have the same height ($h_e = L_w/2 = 120\ in$), the yield rotations are equal. Note that the moment curvature curve, and the yield rotation of the piers are different in positive and negative directions because of the non-symmetric sections, and different axial loads. The elastic analysis for design of the system shows that the piers undergo a maximum compressive axial load of ~5,000 kips (With positive curvature in left pier, and negative curvature in right pier) and a maximum tensile axial load of ~1,500 kips in the opposite direction. The moment curvature diagram of the piers for the expected compressive axial load, and the expected tensile axial load are shown in Figure 4-21.

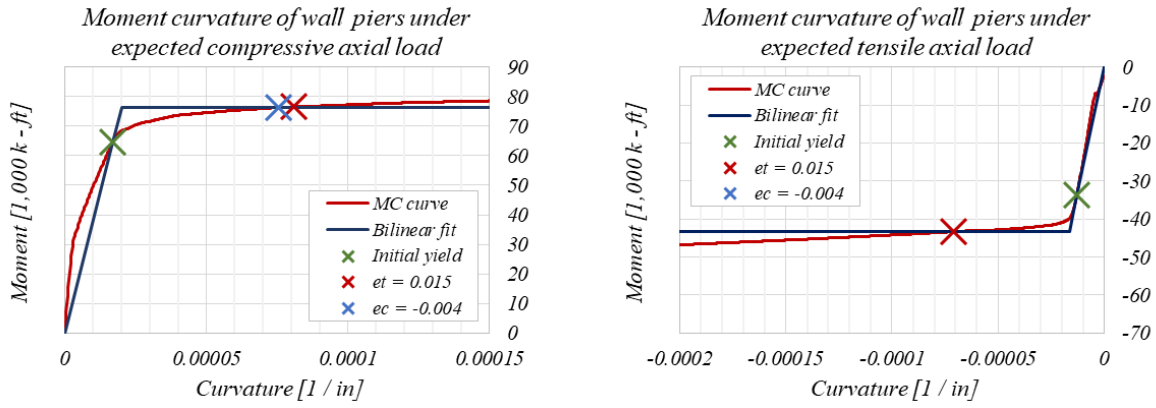

Figure 4-21 Moment curvature diagram of piers when they undergo compressive and tensile axial load

The yield curvature, φ_Y, yield moments, M_Y, and yield rotation, θ_Y, of the piers under expected compression and tension loads are listed here.

$$\varphi_Y^{Com} = 0.000020014\ \frac{1}{in}, \qquad M_Y^{Com} = 76{,}288\ kips - ft, \qquad \theta_Y^{Com} = 0.24017\%$$

$$\varphi_Y^{Ten} = 0.000016464\ \frac{1}{in}, \qquad M_Y^{Ten} = 43{,}317\ kips - ft, \qquad \theta_Y^{Ten} = 0.19756\%$$

The values of deformation parameter d in Table 4-1 are adjusted due to "*Distributed Nonlinearity*" modeling, and for expected axial compression load, using Eq. 5-28.

$$r = \frac{H_{BE}}{H_w} = \frac{1}{2}$$

$$0.032 \rightarrow (0.032 - 0.0024017)\frac{3}{4} + 0.0024017 = 0.024600$$

$$0.026 \rightarrow (0.026 - 0.0024017)\frac{3}{4} + 0.0024017 = 0.020100$$

$$0.018 \rightarrow (0.018 - 0.0024017)\frac{3}{4} + 0.0024017 = 0.014100$$

$$0.014 \rightarrow (0.014 - 0.0024017)\frac{3}{4} + 0.0024017 = 0.011100$$

Same calculations are done for the pier under expected tensile load.

$$0.032 \rightarrow (0.032 - 0.0019756)\frac{3}{4} + 0.0019756 = 0.024494$$

$$0.026 \rightarrow (0.026 - 0.0019756)\frac{3}{4} + 0.0019756 = 0.019994$$

$$0.018 \rightarrow (0.018 - 0.0019756)\frac{3}{4} + 0.0019756 = 0.013996$$

$$0.014 \rightarrow (0.014 - 0.0019756)\frac{3}{4} + 0.0019756 = 0.010994$$

Deformation parameters d and d' will be adjusted in the same way. These calculations are done inside the element, once the user specifies the yield curvature in positive and negative directions.

4.8.1 Analysis of results

The history of demands, over the first 10 sec of the excitation when seismic loads are more severe are presented in this section. The history of axial load, shear, and depth of compression zone are plotted. These are demands that control the deformation parameter of the backbone curve in Table 4-1 and Table 4-2. The roof drift history and the history of plastic hinge is also plotted in Figure 4-22 as reference. The load step at which deformation parameter d is exceeded and strength loss (SL) initiates, is marked with a blue line in the figures.

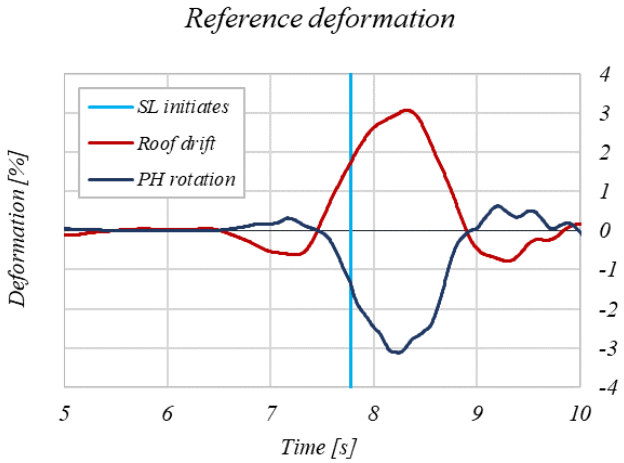

Figure 4-22 Right pier drift and plastic hinge rotation history

Figure 4-23 shows the history of compression zone depth normalized by wall length for the right pier. The roof drift, normalized by its maximum value over the ground motion is also shown for reference. The compression zone depth calculated based on concrete fibers' stress, steel fibers' stress, and the deformation-wise compression zone (Discussed in 4.5) are plotted separately.

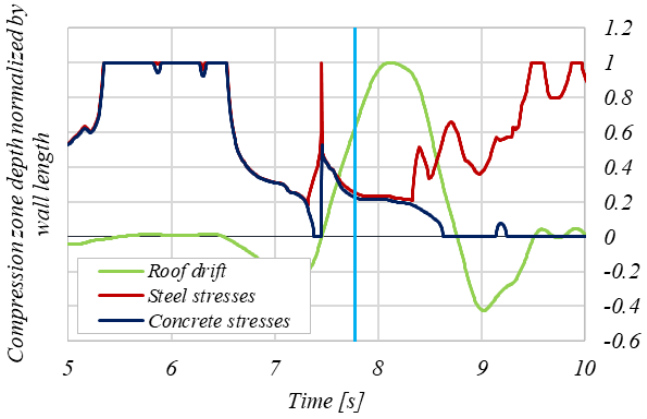

Figure 4-23 History of compression zone depth for the right pier

Note that for the initial phases of the ground motion, including the load step at which the element strength degradation initiates, the two values are close. But once residual deformations become large, the difference between the two become significant. Figure 4-24 shows the history of parameter λ, calculated based on both the concrete and steel compressive stresses.

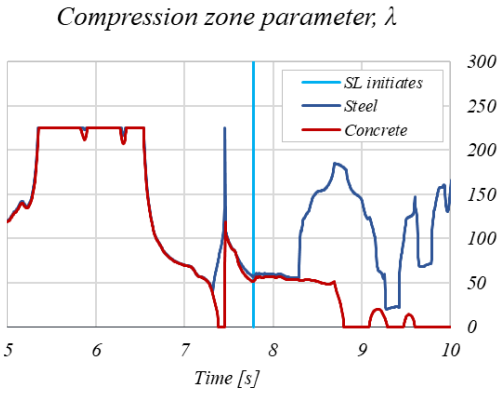

Figure 4-24 History of parameter, λ, for the right pier

Figure 4-25 shows the history of compression zone depth (normalized by dividing by the length of the wall) and shear stress (normalized by $\sqrt{f'_c}$) for the right pier. This shear stress is calculated within the element, using Eq. 3-3, and accounts for the dynamic effect of higher modes and the effect of flexural over strength.

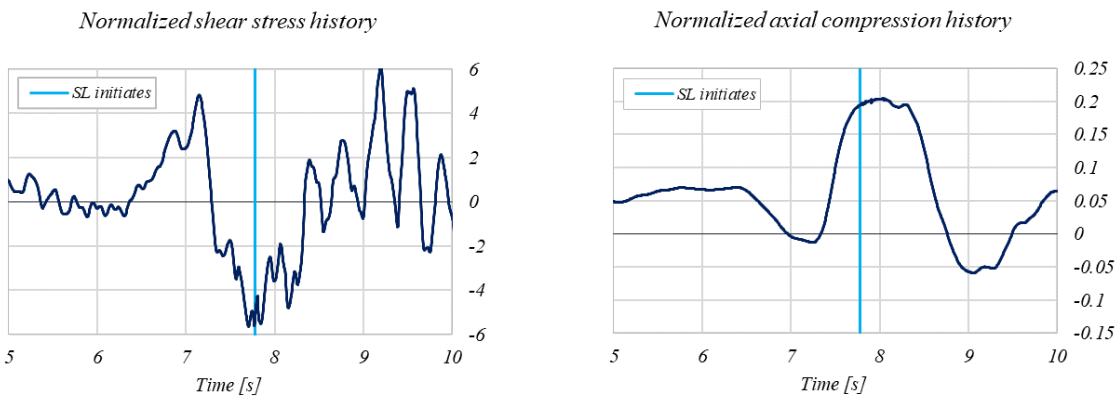

Figure 4-25 History of shear stress and axial load pf right pier

Due to a seismic pulse in a certain direction, one of the piers undergoes seismic compressive axial load, and the other pier undergoes seismic tensile axial load. The total axial load, and depth of compression zone is larger in the wall with more compressive force. The higher axial load, and larger depth of the compression zone initiates the strength degradation of the compressive pier earlier than the other one. In Figure 4-27, these two parameters are shown for the left and right pier in the same figure, alongside the time step at which the strength degradation (SL) initiates for the two piers.

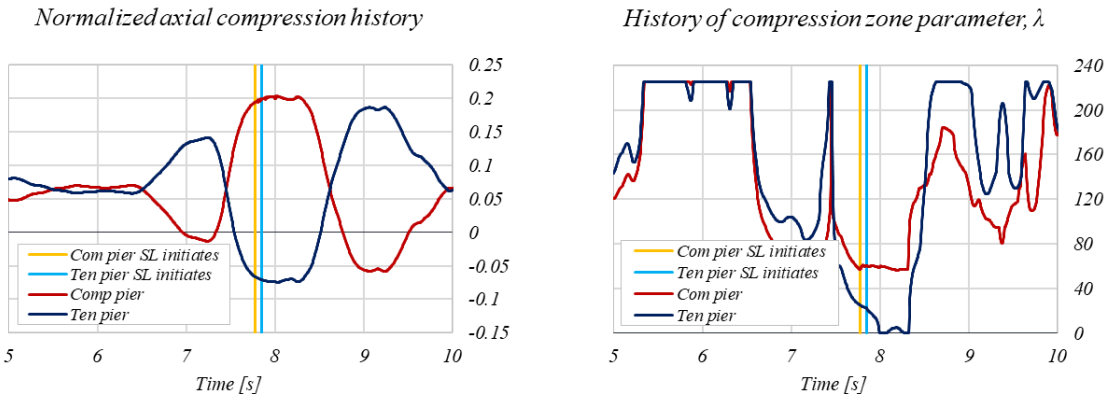

Figure 4-26 History of axial load and compression zone depth parameter for the two piers of the coupled wall system

The strength degradation of both piers takes place at almost the same time. This is partially due to the big pulse in the record in the 8th second. Also note that once the compressive pier loses its strength, the tensile pier takes more demand. This initiates the strength degradation of the tensile pier faster, when compared to the case where the compressive pier has remained intact. The response of the plastic hinge, with and without modeling strength degradation, for both piers is shown in Figure 4-27.

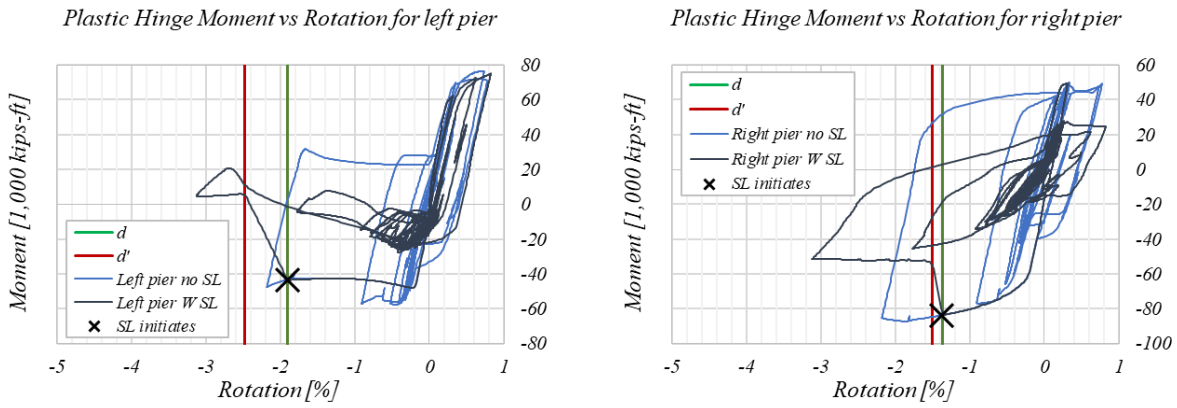

Figure 4-27 Plastic hinge response of the wall piers

The load step at which the strength loss initiates is indicated in the moment curvature curves. For the right pier, the plastic hinge rotation at this step is

$\theta_{SL} = 1.3685\ \%$

The normalized axial load, shear stress, and compression zone parameter at this load step, for the right pier, are as follows.

$p_u = 0.19703, \quad v_u = 5.6318, \quad \lambda = 56.854$

Note that $4 < v_u < 6$ and $10 < \lambda < 70$. This requires a double interpolation within the table to obtain deformation parameter d.

$$d_{RP} = \left(2.4600 + \frac{2.0100 - 2.4600}{6 - 4}(5.6318 - 4)\right) +$$

$$\frac{\left(1.1100 + \frac{1.1100 - 1.4100}{6 - 4}(5.6318 - 4)\right) - \left(2.4600 + \frac{2.0100 - 2.4600}{6 - 4}(5.6318 - 4)\right)}{70 - 10}(56.854 - 10)$$

$$= 1.3685\ \%$$

This is the exact rotation of the plastic hinge at which deformation parameter d is exceeded for the right pier. Deformation parameter d' of the right pier is obtained using the axial load, p_u, and the compression zone depth, λ, obtained at rotation d of the plastic hinge. A double interpolation through Table 4-2 turns d'.

$$d'_{RP} = \left(2.7600 + \frac{2.3100 - 2.7600}{0.2 - 0.1}(0.19703 - 0.1)\right) +$$

$$\frac{\left(1.1100 + \frac{1.1100 - 1.4100}{0.2 - 0.1}(0.19703 - 0.1)\right) - \left(2.7600 + \frac{2.3100 - 2.7600}{0.2 - 0.1}(0.19703 - 0.1)\right)}{70 - 10}(56.854 - 10)$$

$$= 1.3828\ \%$$

The rapid post-peak drop in element strength may cause numerical instability (). To avoid this, deformation parameter d' is assumed to be at least equal to $1.1 \times d$.

$$d'_{RP} = 1.1 \times 1.3685 = 1.5054\ \%$$

Deformation parameters of the Left Pier are calculated the same way, and are equal to

$$d_{LP} = 1.9023\ \%$$

$$d'_{LP} = 2.4730\ \%$$

Note in Figure 4-27 that the Strength degradation branch is wider in the tensile pier because of the more ductility due to the lower compression load.

Chapter 5 Plastic hinge length of flexure-controlled structural walls

To evaluate the performance of structural walls, ASCE 41 [2] assigns a backbone curve to the force deformation response of the bottom portion of the wall called the plastic hinge. To convert the top drift of a wall specimen to the corresponding deformation parameters (rotation) of the backbone curve, the height of the plastic hinge must be known. In addition to ASCE 41 criteria, some of the previous work on required ductility of structural members (Walls and Columns) associate the performance level to the maximum strain (Tensile and compressive) over the plastic hinge (Moehle and Wallace (1992) [51], Berry and Eberhard (2003) [27], Segura and Wallace (2018) [36]). Therefore, it is necessary to have a realistic estimate of the plastic hinge length for performance assessment of structural walls.

Abdullah and Wallace (2019) [47] assumed that the height of the plasticized zone is equal to the length of the wall ($H_{PZ} = L_w$), and the size of the plastic hinge is half the length of the wall ($l_p = L_w/2$). Other researchers, whose work will be reviewed in 5.2, have proposed different expressions. Some of these studies have been done using Finite analyses (Bohl (2006) [48], Zhao et al. (2011) [52], Kazaz (2013) [28]). Experimental studies, are either based on limited data, or there is little documentation regarding the number of tests and the reliability of the models. Recent wall tests, with instrumentation that enables us to measure the extent of nonlinearity, has motivated this study on the plastic hinge length of flexure-controlled structural walls. A database of 17 tested structural walls is assembled. The height of the plastic zones at peak deformation capacity (Point C in Figure 5-8) is calculated for each wall in the database and different expressions for plastic hinge zone are evaluated.

5.1 Description of the plastic hinge

Figure 5-1 shows a flexure-controlled wall deformed by a lateral load. As far as the moment caused by lateral load at the base of the wall is less than the flexural yielding capacity, the wall remains elastic and the flexural deformation (curvature) at any point over the wall height is proportional to the bending moment.

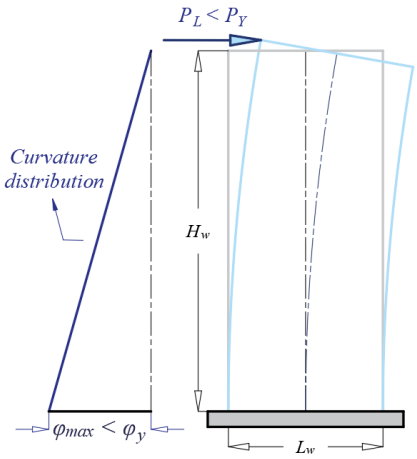

Figure 5-1 Wall loaded with lateral load less than the yield load

Once the bending moment at the base exceeds the yielding capacity, flexural deformation accumulates over a height H_{PZ} above the critical section, called the plasticized zone as shown in Figure 5-2(a). The curvature distribution is also shown in this figure.

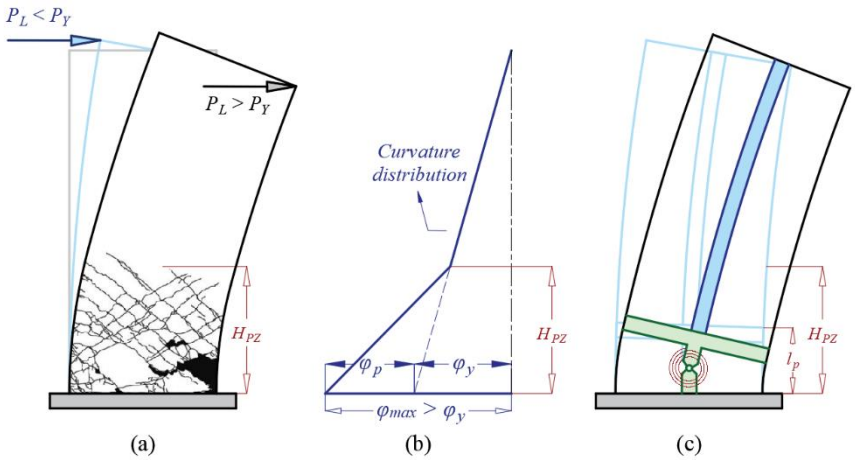

Figure 5-2 (a) Wall loaded with lateral load more than the yield load, (b) Curvature distribution over the wall height, (c) A simple model of the wall

In a simple nonlinear model, like the one shown in Figure 5-2(c), it is assumed that the entire nonlinear action occurs in the bottom portion of the wall, called the plastic hinge, and a nonlinear element is used over this portion in the model. The height of this bottom portion, denoted by l_p, is generally a fraction of the actual plasticized zone. Above the plastic hinge, the wall is modeled by an elastic beam-column element, and therefore, is enforced to remain elastic. In 5.3, it will be shown that for the average curvature of the model's nonlinear element (Figure 5-2 (c)) to be equal to the maximum curvature at the base of the prototype, the height of the nonlinear element must be half of the height of the plasticized zone.

$$l_p = H_{PZ}/2$$

Analyses in literature generally assume the model in Figure 5-2 (c) to calculate average demand over the plastic hinge (curvature or strain) from wall drift. Section 5.5 of this chapter shows the calculations for a Distributed Nonlinearity model, which is used in case studies of Chapter 3 and Chapter 4.

5.2 Literature review

This section describes some of the previous research on the plastic hinge length of RC walls and other structural elements.

5.2.1 Park and Paulay (1975) [24]

In their textbook, the authors refer to the work by other researches for plastic hinge of RC members. Baker has proposed Eq. 5-1 for plastic hinge length of RC members with unconfined concrete.

$$l_p = k_1 k_2 k_3 \left(\frac{Z}{d}\right)^{\frac{1}{4}} d \qquad \text{Eq. 5-1}$$

In Eq. 5-1, k_1 is 0.7 for mild steel and 0.9 for cold worked steel. k_2 depends on axial load and is obtained from Eq. 5-2, where P_u is axial load on the member and P_0 is the pure axial capacity. k_3 is 0.6 for $f'_c = 5100\,psi$, and 0.9 when $f'_c = 1700\,psi$. f'_c is 0.85 times the cube strength of concrete. z is the effective length (Distance between the critical section to the point of counter flexure), and d is the effective depth of the member.

$$k_2 = 1 + 0.5\frac{P_u}{P_0} \qquad \text{Eq. 5-2}$$

For members with confined concrete, Baker has proposed Eq. 5-3, where c is the depth of compression zone at ultimate capacity, and other coefficients are as defined for Eq. 5-2.

$$l_p = 0.8k_1k_3\left(\frac{z}{d}\right)c \qquad \text{Eq. 5-3}$$

Based on tests on simply supported beams, Corley has proposed Eq. 5-4 for length of plastic hinge.

$$l_p = 0.5d + 0.2\sqrt{d}\left(\frac{z}{d}\right) \qquad \text{Eq. 5-4}$$

In discussion of Corley's work, Mattock proposed Eq. 5-5 that has a simpler form and fits the experimental data well.

$$l_p = 0.5d + 0.05z \qquad \text{Eq. 5-5}$$

Sawyer has also proposed equation Eq. 5-6 for the effective length of plastic hinge.

$$l_p = 0.25d + 0.075z \qquad \text{Eq. 5-6}$$

5.2.2 Paulay and Priestley (1992) [25]

Paulay and Priestley obtained Eq. 5-7 to correlate the roof displacement ductility, μ_Δ, of a cantilever, to the curvature ductility, μ_φ, of the wall section.

$$\mu_{\Delta} = 1 + 3(\mu_{\varphi} - 1)\frac{l_p}{l}\left(1 - 0.5\frac{l_p}{l}\right) \qquad \text{Eq. 5-7}$$

In this equation, l_p is the height of the plastic hinge, and l is the shear span of the wall (Distance from the point of effective lateral load to the base). For a triangular distribution of lateral load, l is ⅔ of the total height. Eq. 5-7 was originally developed for columns and is based on a curvature diagram shown in Figure 5-3 (e), where it is assumed that the plastic curvature is concentrated over the plastic hinge, with height l_p above the base. To account for the base rotation due to penetration of strain through the foundation, the plastic hinge is extended below the wall base, and the new height of the plastic hinge is denoted by l'_p.

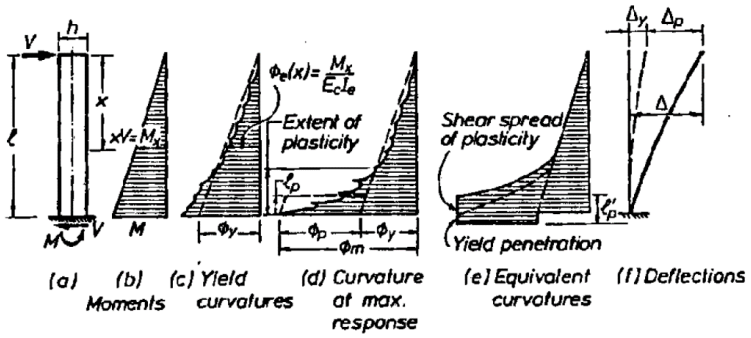

Figure 5-3 Distribution of curvature over the wall by Paulay and Priestley (1992)

The authors recommend the expression in Eq. 5-8 to obtain the height of the plastic hinge.

$$l_p = 0.08l, \qquad l'_p = l_p + 0.15d_b f_y \qquad \text{Eq. 5-8}$$

In Eq. 5-8, l, is the shear span, and the second term of l'_p ($0.15d_b f_y$) accounts for the base rotation due to strain penetration. Paulay and Priestley also proposed Eq. 5-9 for plastic hinge height of RC walls.

$$l_p = 0.2l_w + 0.044h_e \qquad \text{Eq. 5-9}$$

In Eq. 5-9, $h_e = l$ is the effective height. Note that this equation does not have the strain penetration term. Priestley and Kowalsky compared the values obtained for the plastic hinge size, by the two equations in Figure 5-4. A triangular distribution of lateral loads was assumed in this figure.

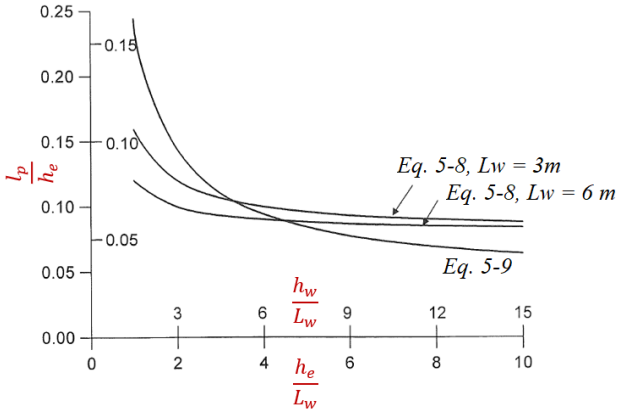

Figure 5-4 Comparison of Eq. 5-8 and Eq. 5-9 by Priestley and Kowalsky

5.2.3 Berry and Eberhard (2005) [27]

Berry and Eberhard worked on an expression that estimates the lateral displacement at which buckling of longitudinal bars of a column initiates. To achieve that, the authors first proposed an expression to estimate the curvature of a column section at initiation of bar buckling. To convert this curvature to a corresponding plastic hinge rotation, and then a corresponding top lateral displacement, expression in Eq. 5-10 for the height of plastic hinge columns was proposed.

$$L_p = \alpha L + \beta D + \xi f_y d_b \qquad \text{Eq. 5-10}$$

In Eq. 5-10, L is the effective height of the column. The term αL considers the effect of moment gradient, and βD considers the effect of section depth. The term $\xi f_y d_b$ accounts for the base rotation.

The results of this research, only turns the plastic hinge rotation at buckling and the coefficients of plastic hinge length, α, β, and ξ were not derived. But Eq. 5-10 provides a general form which is adopted by many researchers to work on equations for the size of the plastic hinge.

5.2.4 Kazaz (2013) [28]

Kazaz did a parametric study using a finite element model to estimate the height of the plasticized zone for cantilever walls. Figure 5-5 shows the overview of the finite element model used in the study.

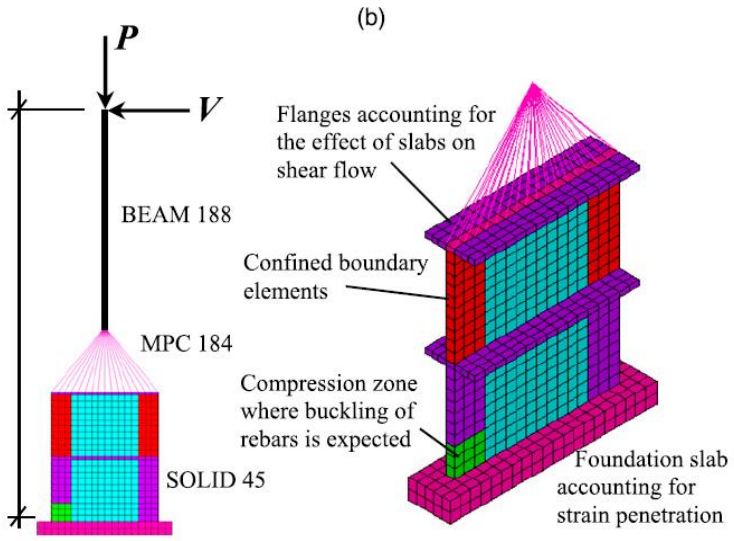

Figure 5-5 Finite element model of cantilever walls in study by Kazaz

The accuracy of the model was calibrated and verified by predicting the response of specimen RW2 tested by Thomsen and Wallace, as shown in Figure 5-6.

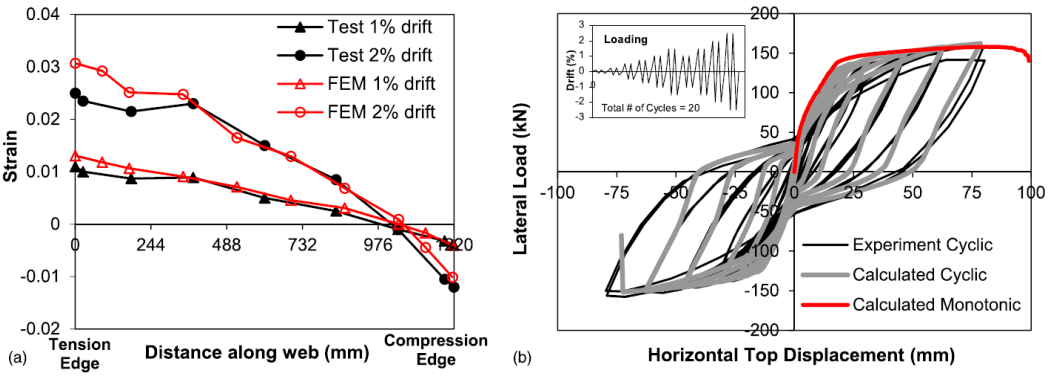

Figure 5-6 Verification of the finite element model by Kazaz

The varying parameters in his study, with the range of their values are listed in Table 5-1.

Table 5-1 Summary of variables in the parametric study by Kazaz

Parameter	*Unit*	*Range of values*
Wall length, L_w	*m*	*3, 5, 8*
Effective height, H_e	*m*	*5, 6, 9, 15, 24*
Wall aspect ratio, H_e/L_w	-	*0.75, 0.125, 1.2, 1.8, 1.875, 2, 3, 4.8, 5, 8*
Wall axial load ratio, $P_u/A_g f'_c$	-	*0.02, 0.05, 0.1, 0.15, 0.25*
Boundary element reinforcement ratio, ρ_b	-	*0.005, 0.01, 0.02, 0.04*

The Proposed equation to estimate the size of the nonlinear zone is shown in Eq. 5-11.

$$L_{pz} = 0.60 L_w \left(1 - \frac{P}{A_w f'_c}\right)\left(1 - \frac{f_y \rho_{sh}}{f'_c}\right)\left(\frac{M/V}{L_w}\right)^{0.5} \qquad \text{Eq. 5-11}$$

Three remarks from this study are listed here.

- Unlike previous equations, the shear reinforcement ratio, ρ_{sh}, is a controlling parameter.
- Although Figure 5-5 mentions the foundation slab accounts for strain penetration, the finite element analysis does not show any yielding of the reinforcement in the foundation. This seems to be the case for any finite element model in which a perfect cohesion between the steel continuum and the adjacent concrete continuum is assumed. Therefore, slippage and extension of bars is not modeled.
- The model is verified by comparing the strain profile over the bottom 9-in. segment of the model, with the strain profile obtained by the LVDTs installed over the bottom 9-in. of specimen RW2 tested by Thomson and Wallace (1995) [22]. Note that the bottom pin of the LVDTs is on the footing (Figure 5-7). So, these LVDTs measure the base rotation in addition to the deformation of the bottom 9 inch of the wall. The finite element model does not measure any base rotation. So, comparing the two seems questionable.

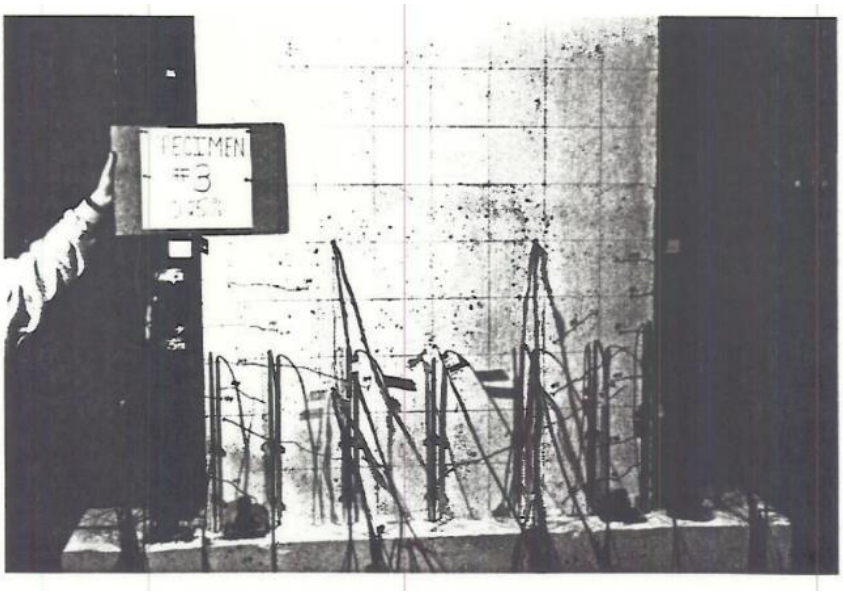

Figure 5-7 LVDTs installed on specimen RW2 tested by Thomsen and Wallace (1995)

5.3 Obtaining properties of model's nonlinear element from test data

Assume a flexurally-controlled wall model is tested in the lab. The wall specimen has a cross-section with t_w thickness, L_w length. The total height of the wall is H_w. The specimen is loaded with cyclic lateral point load, denoted by P_L, at the top. Figure 5-8 shows the envelope of the hysteretic force deformation curve.

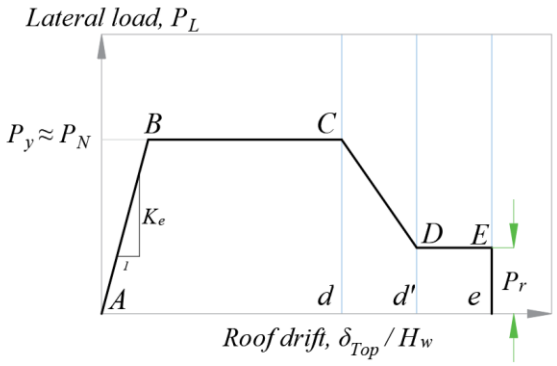

Figure 5-8 Experimental force deformation envelope of a wall specimen

The specimen prototype, and the mechanical model are shown in Figure 5-9.

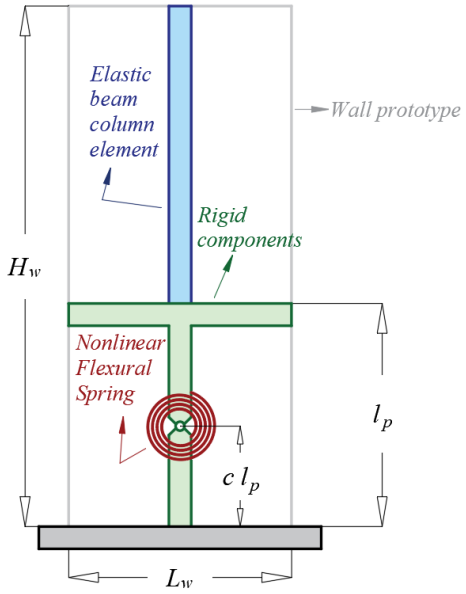

Figure 5-9 A wall specimen and the mechanical model

The nonlinear flexural response of the wall is captured by a nonlinear element, with a height of l_p. This element is comprised of flexurally/axially rigid components, connected by a nonlinear flexural spring located at cl_p from the critical section. The nonlinearity of the wall is entirely captured by this spring. The purpose of this chapter is to find parameters of the backbone curve, shown in Figure 5-10, and the shear stiffness of the nonlinear element, so that the envelope of the force deformation curve predicted by the model matches the envelope of the force deformation curve obtained in the test. These parameters are the stiffness of the elastic part, K_{NLE}, and the deformation parameters, d_{FS}, d'_{FS}, and e_{FS}. The shear stiffness of model will also be computed.

5.3.1 The shear stiffness of the model

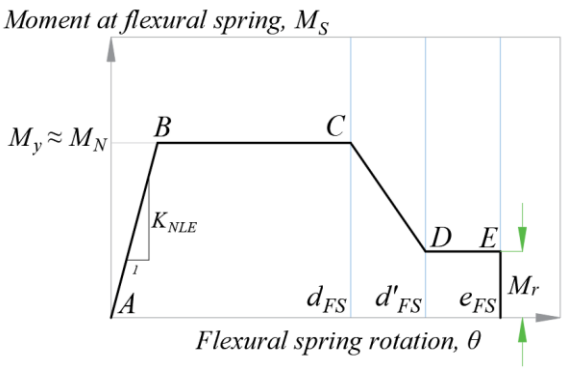

Figure 5-10 Backbone curve of model's flexural spring

It is assumed that the wall's shear response is elastic. If so, the deformation of the wall due to shear response is shown in Figure 5-11.

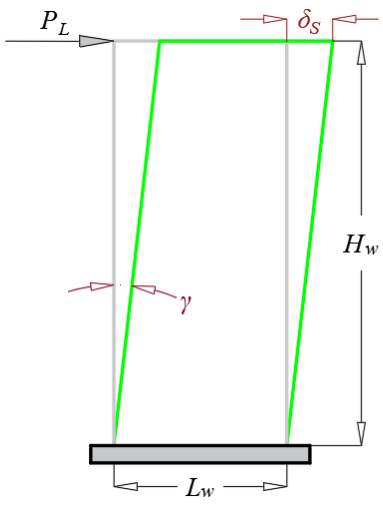

Figure 5-11 Shear deformation of a wall specimen under constant shear

Since the shear force is constant over the wall height, the shear distortion, γ, is also constant over the wall height. Knowing the shear distortion, γ, from top lateral displacement, the shear stiffness, K_S, is calculated in Eq. 5-12.

$$\gamma = \frac{\delta_S}{H_w}, \qquad \gamma = \frac{v_u}{G_e} = \frac{P_L}{t_w L_w G_e}, \qquad K_S = \frac{t_w L_w G_e}{H_w} \qquad \text{Eq. 5-12}$$

In Eq. 5-12, δ_S is the top lateral shear displacement of the wall. G_e is the effective shear modulus. The effective shear modulus is the gross shear modulus, G_g, multiplied by a factor, α_S, to account for concrete cracking.

$$G_e = \alpha_S G_g \qquad \text{Eq. 5-13}$$

In a computer program used for modeling the wall, the stiffness K_S is assigned to a uniaxial material that will later be aggregated with the wall's elastic component and the nonlinear element in the bottom. Another approach is to use an elastic horizontal spring for the nonlinear element, and K_S would be the stiffness of this spring.

Once the effective stiffness factor is known, the shear stiffness is calculated using the geometry of the wall. Calculating this factor from test data will be done in 5.3.2.

5.3.2 Calculation of the effective elastic stiffness factor of the wall from test data

An approximate flexural deformation of the wall due to a lateral point load at the top is shown in Figure 5-12. For now, assume that the lateral load is smaller than the load required for yielding the section, P_y.

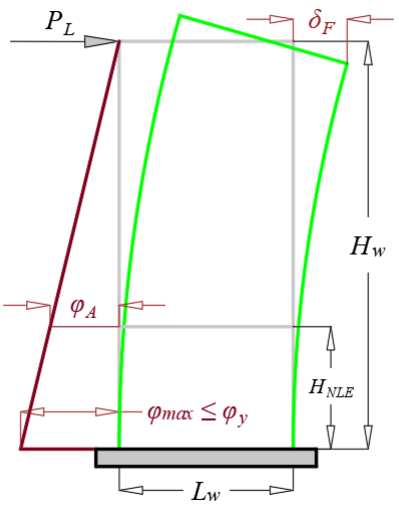

Figure 5-12 Flexural deformation of a wall specimen due to a lateral point load at the top

The roof lateral displacement due to flexural deformation, δ_f, and the flexural stiffness of the wall is given in Eq. 5-14.

$$\delta_F = \frac{P_L {H_w}^3}{3EI_e}, \qquad K_F = \frac{3EI_e}{{H_w}^3} \qquad \text{Eq. 5-14}$$

In Eq. 5-14, EI_e is the effective flexural stiffness of the wall. The effective flexural stiffness is the gross flexural stiffness, EI_g, multiplied by a factor, α_F, to account for concrete cracking.

$$EI_e = \alpha_F EI_g \qquad \text{Eq. 5-15}$$

It is assumed that the flexural stiffness reduction factor, α_F, and the shear stiffness reduction factor, α_S, are equal. Eq. 5-16 then, turns the effective stiffness of the wall in terms of $\alpha = \alpha_S = \alpha_F$, considering both the flexural and shear deformations. Knowing K_e from the envelope of Figure 5-8, the effective stiffness factor, α, is calculated.

$$K_e = \frac{P_L}{\frac{\delta_T = \delta_F + \delta_S}{H_w}} = \frac{P_L}{\frac{P_L {H_w}^2}{3\alpha E I_g} + \frac{P_L}{t_w L_w \alpha G_g}} = \frac{1}{\frac{{H_w}^2}{3\alpha E I_g} + \frac{1}{t_w L_w \alpha G_g}}, \qquad \alpha = K_e \left(\frac{{H_w}^2}{3EI_g} + \frac{1}{t_w L_w G_g} \right) \quad \text{Eq. 5-16}$$

The flexural and shear stiffness properties assigned to the elastic portion of the model must incorporate this effective stiffness factor.

5.3.3 Calculation of the elastic stiffness of the flexural spring's backbone curve, K_{NLE}

The initial elastic segment of the backbone curve in Figure 5-10 accounts for the elastic deformation of the portion of the wall that the nonlinear element represents. To calculate this, the curvature of the prototype at the top and at the bottom of the nonlinear element, φ_A and φ_{max}, are obtained in Eq. 5-17 for a lateral load smaller than the yield load, P_y.

$$\varphi_{max} = \frac{P_L H_w}{E I_e}, \qquad \varphi_A = \frac{P_L [H_w - l_p]}{E I_e} \quad \text{Eq. 5-17}$$

In Eq. 5-17, l_p is the height of the nonlinear element, shown in Figure 5-9. Knowing these two curvatures, the rotation of the prototype at the top of the nonlinear element is obtained in Eq. 5-18.

$$\theta_{l_p} = \left[\frac{\varphi_{max} + \varphi_A}{2} \right] l_p = \frac{P_L \left[H_w - \frac{l_p}{2} \right]}{E I_e} l_p \quad \text{Eq. 5-18}$$

The elastic stiffness of the flexural spring, K_{NLE}, is calculated so that the nonlinear element produces the same rotation as in Eq. 5-18 at the top of the nonlinear element. Eq. 5-19 shows the moment at the location of the flexural spring.

$$M_S = P_L \left[H_w - \frac{l_p}{2} \right] \quad \text{Eq. 5-19}$$

The elastic stiffness of the nonlinear element is calculated in Eq. 5-20, so that the moment in Eq. 5-19 produces the same rotation that the prototype observes (Eq. 5-18).

$$K_{NLE} = \frac{M_S}{\theta_{l_p}} = \left(\frac{P_L[H_w - cl_p]}{\frac{P_L\left[H_w - \frac{l_p}{2}\right]}{EI_e} l_p} \right) = \frac{EI_e}{l_p}\left(\frac{1 - cq}{1 - \frac{q}{2}}\right), \qquad q = \frac{l_p}{H_w} \qquad \text{Eq. 5-20}$$

5.3.4 Calculation of the deformation parameters of the backbone curve, d_{FS}, d'_{FS}, e_{FS}

The force deformation envelope of Figure 5-8 shows that once the wall yields, it starts deforming freely with no increase in lateral load. The flexural plastic deformation is due to accumulation of plastic curvature over the bottom portion of the wall, called the plasticized zone. Figure 5-13 shows the distribution of curvatures over the plasticized zone, and the segment of the wall above that.

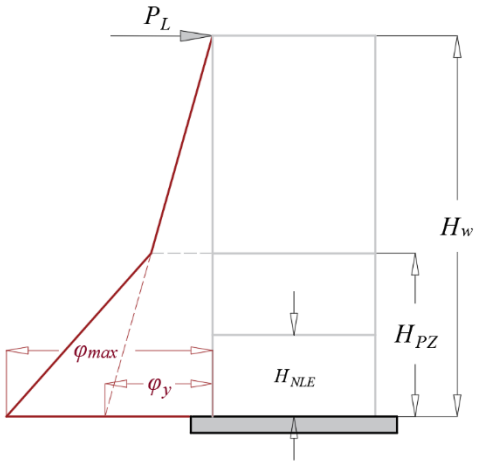

Figure 5-13 Distribution of curvature over the wall after yielding

In the model, a constant plastic curvature is assumed over the bottom nonlinear element, with a magnitude equal to the maximum plastic curvature at the base, $\varphi_p = \varphi_{max} - \varphi_y$. On the other hand, the distribution of plastic curvature is linear over the plasticized zone of the prototype. The two curvature distributions are shown in Figure 5-14.

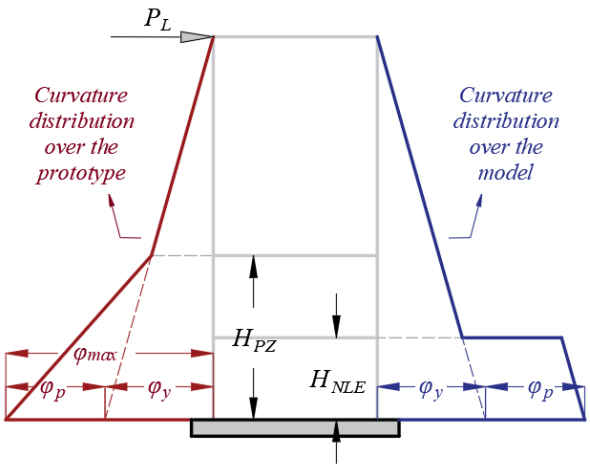

Figure 5-14 post-Yield curvature distribution over the prototype and the model due to a lateral point load

If the constant plastic curvature of the nonlinear element is aimed to be equal to the that at the base of the prototype, height of the nonlinear element must essentially be equal to half of the plasticized zone (Eq. 5-21).

$$l_p = \frac{H_{PZ}}{2} \qquad \text{Eq. 5-21}$$

The roof drift due to the plastic curvature over the nonlinear element is given in Eq. 5-21.

$$\frac{\delta_p}{H_w} = \varphi_p l_p \left(1 - \frac{l_p}{2H_w}\right) = (\varphi_{max} - \varphi_y) l_p \left(1 - \frac{q}{2}\right), \qquad q = \frac{l_p}{H_w} \qquad \text{Eq. 5-22}$$

Using the plastic hinge length of Eq. 5-21, the rotation parameters of the backbone curve is calculated in Eq. 5-23.

$$d_{FS} - \frac{M_y}{K_{NLE}} = \frac{d - \frac{P_Y}{K_e}}{\left(1 - \frac{l_p}{2H_w}\right)}, \qquad d'_{FS} - \frac{M_y}{K_{NLE}} = \frac{d' - \frac{P_Y}{K_e}}{\left(1 - \frac{l_p}{2H_w}\right)}, \qquad e_{FS} - \frac{M_y}{K_{NLE}} = \frac{e - \frac{P_Y}{K_e}}{\left(1 - \frac{l_p}{2H_w}\right)}$$

$$d_{FS} = \frac{d - \frac{P_Y}{K_e}}{\left(1 - \frac{l_p}{2H_w}\right)} + \frac{M_y}{K_{NLE}}, \qquad d'_{FS} = \frac{d' - \frac{P_Y}{K_e}}{\left(1 - \frac{l_p}{2H_w}\right)} + \frac{M_y}{K_{NLE}}, \qquad e_{FS} = \frac{e - \frac{P_Y}{K_e}}{\left(1 - \frac{l_p}{2H_w}\right)} + \frac{M_y}{K_{NLE}} \qquad \text{Eq. 5-23}$$

The moment capacity of the flexural spring, M_Y, is in Eq. 5-24.

$$M_Y = P_Y\left(H_w - \frac{l_p}{2}\right)$$ Eq. 5-24

To obtain the properties of the model, it is necessary to know the plasticized zone.

5.4 Calibrating the shear wall's backbone curve for a different element size

By statistical analysis on a database of more than 1,000 tested structural wall specimens, Abdullah and Wallace derived equations that determine the deformation parameters of a backbone curve that can be used for the flexural spring of the shear wall model in Figure 4-7. The authors also generated Table 4-1 and Table 4-2 that can alternatively be used to determine deformation parameters. In their work, a similar approach to the one discussed in 5.3 was used to convert the top lateral displacement of each specimen to the corresponding deformation parameter of the plastic hinge. Note that not all specimens are models of an entire wall. Some (Including specimens tested by Wallace and Segura) are wall panels, that represent only the bottom portion of the prototype. In this case, new formulations need to be derived to convert a wall panel's top rotation to deformation parameters of the flexural spring in the model.

Analyses done by Abdullah and Wallace assumes the height of the plasticized zone is equal to the length of the wall (Eq. 5-25). The size of the nonlinear element is hence equal to half the length of the wall.

$$H_{PZ} = L_w, \qquad l_p = \frac{H_{PZ}}{2} = \frac{L_w}{2}$$ Eq. 5-25

Note that researchers have proposed different equations for the nonlinear height of structural walls. As shown in 5.3.4, deformation parameters of the flexural spring depend on the size of the nonlinear element. To convert the deformation parameters calculated using a pre-assumed size of

the nonlinear element, l_p^1, to the deformation parameters for a nonlinear element with a different size, l_p^2, Eq. 5-26 is used.

$$d_{FS}^2 = \frac{\left(d_{FS}^1 - \frac{P_Y\left(H_w - \frac{l_p^1}{2}\right)l_p^1}{EI_e}\right)\left(1 - \frac{l_p^1}{2H_w}\right)}{\left(1 - \frac{l_p^2}{2H_w}\right)} + \frac{P_Y\left(H_w - \frac{l_p^2}{2}\right)l_p^2}{EI_e} \qquad \text{Eq. 5-26}$$

Eq. 5-26 is derived with the assumption that both models produce the same roof drift at a certain rotation of the plastic hinge. Other parameters of the backbone curve d'^2_{FS} and e^2_{FS} can be calculated using the same expression.

5.5 Calibrating parameters of the backbone curve for a model with distributed nonlinearity

The wall element used in Figure 5-9 uses elastic beam column elements above the nonlinear bottom element. This approach enforces all the nonlinear action to accumulate within the plastic hinge. Although the portion of the wall within the plasticized zone and above the plastic hinge becomes nonlinear in the prototype, the model enforces an elastic response in this zone. In a practice, the entire wall is modeled using nonlinear elements with fiber sections, such as the MVL element. Figure 5-15 shows the distribution of curvature for a nonlinear model with fiber section. The curvature distribution for the model shown in Figure 5-9 is also shown for comparison.

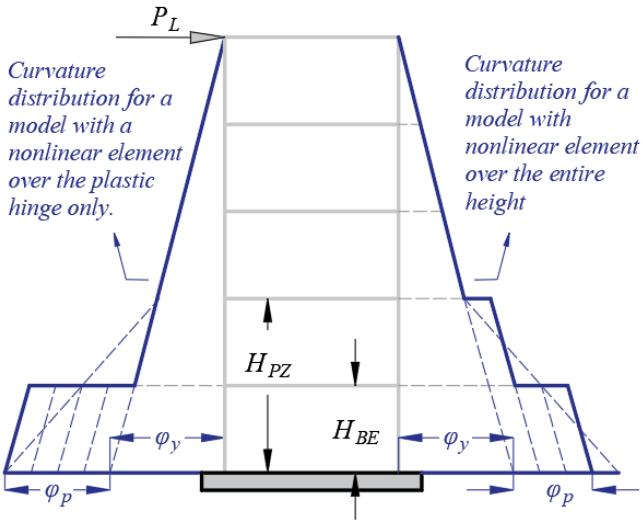

Figure 5-15 Post – yield curvature distribution over the wall prototype and the model due to a lateral point load

The wall is modeled with two elements over the nonlinear zone. Unlike the model shown in Figure 5-9, the element above the plastic hinge (The most bottom element) captures the nonlinear response. Therefore, the backbone curve assigned to the plastic hinge element has to be calibrated accordingly. It is assumed that the elastic flexural stiffness of the nonlinear element with fiber section, is equal to the elastic flexural stiffness elements used in the model of Figure 5-9. So, a similar distribution of curvature is observed in both models when the lateral load is smaller than the yield load. For lateral loads beyond yielding (Assume a deformation-controlled loading scheme), the plastic curvature in the bottom element, φ_p, for the MVL element is ¾ of the plastic curvature observed in the model of Figure 5-9. The areas enclosed by the curvature distributions in Figure 5-15 justifies the ¾ factor. To convert the deformation parameter *d* of the backbone curve used in model of Figure 5-9, to deformation parameter of the backbone curve that is assigned to an MVL element, Eq. 5-27 is used.

$$d_{MVLE} - \frac{M_y}{K_{MVLE}} = \frac{3}{4}\left(d_{FS} - \frac{M_y}{K_{NLE}}\right) \qquad \text{Eq. 5-27}$$

Note that in equation above, the term M_y/K_{MVLE} is the elastic rotation of the plastic hinge. In practice, it might be necessary to use an element size other than half the plasticized zone. For instance, the size of the plastic hinge might be calculated to be more than the height of the first story. In this case, Eq. 5-28 finds the deformation parameters of the backbone curve for any size of the MVL element that is a fraction of the height of the plasticized zone.

$$d_{MVLE} - \frac{M_y}{K_{MVLE}} = \left(d_{FS} - \frac{M_y}{K_{NLE}}\right) 2r \left(1 - \frac{r}{2}\right), \qquad r = \frac{H_{BE}}{H_{PZ}} \qquad \text{Eq. 5-28}$$

In Eq. 5-28, H_{BE} is the size of the bottom element.

Other deformation parameters would be found in the same way.

5.6 An experimental study on the plasticized height of RC structural walls

To study the plasticized height of structural walls, a database of 17 wall specimens, tested in 3 programs was assembled. The data of the tests are obtained from the DESIGNSAFE database [41]. Table 5-2 summarizes the general properties of the tested specimens.

Table 5-2 General properties of the wall specimens in the database

Specimen Name	L_w	H_e	$p_u = P_u/A_g f'_c$	F_y^l	d_b^l	*Researchers*
	in	*in*	*%*	*ksi*	*in*	
RW-A20-P10-S38	*48*	*96*	*7.3*	*68.4*	*0.5*	*Tran and Wallace (2012) [40][39]*
RW-A20-P10-S63	*48*	*96*	*7.3*	*69.2*	*0.75*	
RW-A15-P10-S51	*48*	*72*	*7.7*	*68.4*	*0.5*	
RW-A15-P10-S78	*48*	*72*	*6.4*	*68.7, 69.2*	*0.625, 0.75*	
RW-A15-P25-S64	*48*	*72*	*1.6*	*68.7, 69.2*	*0.625, 0.75*	
WP1	*90*	*331*	*9.641*	*73.4, 77*	*0.5, 0.625*	*Segura and Wallace (2017) [34][36]*
WP2	*90*	*330*	*8.363*	*73.4, 77*	*0.5, 0.625*	
WP3	*90*	*330*	*8.139*	*73.4, 77*	*0.5, 0.625*	
WP4	*90*	*541*	*6.369*	*76.9, 77*	*0.75, 0.625*	
WP5	*90*	*321*	*8.035, 6.423*	*70.9, 74.1*	*0.625, 0.5*	
WP6	*90*	*321*	*7.452*	*70.9*	*0.625*	
WP7	*90*	*321*	*5.294*	*70.9*	*0.625*	
WSH2	*78.74*	*178*	*5.199*	*89.92*	*0.395*	*Dazio et al. (1999) [43][42]*
WSH3	*78.74*	*178*	*5.334*	*87.17*	*0.479*	
WSH4	*78.74*	*178*	*5.184*	*83.54*	*0.477*	
WSH5	*78.74*	*178*	*12.27*	*84.7*	*0.32*	
WSH6	*78.74*	*179.5*	*10.34*	*83.54*	*0.477*	

The selected specimens are flexure-controlled. Specimens RW-A15-P10-S51, RW-A15-P10-S78, and RW-A15-P25-S64 tested by Tran and Wallace have an aspect ratio of 1.5, smaller than 2, which is the threshold considered in ACI 318 for flexure-controlled walls. But these specimens failed in a ductile mode because of the confinement over the boundary element. So, these tests were also included in the database.

In Table 5-2, L_w is the length of the wall, H_e is the effective height, p_u is the axial load ratio on the section, F_y^l is the yield strength, and d_b^l is the diameter of the longitudinal bars in the boundary element. Some cells in Table 5-2 contain two numbers. Specimen WP5 was loaded with different axial loads in positive and negative directions. Specimens RW-A15-P10-S78, RW-A15-P25-S64, and specimens WP1 through WP5 had longitudinal reinforcement with different bar diameter and yield strengths in their boundary elements. More details about the specimens will be shown in appendix.

5.6.1 Measuring the curvature distribution over specimens

The walls in the database used in this study were selected because they were well instrumented and the data of instrumentation was available in the literature. This instrumentation includes Linear Variable Differential Transformers (LVDTs), that measure the displacement between two points on the wall due to the deformation of wall.

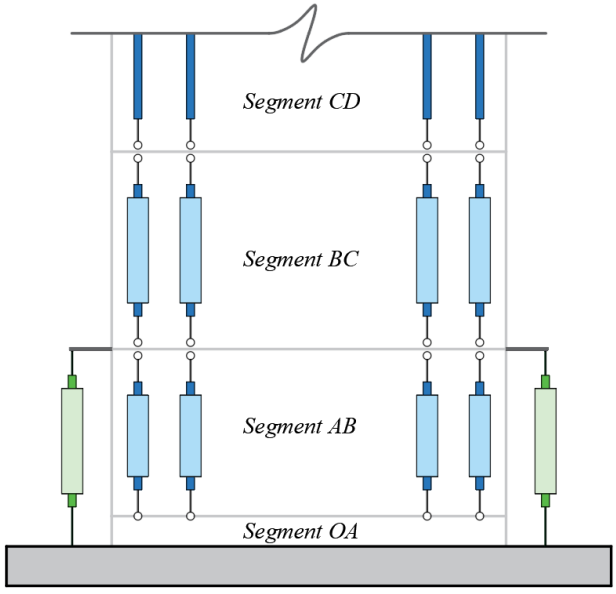

Figure 5-16 Typical layout of LVDTs over a wall specimen in the database

By calculating the displacement between the two pins of LVDT, δ, the average strain over this length is calculated according to Eq. 5-29.

$$\varepsilon = \frac{\delta}{L} \qquad \text{Eq. 5-29}$$

In Eq. 5-29, L is the initial length between the two pins of an LVDT.

Figure 5-16 shows the layout of LVDTS on a typical wall specimen. The series of four blue LVDTs mounted over each segment of the wall calculates the strains at four points, along the length of the wall. A linear regression between strain of these points is used to calculate the average curvature over each segment. By using another linear regression, over segments with curvature ductility more than 1, the bottom line of the bilinear curve is established (The red line in Figure 5-17). This line determines the height of the plasticized zone, H_{PZ}. The top of the plasticized zone is where the curvature ductility is equal to the value shown in Eq. 5-30.

$$\mu_\varphi = \frac{\varphi}{\varphi_Y} = 1 - \frac{H_{PZ}}{H_w} \qquad \text{Eq. 5-30}$$

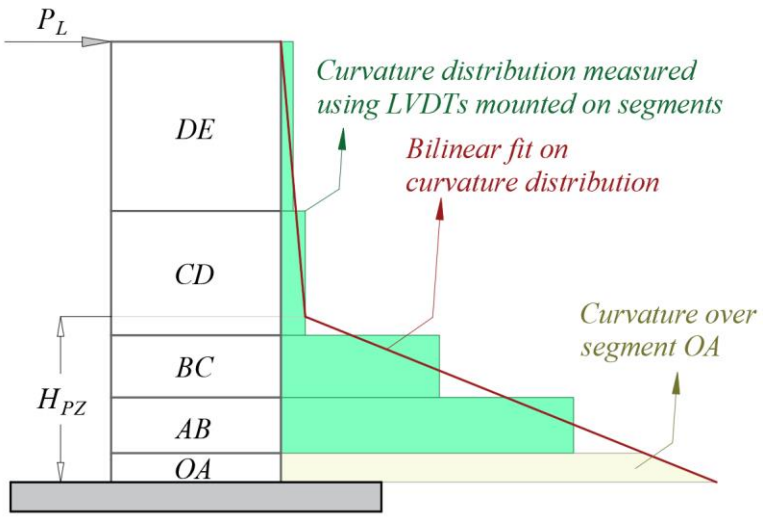

Figure 5-17 Curvature distribution measured by LVDTs and the bilinear fit over a tested wall specimen

The bottom line of the bilinear curve also determines the curvature distribution over the most bottom segment (i.e., Segment OA).

To complete the bilinear curve the point at the top of the plasticized zone is connected to the point with zero curvature at the effective height. This process is demonstrated in Figure 5-17.

5.6.2 Measuring the base rotation

The two green LVDTs on either side of the wall in Figure 5-16 measure the deformation of segments OA, AB, and the base rotation due to slippage and extension of longitudinal bars. All the specimens in the database had sufficient anchorage of longitudinal bars into the footing. So, no slippage occurs and the base rotation is just due to extension of longitudinal bars. This phenomenon is also called strain penetration in the literature. Note that the bottom pin of these LVDTs lies on the foundation. Eq. 5-31 determines the base rotation of the wall specimen in Figure 5-16.

$$\theta_{Sp} = R - \left(\frac{A_{OA} + A_{AB}}{H_{OB}}\right) \qquad \text{Eq. 5-31}$$

In Eq. 5-31, θ_{SP} is the base rotation due to strain penetration. θ_{SP} can be measured by the side LVDTs. A_{OA} and A_{AB} are the areas under curvature diagrams over segments OA and AB, and H_{OB} is the elevation of the top pins of the side LVDTs. Once the base rotation is determined, the equivalent depth of the nonlinear zone into the foundation is determined according to Eq. 5-32.

$$D_{NZ} = \frac{\theta_{SE}}{\varphi_{max}} \qquad \text{Eq. 5-32}$$

5.6.3 Calculating the yield curvature of wall section

As discussed in 5.6.1, the yield curvature of the wall section must be known to find the plasticized height of the walls. Paulay and Priestley (1992) [25] assumed that the first bar yields at a strain of

0.002, while the fiber with the most compressive strain at the opposite edge of the section has a strain of *0.0005*. Eq. 5-33 turns the initial yield curvature of the section.

$$\varphi'_y = \frac{(\epsilon_y = 0.002) + (\epsilon_{ce} = 0.0005)}{L_w} \qquad \text{Eq. 5-33}$$

Due to distribution of bar over the depth of the section, the effective yield happens at somewhat larger deformation as shown in Eq. 5-16.

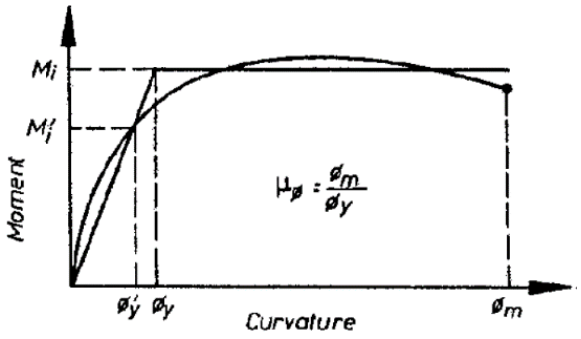

Figure 5-18 Moment curvature diagram of a wall section by Pauley and Priestley

Authors assumed the effective yield to occur at *1.33* of the initial yield and is given by Eq. 5-34.

$$\varphi_y = 1.33\varphi'_y \qquad \text{Eq. 5-34}$$

In a more systematic approach by Kazaz (2013) [28], a moment curvature analysis is done for each specimen. The average axial load during the test was used in the moment curvature analysis. Strain stress equations that fit the actual force deformation of steel bars, and the test day properties of the concrete material were used for this analysis. To find the strain stress relationship of concrete inside the boundary element core, relationships developed by Saatcioglu and Razvi (1992) [29] were used. Figure 5-19 shows the moment curvature diagram for specimen WSH3 tested by Dazio et al. (1990) [42].

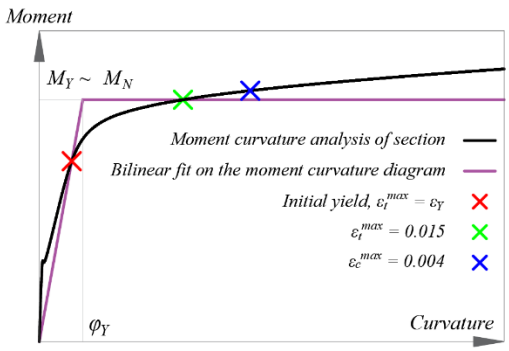

Figure 5-19 Moment curvature diagram of specimen WSH3 tested by Dazio et al.

Three steps on the diagram are to be found.

1. Initial yielding, when the strain of the farthest bar just exceeds the yielding strain.
2. Tensile capacity, when the strain of the bar with maximum tensile strain exceeds *0.015*
3. Compressive capacity, when the strain of the fiber with maximum compressive strain exceeds *0.004*

The section reaches its capacity at load step 2, and 3, whichever occurs first. Once the initial yield point and the capacity point are found, the bilinear curve fitting the moment curvature diagram can be established and the yield curvature of the section is found according to Figure 5-19.

5.6.4 The load step to calculate the plastic hinge height at

As discussed before, the accumulation of the plastic deformations over the plasticized height takes place at loads beyond the yielding deformation, Δ_Y. Analyses by Dazio et al. (2009) [42] show that the height of plastic hinge decreases as the lateral displacement of wall increases. Figure 5-20 shows this trend on specimens tested by Dazio et al.

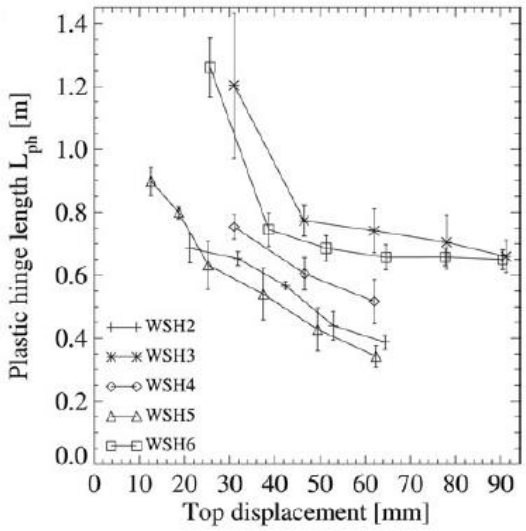

Figure 5-20 Plastic hinge length versus top drift of specimens tested by Dazio et al. (2009)

For the purpose of this work, the height of plastic hinge will be calculated at load steps where the specimen retains its maximum strength, but strength loss is about to initiate. Such a load step corresponds to point *C* on the backbone curve shown in Figure 5-21.

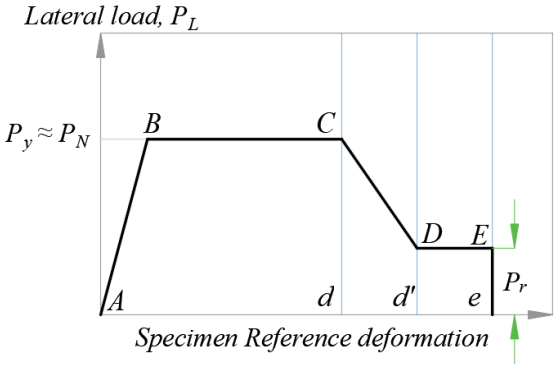

Figure 5-21 Backbone of a tested wall specimen

Here are two remarks regarding the selected load steps to calculate the height of plastic hinge at:

- The loading protocol for the tests include multiple cycles of same amplitude. In many cases, the specimen starts losing strength at the second or third cycle of a load amplitude, while the first cycle has been completed without strength loss. Such amplitudes are considered within the strength loss branch (Segment *CD* of Figure 5-21), and the nonlinear

height was calculated at the peak of cycles with one level smaller amplitude. The load steps at which the plasticized zone is calculated are shown in 7.4 for each specimen.

- The curvature distribution is calculated at the peak of each cycle. For load amplitudes with multiple cycles, the average of curvature distributions is used. For specimens with symmetric cross sections, the average is taken for both the positive, and the negative peak. For specimens with unsymmetric cross section, positive and negative directions were regarded as different data points.

5.6.5 Analyses results, height of the nonlinear zone

Table 5-3 presents the measured height of the nonlinear zone above the footing and the measured base rotation as an equivalent depth of nonlinear zone into the footing.

Table 5-3 Measured height and depth of the nonlinear zone for tests in the database

Specimen	L_w	H_e	$P_u/A_g f'_c$	H_{NZ}	D_{NZ}
	in	*in*	%	*in*	*in*
T1 RW-A20-P10-S38	*48*	*96*	*7.30*	*42.14*	*3.448*
T2 RW-A20-P10-S63	*48*	*96*	*7.30*	*40.12*	*3.455*
T3 RW-A15-P10-S51	*48*	*72*	*7.70*	*42.65*	*2.483*
T4 RW-A15-P10-S78	*48*	*72*	*6.40*	*34.44*	*4.406*
T5 RW-A15-P25-S64	*48*	*72*	*1.60*	*33.77*	*3.285*
WP 1 Positive dir.	*90*	*331*	*9.64*	*66.25*	*2.304*
WP 1 Negative dir.	*90*	*331*	*9.64*	*82.84*	*7.315*
WP 2 Positive dir.	*90*	*330*	*8.36*	*81.38*	*6.033*
WP 2 Negative dir.	*90*	*330*	*8.36*	*71.56*	*5.304*
WP 3 Positive dir.	*90*	*330*	*8.14*	*77.81*	*10.77*
WP 3 Negative dir.	*90*	*330*	*8.14*	*72.75*	*4.827*
WP 4 Positive dir.	*90*	*541*	*6.37*	*71.17*	*3.988*
WP 4 Negative dir.	*90*	*541*	*6.37*	*75.56*	*7.885*
WP 5 Positive dir.	*90*	*321*	*8.03*	*92.72*	*3.098*
WP 5 Negative dir.	*90*	*321*	*6.42*	*92.28*	*7.700*
WP 6 Positive dir.	*90*	*321*	*7.45*	*79.71*	*7.127*
WP 6 Negative dir.	*90*	*321*	*7.45*	*66.46*	*2.246*
WP 7 Positive dir.	*90*	*321*	*5.29*	*85.61*	*5.822*
WP 7 Negative dir.	*90*	*321*	*5.29*	*80.69*	*5.234*
WSH2	*78.7*	*178.0*	*5.20*	*40.11*	*1.045*
WSH3	*78.7*	*178.0*	*5.33*	*52.31*	*1.507*
WSH4	*78.7*	*178.0*	*5.18*	*41.34*	*0.989*
WSH5	*78.7*	*178.0*	*12.3*	*32.15*	*0.829*
WSH6	*78.7*	*179.5*	*10.3*	*45.48*	*1.983*

The equations that are mostly used in practice follow the general form of Eq. 5-10 proposed by Berry and Eberhard. This general form indicates that the height of the nonlinear zone increases with increase in effective height and the length of the wall. Figure 5-22 and Figure 5-23 show the same rend for the experiments in the database. In these figures the red marks indicate the nonlinear height measured for each specimen in the database and the blue line is the linear regression over the datapoints.

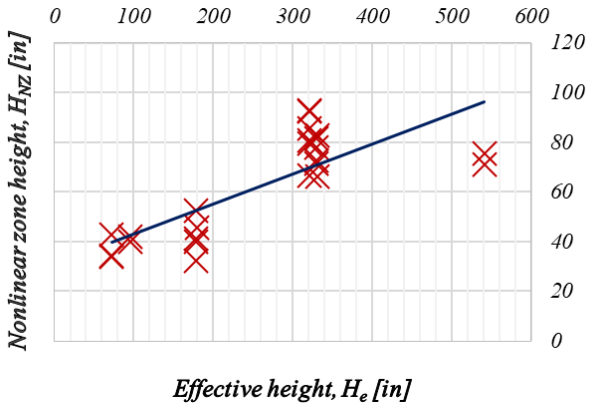

Figure 5-22 Height of the nonlinear zone vs effective height for the experiments in the database

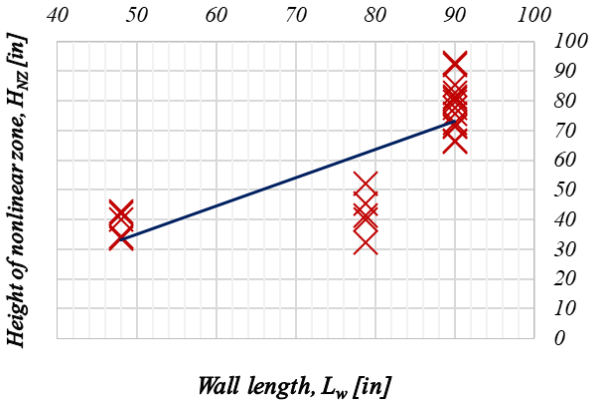

Figure 5-23 Height of the nonlinear zone vs wall length for the experiments in the database

A linear regression is conducted to develop an equation for the nonlinear height in terms of the effective height and the length of the structural wall. Eq. 5-35 shows the proposed equation and the coefficient of determination, R^2.

$$H_{NZ}[in] = 0.51L_w + 0.067H_e + 4.8, \qquad R^2 = 0.666 \qquad \text{Eq. 5-35}$$

Note that the there is a nonzero residual. Eq. 5-36 shows the equation obtained by linear regression, with the assumption that the residual is zero.

$$H_{NZ} = 0.59L_w + 0.061H_e, \qquad R^2 = 0.665 \qquad \text{Eq. 5-36}$$

Table 5-4 summarizes some equations used by other researchers to estimate height of plasticized zone, and the calculated R^2 based on the measured plasticized zone of specimens in the data base.

Table 5-4 Proposed equation by authors for calculation of nonlinear height of RC walls

Author	Equation	R^2
Eurocode 8 (2005)	$H_{NZ} = 0.4L_w + 1/15\,H_e$	*0.201*
Paulay and Priestley (1996)	$H_{NZ} = 0.16H_e$	*-0.514*
Paulay and Priestley (1992)	$H_{NZ} = 0.4L_w + 0.14H_e$	*0.425*
Bohl and Adebar (2011)	$H_{NZ} = 0.4L_w + 0.1H_e\left(1 - 1.5\frac{P}{f'_c A_g}\right)$	*0.350*
Kazaz (2013)	$H_{NZ} = 0.333L_w + 0.167H_e$	*0.237*
Segura and Wallace (2017)	$H_{NZ} = 0.5L_w$	*-0.0604*

5.6.6 Analysis results, depth of the nonlinear zone

Table 5-3 shows the measured depth of the nonlinear zone for the tests in the database. This depth specifies the base rotation due to strain penetration as an equivalent depth of the nonlinear zone with the maximum curvature, φ_u. Paulay and Priestley (1992) estimate this depth with Eq. 5-37.

$$D_{NZ} = \xi d_b f_y = 0.15 d_b f_y \qquad \text{Eq. 5-37}$$

The expression in Eq. 5-37 is obtained based on two assumptions.

1. The depth of the nonlinear zone, and the depth of strain penetration into the foundation are in direct proportion.
2. The cohesion stress between concrete and reinforcing bars is constant.

If assumptions 1 and 2 are true, the depth of strain penetration into the foundation, L_{SP}, for a single longitudinal bar can be calculated by Eq. 5-38.

$$L_{SP} = \frac{A_b F_y}{c P_b} = \frac{\frac{\pi}{4} {d_b}^2 F_y}{c \pi d_b} = \frac{d_b F_y}{4c} \qquad \text{Eq. 5-38}$$

In Eq. 5-38, c is the cohesion stress between concrete and steel bara. The measured depth of nonlinear zone into the footing (According to 5.6.2) versus $d_b F_y$ is plotted in Figure 5-24 for the tests in the database. For some walls, bars with different size and yield stress are used in the boundary element. In this case, parameter $P = 4 \sum A_b^i F_y^i / \sum \pi d_b^i$ would be equivalent to $d_b F_y$.

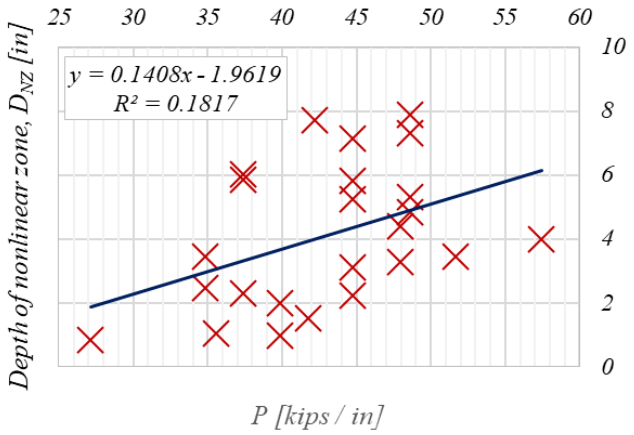

Figure 5-24 Depth of nonlinear zone versus parameter P

Although the measured depth of nonlinear zone shows the same trend that Eq. 5-37 suggests, but the coefficient of determination is very low. This scatter is associated with the low number of tests, and the inaccuracy in measuring the associated deformations. Parameter ξ in Eq. 5-37 is calculated based on the measurements of tests in the database and compared with the proposed value by Paulay and Priestley in Figure 5-25.

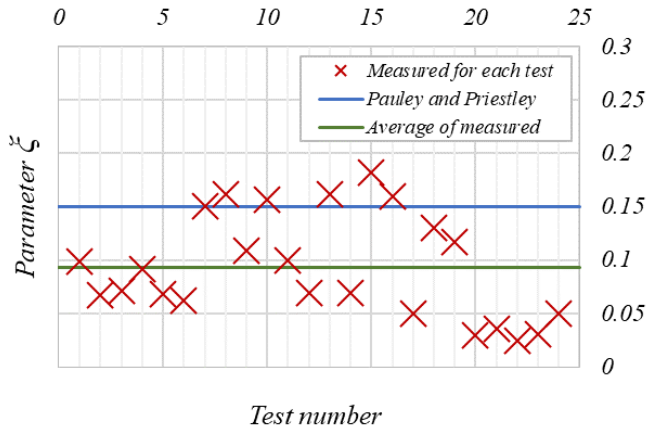

Figure 5-25 Parameter ξ

Eurocode 8 (2005) [53]'s equation to estimate the plastic zone depth, shown in Eq. 5-39, correlates the cohesion stress to the square root of concrete specified strength, $\sqrt{f'_c}$.

$$D_{NZ} = \eta \frac{d_b f_y}{\sqrt{f'_c}} = 9.135 \frac{d_b f_y}{\sqrt{f'_c}}$$ Eq. 5-39

In Eq. 5-39, f_y is in ksi, f'_c is in psi, and the depth of nonlinear zone, D_{NZ}, is turned in inch. Like what I did for Eq. 5-37, the measured depth of the nonlinear zone into the foundation is plotted, this time, against parameter $Q = 4\sum A_b^i F_y^i / \sum f'_c \pi d_b^i$ and the plot is shown in Figure 5-26.

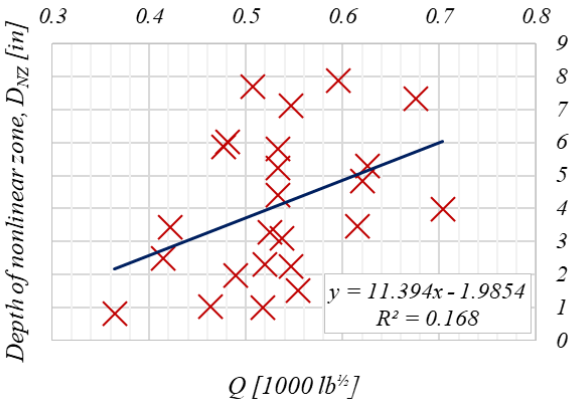

Figure 5-26 Depth of nonlinear zone versus parameter Q

Again, the trend confirms what the equation proposes, but the data scatters a lot. Furthermore, considering the effect of concrete strength in cohesion stress does not improve the coefficient of determination. The measured value of parameter η for each test, the average value, and the recommended value by Eurocode 8 are all compared in Figure 5-27.

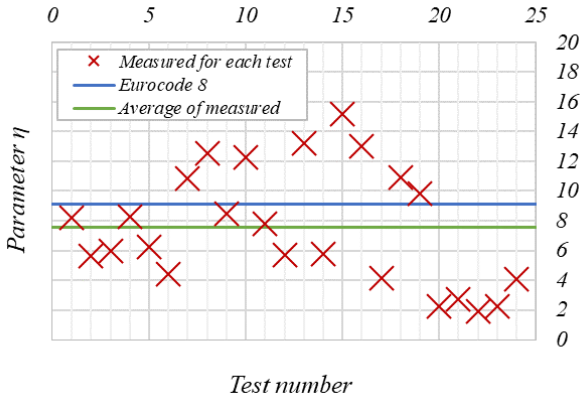

Figure 5-27 Parameter ξ

5.7 Summary of the results

Eq. 5-40 shows two proposed equations for plasticized zone of flexurally-controlled walls, based on analysis of the data of the tests in the data base.

$$H_{PZ} = 0.6L_w + 0.06H_e + 0.09d_{bl}F_y$$

$$H_{PZ} = 0.6L_w + 0.06H_e + 8\frac{d_{bl}F_y}{\sqrt{f'_c}} \qquad \text{Eq. 5-40}$$

The first two terms turn the height of the nonlinear zone, and the third term turns the base rotation an equivalent depth of the nonlinear zone into the footing. The coefficient of determination, R^2, for the first two terms is ~0.665, which seems acceptable. The R^2 factor for the depth of the nonlinear zone is ~0.18. More data may improve the efficiency of the models, but note that these models have been obtained using instruments that measure local deformations of RC specimens, and model with better performance may not be achieved.

Chapter 6 Summary and future work

This dissertation consists of two main studies. The key conclusions of each study are presented in this section.

6.1 Wall model

The wall model developed in this study provides several advantages for applications of Performance-Based design of buildings with structural walls as the lateral force resisting system. The primary goal of the model is to enable control over the load versus deformation response of fiber models of structural walls that can be matched to specified component backbone relations, such as prescribed in ASCE 41 [2]. To accomplish this goal, the strain-stress response of the material used for the fibers of the element cross-section is mapped into a strain-strain-stress space, where the additional dimension provides greater flexibility to accommodate strength deterioration. The element is implemented in OpenSees [4], an open-source computer program for structural and earthquake engineering, and then used in two case studies. One case-study is a static pushover analysis and the other case-study is nonlinear dynamic analysis of a structural wall designed according to the latest building code. Computer implementation and the case studies show the reliability and effectiveness of the element for both static and dynamic analyses.

More refinements are presented in Chapter 4 that enable the computation of demand to capacity ratios of deformation parameters in real time within each load step. The variables that determine the backbone curve of the element (e.g., deformation at strength loss), have been shown to vary with shear stress, axial load, and depth of the compression zone, which vary in time over the analysis. Pre-assigning these variables based on an estimate of maximum probable values occurring simultaneously results in underestimating the wall deformation capacity and a

conservative performance assessment for the wall and the building. This is particularly true for coupled-wall systems, or dual systems, where the variables impacting deformation capacity may vary significantly over time (e.g., for the tension versus compression piers of a coupled wall. In these cases, the proposed model provides substantial benefits versus current approaches.).

6.1.1 Future work

Some aspects discussed in the formulation, such as use of smooth hysteretic performance, were not implemented in the current model. Thus, the strain-stress response of the fibers in case studies of sections 3.13 and 3.14 show piece-wise linear response and more work is required to implement the transitions relations into the model.

Table 4-2 specifies the residual strength of the wall once deformation parameter d' is exceeded. The elements residual strength depends on the residual stress of the material, and the depth of section over which the material is damaged. Section 3.7 describes how the material relation parameters are assigned once strength degradation initiates. An approach to enable a prescribed residual stress (e.g., as given in ASCE 41 tables) to be targeted was not developed. Although this feature would be helpful, it is not essential to produce useful and improved results with the model.

The wall element developed in this study captures the strength degradation response when one element over the plastic hinge is used. In analysis of a 3D structure, as is required for a code compliant Performance-Based design, more than one element over the plan might be required within the plastic hinge region. An example of this case is shown in Figure 6-1. This wall is modeled with three elements within four nodes over the plastic hinge. The study by Abdullah and Wallace (2019) [47], determines the backbone curve for the combination of the three elements with the plan view shown in Figure 6-1. To address this situation, additional work is needed.

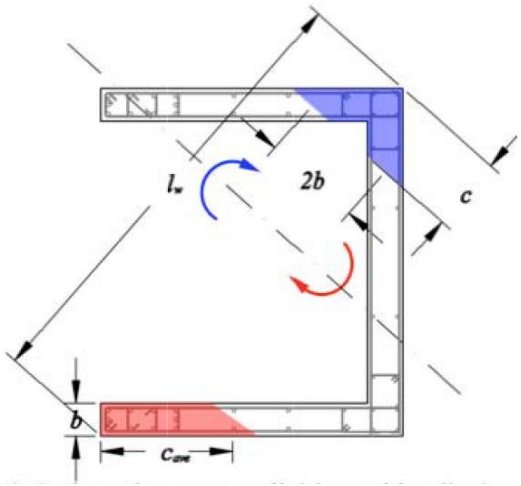

Figure 6-1 Plan view of a C-shaped wall with bi-directional loading

6.2 Height of nonlinear zone

Chapter 5 includes a study to evaluate current models used to estimate the plasticized zone of flexure-controlled structural walls. This parameter is used in many studies for different purposes, including calculation of plastic hinge rotation from drift. A database of 17 tested specimens is assembled. The specimens selected were well-instrumented, such that the extent of nonlinearity can be measured over the wall height. Analyses of 24 datapoints from 17 testes recommended Eq. 6-1 to estimate the plastic hinge height of flexure-controlled walls.

$$H_{PZ} = 0.6L_w + 0.06H_e + 0.09d_{bl}F_y$$

$$H_{PZ} = 0.6L_w + 0.06H_e + 8\frac{d_{bl}F_y}{\sqrt{f'_c}} \quad \text{Eq. 6-1}$$

6.2.1 Future work

Although hundreds of structural walls have been tested and studied (e.g., see Abduallah and Wallace (2018) [50]), only a relatively few have sufficient instrumentation to be used in this study. More data are required to improve the reliability of the models and study the impact of other parameters, including the axial load as some researchers (e.g., Bohl (2006) [48] and Kazaz (2013)

[28]) have reported that axial load has considerable impact on plastic hinge length of structural walls. This becomes especially important for coupled walls, where there the axial load varies over a wide range, from net tensile load to large net compressive load. The database in this study has a relatively small number of tests and the range of axial loads is limited. Another important subject that can be part of a future work is calibrating deformation parameters of a backbone curve in real time with a varying plastic hinge length.

Chapter 7 Appendix

7.1 Calculation of deformation parameters in a typical load step

Calculation of backbone curve parameters for the bottom element of the twelve-story coupled wall system shown below, within a typical load step (Load step 2,361) is presented in this chapter. The wall is loaded with a displacement – controlled scheme and a distribution of lateral loads shown in the figure below.

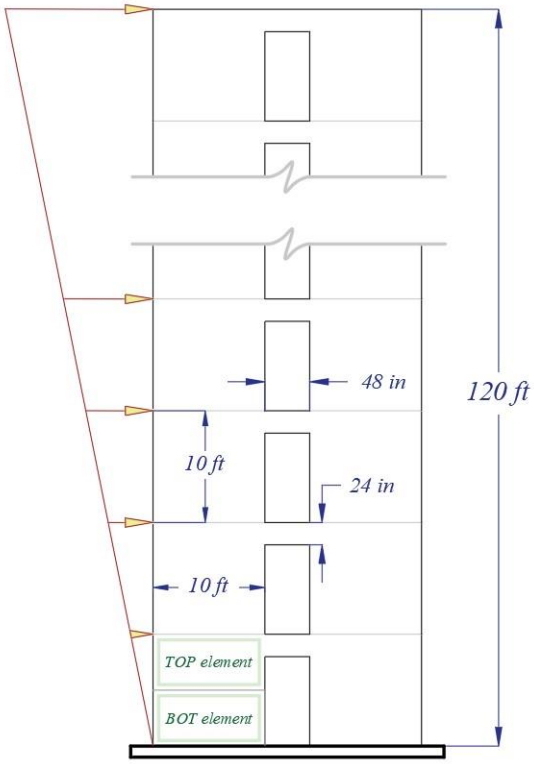

The wall cross section for the left side pier is shown below. The wall piers are symmetric with respect to the coupling beams centerline. The section is discretized into fibers to model the walls using MVL elements. Two elements are used in each story.

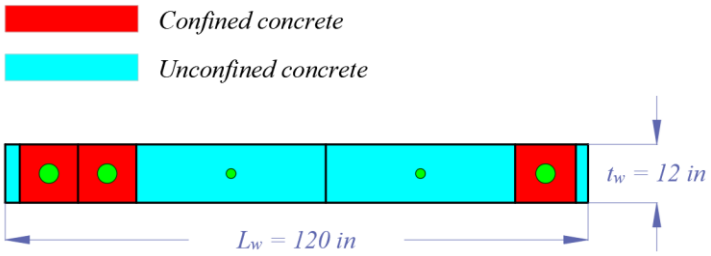

The thickness, with, reinforcement ratio, concrete area, steel area and local coordinate of the fibers of the wall cross section, from left to right, is shown in the table below.

Fiber No.	t_f	w_f	ρ	A_C	A_S	x_F
	in	in		in^2	in^2	in
1	16	3	0.0423	2.0304	45.9696	-58.5
2	16	12	0.0423	8.1216	183.878	-51
3	16	12	0.0423	8.1216	183.878	-39
4	16	39	0.0122	7.6128	616.387	-13.5
5	16	39	0.0122	7.6128	616.387	25.5
6	16	12.5	0.0423	8.46	191.54	51.25
7	16	2.5	0.0423	1.692	38.308	58.75

The history of controlled roof drift is shown in the diagram below.

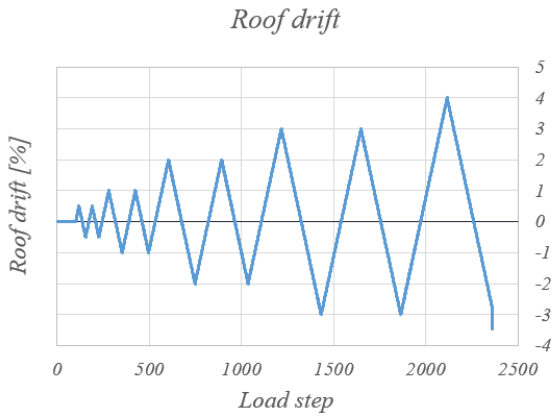

The element nodal forces for a typical wall element are shown in the figure below.

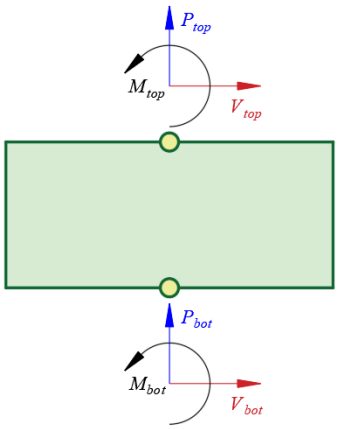

The forces of the bottom element of the left pier at the last converged load step, and at a trial state to solve for the current load step, are shown in the table below.

Load Step	V_{bot}	P_{bot}	M_{bot}	V_{top}	P_{top}	M_{top}
	kips	*Kips*	*k - ft*	*kips*	*kips*	*k – ft*
2,360, C	*493.318*	*4800.1*	*-20564.9*	*-493.318*	*-4800.1*	*18098.3*
2,361, T	*542.732*	*5177.35*	*-23059.9*	*-542.732*	*-5177.35*	*20346.3*

The normalized shear stress of the element, at the end of the last converged load step, ${v_u}^C$ and at a trial deformation to solve for the current load step, ${v_u}^T$ is:

$${v_u}^C = \frac{\omega_v V_u}{t_w L_w \sqrt{f'_c}} = \frac{493.318 \times 1{,}000}{12 \times 120 \times \sqrt{6{,}000}} = 4.423, \qquad {v_u}^T = \frac{542.732 \times 1{,}000}{12 \times 120 \times \sqrt{6{,}000}} = 4.866$$

The element nodal displacements for a typical wall element are shown in the figure below.

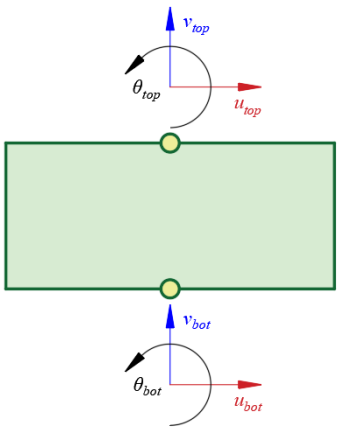

The nodal displacements of the bottom element of the left pier, at the last converged load step (Load step 2,360), and at a trial deformation to solve for the current load step are shown in the table below.

Load Step	u_{bot}	v_{bot}	θ_{bot}	u_{top}	v_{top}	θ_{top}
	in	*in*		*in*	*In*	
2,360, C	*0*	*0*	*0*	*-0.58159*	*0.15375*	*0.01535*
2,361, T	*0*	*0*	*0*	*-0.75731*	*0.22421*	*0.020136*

The deformation vector of Figure 4-18, from the last converged state to the trial deformation at the current load step, for the element is shown below.

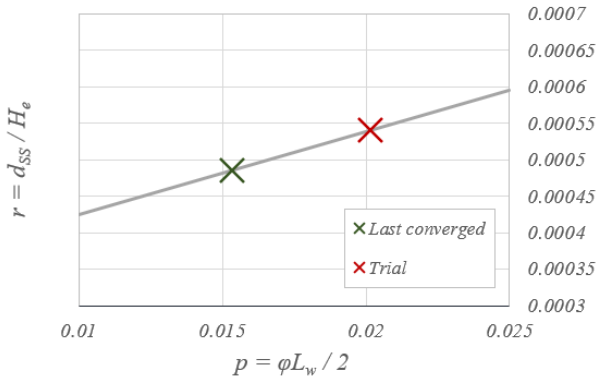

Parameters *C*, and *D* of Eq. 4-26 are

$C = 0.0054071, \quad D = 0.00037094$

Assuming the shear force deformation has an elastic linear response, the stiffness assigned to the shear spring of the element is

$$K_{SS} = \frac{G_{eff} A_{eff}}{H_e} = \frac{0.5 \times \frac{57 \times \sqrt{6{,}000}}{2 \times (1 + 0.2)} \times \frac{5}{6} \times 12 \times 120}{60} = 18{,}397$$

The shear stress of Table 4-2, in terms of curvature comes from Eq. 4-28 and is determined as follows.

$$v_u(\varphi) = \frac{\omega_v V_{M_{ult}}}{A_{cv}\sqrt{f'_c}} = \frac{K_{SS} H_e \left(C\left[\varphi \frac{L_w}{2}\right] + D\right)}{A_{cv}\sqrt{f'_c}} = \frac{18{,}397 \times 60 \times (0.0054071[\varphi \times 60] + 0.00037094)}{12 \times 120 \times \frac{5}{6} \times \sqrt{6{,}000}}$$

Simplified here.

$$v_u(\varphi) = 3{,}853\varphi + 4.405$$

The computation of the compression zone depth requires knowing zero – stress – strain based on the material properties at the converged load step. Figure below shows the strain stress history of the steel material in fiber 1.

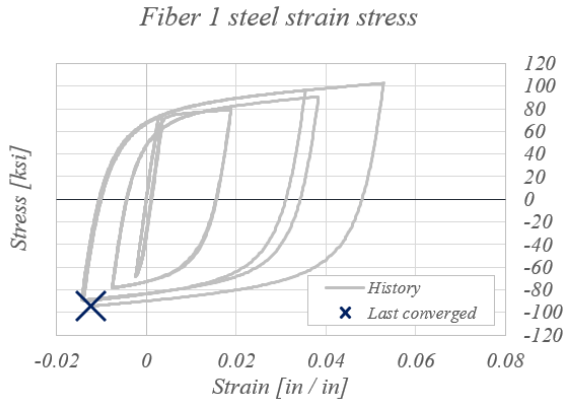

The zero – stress – strain is calculated based on the properties of the material at the last converged step. Note that the stress is compressive and the material needs to be loaded in tensile loading to turn back to zero stress. The strain stress equation for this tensile load path is governed by MP equations.

$$\sigma^* = b\varepsilon^* + \frac{(1-b)\varepsilon^*}{(1+\varepsilon^{*R})^{\frac{1}{R}}}, \qquad \varepsilon^* = \frac{\varepsilon - \varepsilon_r}{\varepsilon_r - \varepsilon_0}, \qquad \sigma^* = \frac{\sigma - \sigma_r}{\sigma_r - \sigma_0}$$

σ is the material stress and ε, is the material strain. Other parameters are shown in the table below, based on the material properties at the last converged load step.

ε_0	ε_R	σ_0	σ_R	R
		ksi	*ksi*	*in*
-0.0059827	*-0.012399*	*91.6483*	*-94.4342*	*1.6146*

To solve for $\sigma = 0$, Newton's approach is used within a newly added member function to the material object. An initial guess for the zero-stress strain is:

$$\varepsilon_{\sigma=0} = \varepsilon^C - \frac{\sigma^C}{E_0} = -0.012399 - \frac{-94.43}{29{,}000} = -0.009143$$

Iterations that lead to finding the exact strain corresponding to zero stress is shown in the table below.

Iterations	ε	ε^*	σ^*	σ	$T = \frac{\partial \sigma^*}{\partial \varepsilon^*}$
1	*-0.009143*	*0.5074859*	*0.4252614*	*-15.30054*	*-0.082224*
2	*-0.008306*	*0.6379095*	*0.5009503*	*-1.216157*	*-0.006536*
Iterations	ε	ε^*	σ^*	σ	$T = \frac{\partial \sigma^*}{\partial \varepsilon^*}$
3	*-0.008227*	*0.6501836*	*0.5074335*	*-0.00974*	*-5.23E-05*
4	*-0.008227*	*0.6502835*	*0.5074859*	*-6.39E-07*	*-3.43E-09*

The zero-stress strain, $\varepsilon^{\sigma=0}$, and the load path from converged state to the zero-stress point is shown in the figure below.

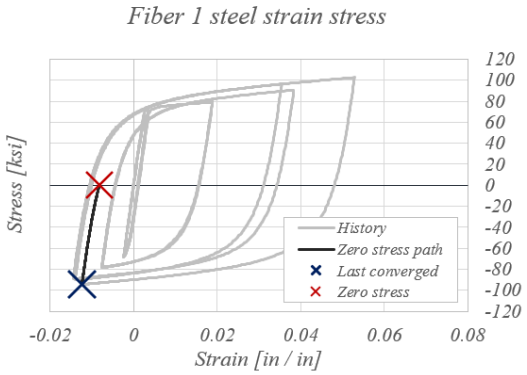

Same calculations are done for steel material of other fibers.

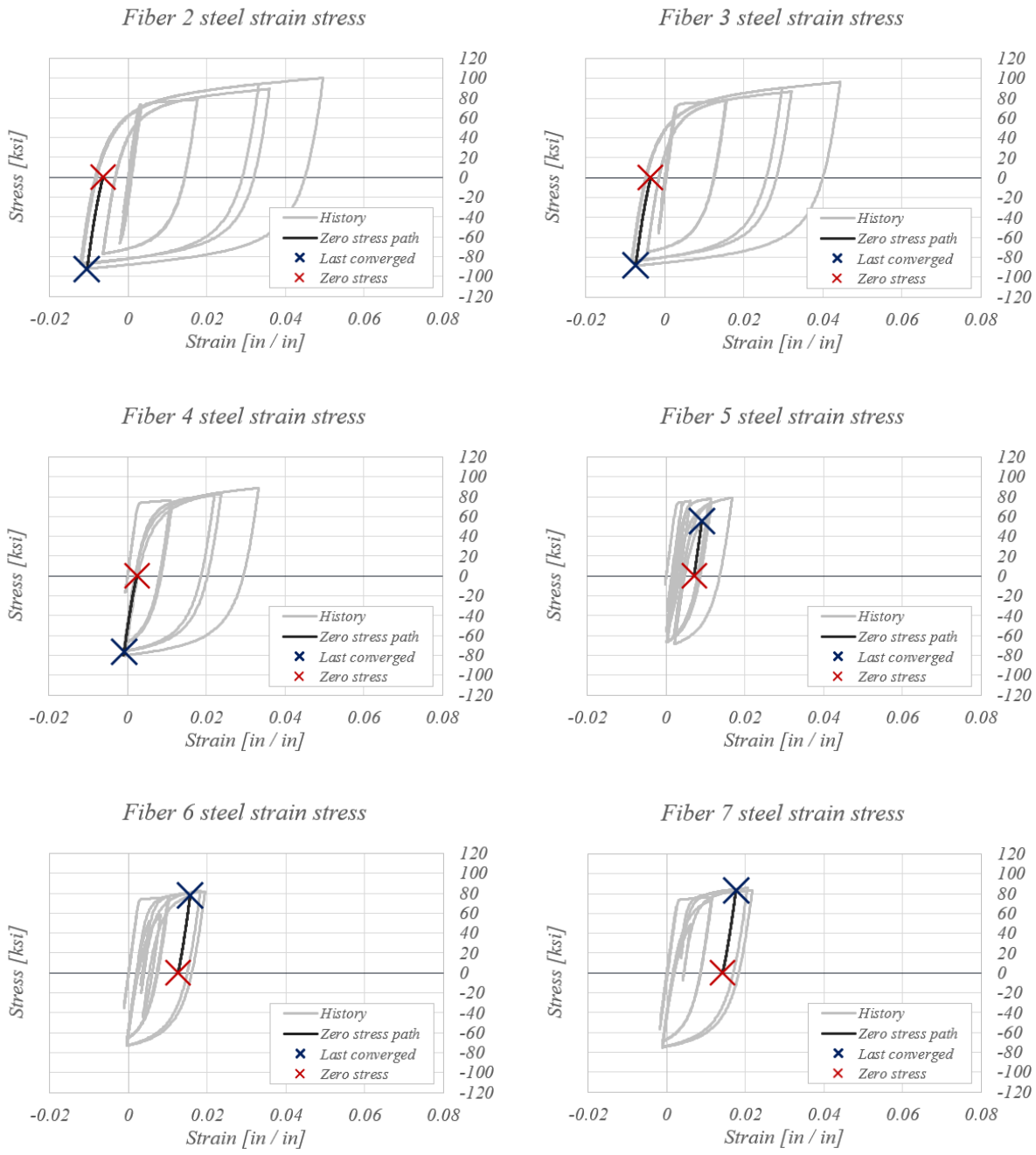

The profile of zeros-stress strain (Figure 4-15) over the section at the last converged load step is shown in figure below.

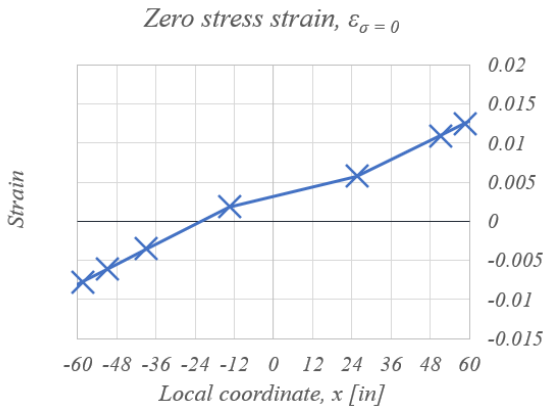

Each segment of the profile is governed by an $\varepsilon = mx + n$ with coefficients, from left to right, in the table below.

Segment	*m*	*n*
1	*0.00021820*	*0.00498794*
2	*0.00021754*	*0.00495429*
3	*0.00021196*	*0.00473659*
4	*0.00010053*	*0.00323222*
5	*0.00019915*	*0.00071722*
6	*0.00020612*	*0.00036004*

The strain profile of the element, corresponding to the last converged load step, and to a trial deformation to solve for the current load step, is shown in figure below. The location of the hinge in Figure 4-16 is $x_H = -13.12\ in,\ \varepsilon_H = -0.001228$

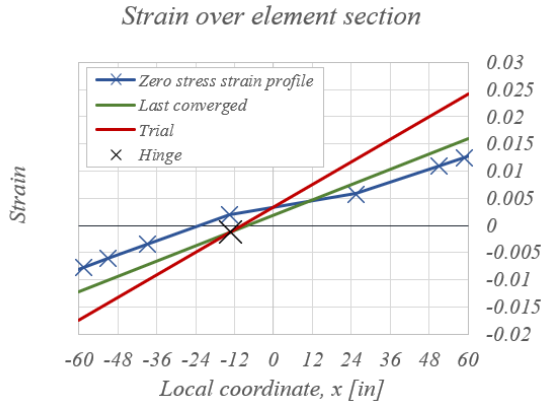

The strain profiles cross the fourth segment. The equation of the compression zone depth using Eq. 4-22 is shown below.

$$C_E(\varphi) = x_{CZ}^k - \left(-\frac{L_w}{2}\right) = \frac{-13.12\varphi + 0.003232 + 0.001228}{\varphi - 0.0001005} + 60$$

The compression zone parameter λ in terms of curvature is shown below

$$\lambda(\varphi) = \frac{C_E L_w}{b^2} = \frac{-10.93\varphi + 0.003717}{\varphi - 0.0001005} + 50$$

Knowing the compression zone parameter, λ, and the shear stress parameter, v_u, The capacity for deformation parameter d is obtained by double-interpolating through Table 4-2.

$$C_d(\varphi) = \left(0.032 + \frac{0.026 - 0.032}{6 - 4}(v_u(\varphi) - 4)\right) +$$

$$\frac{\left(0.018 + \frac{0.014 - 0.018}{6 - 4}(v_u(\varphi) - 4)\right) - \left(0.032 + \frac{0.026 - 0.032}{6 - 4}(v_u(\varphi) - 4)\right)}{70 - 10}(\lambda(\varphi) - 10)$$

$$C_d(\varphi) = \left(0.032 - 0.003(v_u(\varphi) - 4)\right) + \frac{0.001(v_u(\varphi) - 4) - 0.014}{60}(\lambda(\varphi) - 10)$$

$$C_d(\varphi) = \left(0.044 - 0.003v_u(\varphi)\right) + (0.001v_u(\varphi) - 0.018)\frac{\lambda(\varphi) - 10}{60}$$

The demand of plastic hinge rotation in terms of curvature is

$$D_d(\varphi) = \varphi H_e$$

$$C_d(\varphi) = D_d(\varphi)$$

$$F(\varphi) = \left(0.044 - 0.003v_u(\varphi)\right) + (0.001v_u(\varphi) - 0.018)\frac{\lambda(\varphi) - 10}{60} - \varphi H_e = 0$$

Newton's approach is used to solve the nonlinear equation.

$$F'(\varphi) = -0.003v'_u(\varphi) + 0.001v'_u(\varphi)\frac{\lambda(\varphi) - 10}{60} + (0.001v_u(\varphi) - 0.018)\frac{\lambda'(\varphi)}{60} - H_e$$

$$\varphi_{N+1} = \varphi_N - \frac{F(\varphi_N)}{F'(\varphi_N)}$$

All functions $v_u(\varphi)$, $v'_u(\varphi)$, $\lambda(\varphi)$, and $\lambda'(\varphi)$ have been computed before. The table of iterations to solve for element curvature φ, at deformation parameter d, is shown in table below. The initial guess is obtained by interpolation. The curvature, φ, and demand to capacity ratio for parameter d, $[D/C]_d$, at the last converged load step, and at a trial deformation to solve for the current load step is shown in the table below.

Load step	φ	$[D/C]_d$
2,360 C	*0.000234220*	*0.7869*
2,361 T	*0.000347763*	*1.118*

An initial guess, φ_1, to solve for $[D/C]_d = 1$ is calculated here using the table.

$$\varphi_1 = 0.00023422 + \frac{0.000347763 - 0.000234220}{1.118 - 0.7869}(1.118 - 1.0) = 0.0003073$$

Table below shows the iterations to solve for $[D/C]_d = 1$.

φ	v_u	v_u'	λ	λ'	F	F'
1 / in						
0.00030730	*5.589*	*3853*	*51.73*	*-61,223*	*1.646E-02*	*-56.2143*
φ	v_u	v_u'	λ	λ'	F	F'
0.00060014	*6.717*	*3853*	*44.31*	*-10,487*	*-1.861E-02*	*-67.3829*
0.00032395	*5.653*	*3853*	*50.78*	*-52,438*	*-7.881E-04*	*-58.1482*
0.00031039	*5.601*	*3853*	*51.54*	*-59,430*	*-1.010E-05*	*-56.6091*
0.00031022	*5.600*	*3853*	*51.55*	*-59,531*	*-1.988E-09*	*-56.5868*
0.00031022	*5.600*	*3853*	*51.55*	*-59,531*	*-7.633E-17*	*-56.5868*
0.00031022	*5.600*	*3853*	*51.55*	*-59,531*	*0.000E+00*	*-56.5868*

Once deformation parameter d is determined, other parameters (d', c, and e) would be computed based on compression zone parameter λ, and axial load ratio p_u at element rotation of d.

7.2 Transition equations used in strain stress curves

Figure below shows the strain stress curve of a typical steel material. To provide a transition from segment 1, governed by the Menegotto Pinto equation, to segment 2, the stress degradation curve, the coordinates of the start of the transition assumed to be at point 1, P_1, must be determined. In the sample problem below, the start of the transition is assumed to be at $0.8 \times D$.

$$x_{P_1} = 0.8 \times D, \qquad y_{P_1} = b\left[\frac{x_{P_1}}{\varepsilon_y}\right] + \frac{(1-b)\left[\frac{x_{P_1}}{\varepsilon_y}\right]}{\left(1+\left[\frac{x_{P_1}}{\varepsilon_y}\right]^R\right)^{\frac{1}{R}}}$$

The tangent at point 1, T_{P_1}, is also determined.

$$T_{P_1} = \frac{y_{P_1}}{x_{P_1}} - \frac{\left[\frac{y_{P_1}}{x_{P_1}} - bE_s\right]}{1+\frac{1}{\left[\frac{x_{P_1}}{\varepsilon_y}\right]^R}}$$

In equations above, b is the strain-hardening ratio and E_s is the initial stiffness of the material.

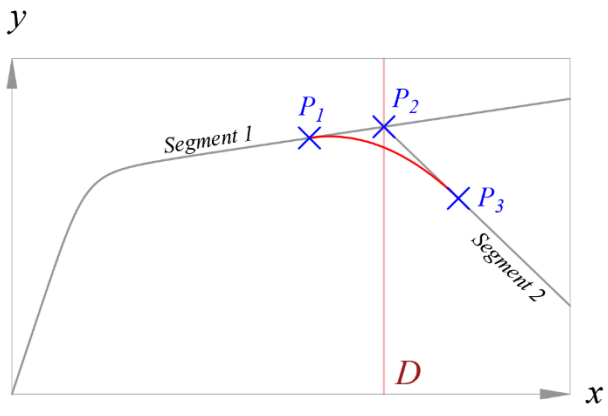

Segment 2 of the curve is governed by the coordinates of point 2, P_2, and a constant tangent, T.

$$y_D = T(x - x_{P_2}) + y_{P_2}, \qquad x_{P_2} = D$$

The intersection of the first segment, and the second segment happens at point 2, P_2. Assuming the transition starts at point 1, P_1, and the tangent varies uniformly till the landing point, equation of the transition, (x_T, y_T), is governed by a polynomial shown below.

$$y_T = a(x - x_{P_1})^2 + T_{P_1}(x - x_{P_1}) + y_{P_1}$$

The coordinates of the landing point, P_3, is obtained by setting equal, the tangent of the transition and descending segment.

$$T_D = T_T, \qquad 2a(x - x_{P_1}) + T_{P_1} = T, \qquad a = \frac{T - T_{P_1}}{2(x - x_{P_1})}$$

The x, and y coordinate of the landing point, P_3, is obtained by setting equal, the ordinate of the transition and descending segment.

$$y_D = y_T, \qquad a(x_{P_3} - x_{P_1})^2 + T_{P_1}(x_{P_3} - x_{P_1}) + y_{P_1} = T(x_{P_3} - x_{P_2}) + y_{P_2}$$

7.3 Analysis and design of the structural walls in case study 3.13

The seismic properties of the building site are assumed as follows.

$$S_s = 2.136, \qquad S_1 = 0.718$$

The Site class is assumed to be C. From table 11.4-1 and 11.4-2, and knowing that the site class is C, and $S_s \geq 1.25$, $S_1 \geq 0.5$, we will find F_a and F_v.

$$F_a = 1.0, \qquad F_a = 1.3$$

ASCE 7 Equation 11.4-1 and Equation 11.4-2 turn S_{MS} and S_{M1}.

$$S_{MS} = F_a S_S = 1.0 \times 2.136 = 2.136$$

$$S_{M1} = F_a S_1 = 1.3 \times 0.718 = 0.9334$$

ASCE 7 Equation 11.4-3 and Equation 11.4-4 turn S_{DS} and S_{D1}.

$$S_{DS} = \frac{2}{3} S_{MS} = \frac{2}{3} \times 2.136 = 1.424$$

$$S_{D1} = \frac{2}{3} S_{M1} = \frac{2}{3} \times 0.9334 = 0.6223$$

$$T_0 = 0.2 \frac{S_{D1}}{S_{DS}} = 0.2 \times \frac{0.6223}{1.424} = 0.0874, \qquad T_s = \frac{S_{D1}}{S_{DS}} = \frac{0.6223}{1.424} = 0.437$$

The seismic response spectra are calculated and shown in Figure 7-1 and Figure 7-2.

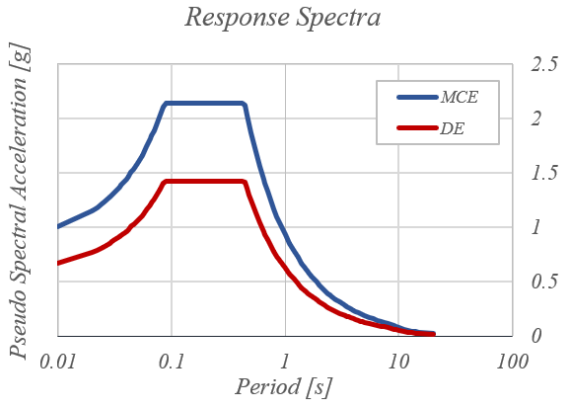

Figure 7-1 Response spectrum (Acceleration) of the building site

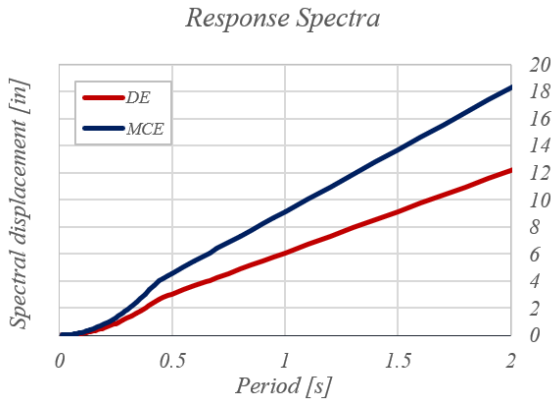

Figure 7-2 Response spectrum (Displacement) of the building site

The preliminary design starts with satisfying the drift limit. The fundamental period for the wall is estimated assuming uniform distributed mass over the height of the wall. The mass of each floor is calculated first. Referring to the floor plan of Figure 3-37, and assuming an 8 in. slab and a 25 psf super-imposed dead load, the total dead load of the floor is:

$$\omega_D = 150 \times \frac{8}{12} + 25 = 125\ psf$$

Floors are all square and 131 ft. by 131 ft.

$$W_f = 131 \times 131 \times 0.125 = 2{,}145\ kips, \qquad m_f = \frac{W_f}{g} = \frac{2{,}145}{32.2 \times 12} = 5.551\ \frac{kips - s^2}{in}$$

Two walls resist the seismic load of the building. The tributary mass of each floor for one wall is

$$m_w = \frac{5.551}{2} = 2.776\ \frac{kips - s^2}{in}$$

Assuming the mass is uniform over the wall height, the mass per unit height of the wall is

$$\bar{m} = \frac{m_w}{H_s} = \frac{2.776}{144} = 0.019278\ \frac{kips - s^2}{in^2}$$

Assuming the length of the wall is 12 times the thickness as an initial guess. The effective flexural stiffness factor for the wall is 0.5.

$$L_w = 12t_w, \qquad EI_z = 0.5 \times \frac{1}{12} t_w {L_w}^3 = 72{t_w}^4$$

The modal periods for the wall can be estimated by

$$\omega_n = (aH)^2 \sqrt{\frac{EI}{\bar{m}H^4}}$$

Where H is the total height of the building, and $\bar{m}$ is the uniform mass over the wall height. ACI 318-14 section 19.2.2.1(b) estimates concrete's modulus of elasticity as follows.

$E_c = 57\sqrt{f'_c} = 57 \times \sqrt{6{,}000} = 4{,}415\ ksi$

For the first mode period $aH_1 = 1.875$. The total height of the building is:

$H = 10 \times 12 \times 12 = 1440\ in$

After substituting for all the parameters, the first mode frequency for the wall is:

$$\omega_1 = (aH)^2 \sqrt{\frac{EI}{\bar{m}H^4}} = 7.216 \times 10^{-3} {t_w}^2$$

$$T_1 = \frac{2\pi}{\omega_1} = \frac{2\pi}{7.216 \times 10^{-3} {t_w}^2} = \frac{870.8}{{t_w}^2}$$

Assuming the maximum story drift ratio for the wall is 2%, the average drift ratio over the entire height is approximately:

$$\frac{\delta_{roof}}{H_w} = \frac{3}{4} \times 2 = 1.5\ \%, \qquad \delta_{roof} = 0.015 \times 10 \times 144 = 21.6\ in$$

Knowing the displacement at roof, the lateral displacement at the effective height of first mode for the wall is approximately:

$$\delta_{H_{eff}} = \frac{\delta_{roof}}{1.5} = \frac{21.6}{1.5} = 14.4\ in = Sd$$

Knowing the response spectrum of the site, the period that turns this spectral displacement is estimated.

$$S_d = 14.4\ in \xrightarrow{yields} T = 2.36\ sec$$

So, if the building's period is almost equal to 2.36, it will meet the drift limit.

$$2.36 = \frac{870.8}{{t_w}^2} \xrightarrow{yields} t_w = \sqrt{\frac{870.8}{2.36}} \approx 20.0\ in, \qquad L_w = 20\ ft$$

It was discovered later that a larger section is required to provide enough strength. The final design is a section with the length $L_w = 27\ ft$, and thickness of $t_w = 26\ in.$

Lateral forces for strength design of the wall are calculated using ASCE 7 chapter 12.8, The Equivalent Lateral Force Procedure. The response spectrum of the building and the modal periods of the building have been calculated before.

$T_a = C_t {h_n}^x$

Referring to Table 12.8-2, for a RC bearing walls, the coefficients for calculating the approximate fundamental period are:

$C_t = 0.02, \qquad x = 0.75$

$T_a = 0.02 \times 120^{0.75} = 0.725\ sec$

Table 12.8-1 gives the coefficient for upper limit on approximate period.

$S_{D1} \geq 0.4 \xrightarrow{yields} C_u = 1.4$

$T_u = C_u T_a = 1.4 \times 0.725 = 1.02\ sec$

The first mode period of the building in the direction of the walls is calculated using a modal analysis in MATLAB with walls modeled using elastic beam column elements. An effective stiffness factor of 0.5 is assumed and shear deformation is ignored.

$T_1 = 1.403$

Note that the calculated first mode period is more than the upper limit set by 12.8.2. So, T_u shall be used for calculation of seismic forces. From the response spectrum, the Pseudo Spectral Acceleration, pSa, for the building in the direction of walls is

$$pSa = 0.610\ g, \qquad C_s = \frac{pSa}{\left(\frac{R}{I_e}\right)} = \frac{0.610}{\frac{5}{1.0}} = 0.1226$$

Equations 12.8-5 and 12.8-6 set a minimum for Seismic Response Coefficient.

$$C_S^{min} = 0.044 S_{DS} I_e = 0.044 \times 1.424 \times 1.0 = 0.06266$$

$$C_S^{min} = \frac{0.5 S_1}{\frac{R}{I_e}} = \frac{0.5 \times 0.718}{\frac{5}{1.0}} = 0.07180$$

The calculated seismic response is more than the minimum. The seismic weight of each floor is determined per Section 12.7.2. The effective seismic weight, W, of a structure shall include the dead load as defined in section 3.1. The assumed total dead load of the building distributed over the floor plan is.

$$\omega_D = 100 + 25 = 125\ psf$$

$$W_f = 131 \times 131 \times 0.125 = 2{,}145\ kips, \qquad W = 10 W_f = 10 \times 2{,}145 = 21{,}450\ kips$$

$$V = C_S W, \qquad V = 0.1226 \times 21{,}450 = 2{,}630\ kips$$

Assuming two walls for resisting the lateral loads, base shear in one wall would be one half of the total base shear of the building.

$$V_w = \frac{1}{2} \times 2{,}630 = 1{,}315\ kips$$

Accidental torsion is calculated assuming displacement of the center of mass each way from its actual location by a distance equal to 5 percent of the dimension of the structure perpendicular to the direction of applied forces.

$$e = 0.05 B_f, \qquad B_f = 131\ ft, \qquad e = 0.05 \times 131 = 6.55\ ft$$

The torque caused by the accidental torsion is calculated multiplying the eccentricity by the base shear.

$$M_{at} = eV = 6.55 \times 2{,}630 = 17{,}227\ kips - ft$$

This torque would induce additional shear force in the shear wall of one side of the building, and decreases the shear force of the wall on the other side. Assuming d is distance between walls, the additional shear is:

$$V_{at}d = M_{at} \xrightarrow{yields} V_{at} = \frac{M_{at}}{d} = \frac{eV}{d} = \frac{0.05B_fV}{d} = 0.05V$$

So, considering the accidental torsion, the shear wall on one side takes 55 percent of the total base shear and the shear wall on the other side takes 45 percent. So, base shear of each wall should be amplified to 10 percent more shear.

$$V_f = 1{,}315 \times 1.10 = 1{,}447\ kips$$

This is the total shear that should be resisted by the entire building. The lateral seismic force, F_x, induced at any level shall be determined from equations 12.8-11 and 12.8-12.

$$F_x = C_{vx}V, \qquad C_{vx} = \frac{w_x {h_x}^k}{\sum_{i=1}^{n} w_i {h_i}^k}, \qquad k = 1.0 + \frac{1.02 - 0.5}{2.5 - 0.5} \times (2.0 - 1.0) = 1.26$$

The definition for each parameter is in Section 12.8.3 of ASCE 7. The numerical value for each parameter with the lateral force on one wall are shown in the following table.

Level	***Floor height [ft]***	***Floor weight [k]***	$w_i {h_i}^k$	C_{vi}	F_i [k]
R	*120*	*2,145*	*883,512*	*0.203*	*293*
F 10	*108*	*2,145*	*773,870*	*0.177*	*257*
F 9	*96*	*2,145*	*667,328*	*0.153*	*221*
F 8	*84*	*2,145*	*564,169*	*0.129*	*187*
F 7	*72*	*2,145*	*464,748*	*0.107*	*154*

Level	*Floor height [ft]*	*Floor weight [k]*	$w_i h_i^k$	C_{vi}	F_i [k]
F 6	*60*	*2,145*	*369,522*	*0.0847*	*123*
F 5	*48*	*2,145*	*279,104*	*0.0640*	*92.5*
F 4	*36*	*2,145*	*194,377*	*0.0446*	*64.4*
F 3	*24*	*2,145*	*116,733*	*0.0268*	*38.7*
F 2	*12*	*2,145*	*48,823*	*0.01119*	*16.2*

For a Risk Category II Building with S_{DS} of 1.424, and S_{D1} of 0.6223, the seismic design category referring to tables 11.6-1 and 11.6-2 is D. For a seismic design category D building, the redundancy factor is determined from Section 12.3.4.2. The structure is regular in plan at all levels and there are two walls on each side of the building in the perimeter. The equivalent number of frames, per section 12.3.4.2, part b, is calculated as the length of the shear wall divided by the story height.

$$n_f = \frac{L_w}{H_s} = \frac{27}{12} = 2.25$$

So, the building consists of at least 4 frames of lateral force resisting elements in the direction under consideration, and the redundancy factor is equal to 1.0. The shear and moment demands are shown in the table below.

Story	*Shear [kips]*	*Bottom Moment [1,000 kips - ft]*
10	*293*	*3.515*
9	*550*	*10.11*
8	*771*	*19.36*
7	*958*	*30.85*
6	*1,112*	*44.2*
5	*1,234*	*59.01*
4	*1,327*	*74.94*
3	*1,391*	*91.63*
2	*1,430*	*108.8*
1	*1,446*	*126.2*

The lateral loads for calculating the lateral displacements for drift check are calculated next. Per section 12.8.6.2, to determine compliance with the story drifts of section 12.12.1, it is permitted to calculate the elastic drifts, δ_{xe}, using seismic design forces based on the computed fundamental period of the structure without the upper limit specified in Section 12.8.2. So, $T = 1.403\ sec$ is used for calculating the lateral forces for drift check.

Story	***Floor lateral forces for drift check [kips]***	***Floor lateral displacements for drift check [in]***	***Drift ratio for drift check [%]***
10	*207.2*	*19.06*	*1.849*
9	*177.8*	*16.40*	*1.833*
8	*149.9*	*13.76*	*1.794*
7	*123.5*	*11.18*	*1.720*
6	*98.72*	*8.700*	*1.604*
5	*75.77*	*6.390*	*1.439*
4	*54.80*	*4.318*	*1.221*
3	*36.09*	*2.559*	*0.9466*
2	*20.04*	*1.196*	*0.6125*
1	*7.325*	*0.3135*	*0.2177*

The upper bound and lower bound of distributed gravity loads are calculated as follows.

$\omega_u^5 = (1.2 + 0.2S_{DS})\omega_D + 0.5\omega_L = (1.2 + 0.2 \times 1.424) \times 125 + 0.5 \times 40 = 205.6\ psf$

$\omega_u^7 = (0.9 - 0.2S_{DS})\omega_D = (0.9 - 0.2 \times 1.424) \times 125 = 76.9\ psf$

Assuming $55\ ft \times 35\ ft$ tributary area of gravity loads for each wall (estimated using a finite element analysis in ETABS), the axial gravity load over the height is computed in table below.

Story	***LC5 axial load***	***LC7 axial load***
10	*395.8*	*148.0*
9	*791.6*	*296.1*
8	*1187*	*444.1*

Story	*LC5 axial load*	*LC7 axial load*
7	*1583*	*592.1*
6	*1979*	*740.2*
5	*2375*	*888.2*
4	*2770*	*1036*
3	*3166*	*1184*
2	*3562*	*1332*
1	*3958*	*1480*

Note that for a nonlinear dynamic analysis, an estimate of the expected gravity loads determined by $P_u^{NL} = DL + 0.25LL$ is used to reduce the number of required runs. The total gravity load at the base of the wall using tis load combination is:

$$P_u^{NL} = DL + \frac{1}{4}LL = 2{,}600\ kips$$

The flexural demand of $126{,}200\ k-ft$, paired with axial gravity loads of $3{,}958\ kips$ and $1{,}480\ kips$ control the flexural design of the wall. The P-M interaction diagram of the final design (Cross section shown in Figure 3-38) is shown below.

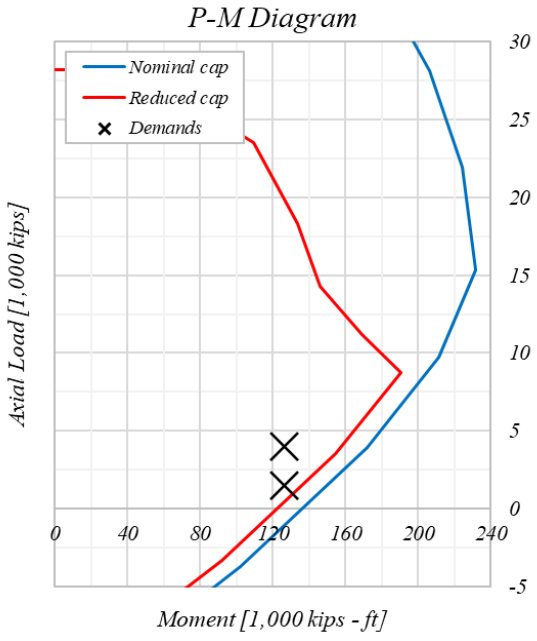

The reduced, and nominal flexural capacity of the wall for the upper bound and lower bound of the gravity loads, and the gravity load of the nonlinear dynamic analyses are shown in table below.

	LC7 axial load	***Nonlinear dynamic analysis axial load***	***LC5 axial load***
φM_n [1,000 k – ft]	*136.3*	*144.9*	*155.0*
M_n [1,000 k – ft]	*151.3*	*161.0*	*172.2*

The deformation parameters of the backbone curve for nonlinear modeling of the wall are calculated here. Table 4-1 and Table 4-2 determine the deformation parameters based on the axial load on the wall section, maximum probable shear demand, and the maximum depth of compression zone. Ignoring the effect of slab shear on the axial load of the wall, the maximum axial load on the wall is equal to the expected gravity load.

$$p_u = \frac{P_u}{A_g f'_c} = \frac{2{,}600}{26 \times 324 \times 7.8} = 0.0396$$

ACI 318-19 section 18.10.3.1 estimates the maximum shear demand of the wall, V_e.

$$V_e = \Omega_v \omega_v V_u$$

In this equation, V_u is the shear force determined per Equivalent Lateral Force Procedure.

$$V_u = 1{,}446\ kips$$

ω_v is the dynamic amplification factor due to effect of higher modes. ACI and the New Zealand Standard estimate this per number of stories.

$$\omega_v = 1.3 + \frac{n_s}{30} \leq 1.8, \qquad \omega_v = 1.633$$

Ω_v is the flexural overstrength factor. The flexural capacity of the wall considering the over strength of the material is approximately 1.25 of the nominal capacity, calculated with the nonlinear analysis axial load on the wall. The overstrength is then computed as follows.

$$\Omega_v = \frac{M_{pr}}{M_u} = \frac{1.25 \times 161.0}{126.2} = 1.59 > 1.5$$

The maximum shear demand is then:

$$V_e = \Omega_v \omega_v V_u = [1.595 \times 1.633 = 2.605 < 3] \times 1{,}446 = 3{,}768\ kips$$

The shear stress to use for finding deformation parameters in Table 4-1 is:

$$v_e = \frac{3{,}768 \times 1000}{26 \times 324 \times \sqrt{7{,}800}} = 5.06$$

The last parameter to be calculated is the compression zone parameter. The approximate depth of compression zone, using the nonlinear analysis gravity load, and the compression zone parameters are:

$$c_E = 71.82\ in, \qquad \lambda = \frac{L_w c_E}{b^2} = \frac{324 \times 71.82}{26 \times 26} = 34.42$$

Deformation parameters d, d', and e are calculated by interpolating the values in the table.

$$d = 0.02354, \qquad d' = 0.02867, \qquad e = 0.03186$$

The values obtained from the table are based on the height of the plastic hinge being equal half the length of the wall, as recommended by Moehle and Wallace, and modeling with a nonlinear element of Figure 5-2 (c).

$$l_p = \frac{H_{PZ}}{2} = \frac{L_w}{2} = \frac{324}{2}$$

To convert these values to deformation parameters of a nonlinear element with fiber section over the entire height, Eq. 5-28 is used. One element over the bottom story is used.

$h_{BE} = 144\ in$

To find the elastic rotation of the wall, a moment curvature analysis is done on the wall section. The moment curvature diagram with critical points is shown in the figure below. A bilinear is fit on the curve to estimate the yield point.

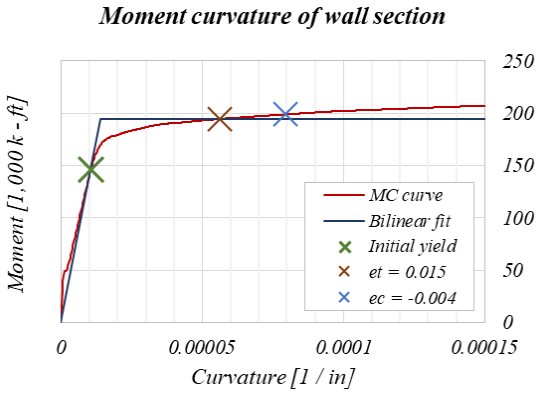

The yield moment, and the effective flexural stiffness of the wall are obtained using the bilinear fit on the moment curvature. The elastic rotation of the element in calculated per Eq. 5-20.

$$M_Y = 194{,}400\ kips - ft, \qquad EI_e = 1.657 \times 10^{11}\ kips - in^2, \qquad \theta_e^1 = \frac{M_Y}{K_{NLE}} = \frac{M_Y}{\frac{EI_e}{l_p = 162\ in.}} = 0.002280$$

The elastic rotation of the nonlinear element used in the study is calculated in the same way. Only the element size is different.

$$\theta_e^2 = \frac{M_Y}{K_{NLE}} = \frac{M_Y}{\frac{EI_e}{l_p = 144\ in.}} = 0.002027$$

Parameter r in Eq. 5-20 is calculated as follows, with the assumption that the extent of nonlinearity is equal to the length of the wall, $H_{PZ} = L_w$.

$$r = \frac{144}{324} = 0.444$$

The new deformation parameters are calculated as follows.

$$d = 0.01673, \qquad d' = 0.02027, \qquad e = 0.02248$$

These rotations are then divided by the element height to obtain the equivalent curvature. The equivalent curvatures are inserted in commands that builds the wall element.

7.4 Details of tested wall specimens in the database

Some additional data and Metadata regarding the structural wall tests in the database of 5.6 are presented in this chapter.

7.4.1 Tests conducted by Segura and Wallace (2017)

Figure 7-3 shows the layout of LVDTs in Segura's tests used to measure curvature profile over height. The rotations calculated by LVDTs 4, and 5 measure the curvature over the bottom three segments and the base rotation due to slippage and extension of longitudinal bars. Once the total rotation due to deformation of bottom three segments is subtracted from the rotation of LVDTs 4 and 5, the base rotation is obtained.

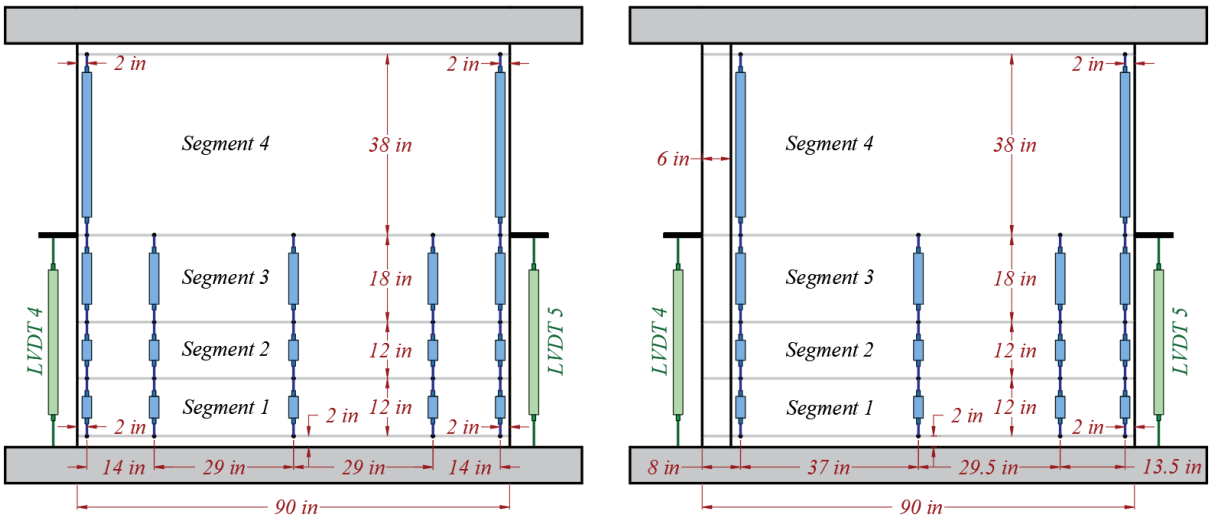

Figure 7-3 Layout of LVDTs used for measuring curvature in tests conducted by Segura and Wallace. Right: Specimen WP4, Left: All other specimens

The force deformation response of specimens, and the load steps at which the curvature profiles are calculated are shown in Figure 7-4. In these figures, the plastic hinge rotation (The reference deformation) refers to the rotation calculated by LVDTs 4 and 5 shown in Figure 7-3.

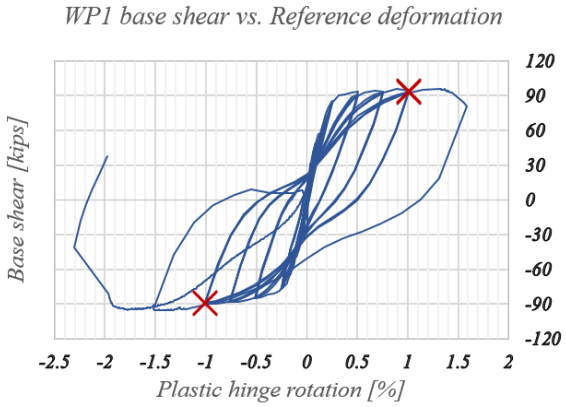
WP1 base shear vs. Reference deformation
Base shear [kips]
120
90
60
30
0
-30
-60
-90
-120
-2.5 -2 -1.5 -1 -0.5 0 0.5 1 1.5 2
Plastic hinge rotation [%]

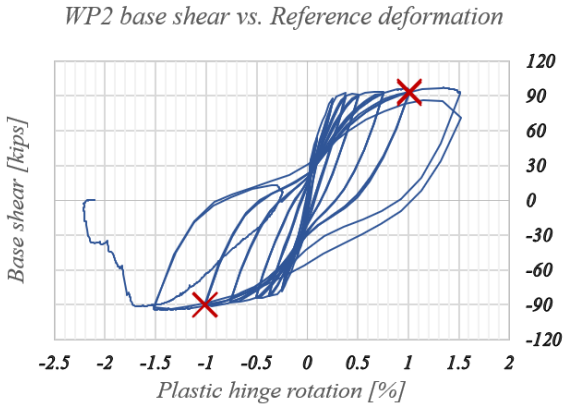
WP2 base shear vs. Reference deformation
Base shear [kips]
120
90
60
30
0
-30
-60
-90
-120
-2.5 -2 -1.5 -1 -0.5 0 0.5 1 1.5 2
Plastic hinge rotation [%]

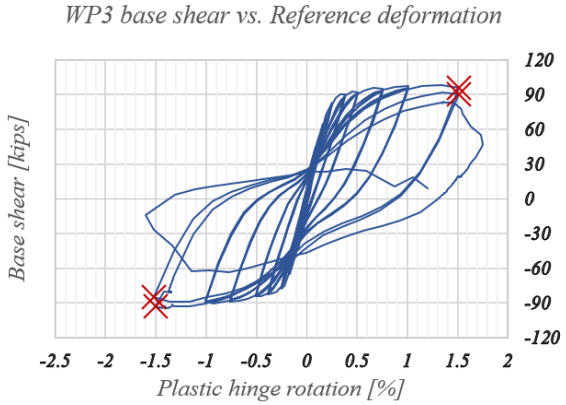
WP3 base shear vs. Reference deformation
Base shear [kips]
120
90
60
30
0
-30
-60
-90
-120
-2.5 -2 -1.5 -1 -0.5 0 0.5 1 1.5 2
Plastic hinge rotation [%]

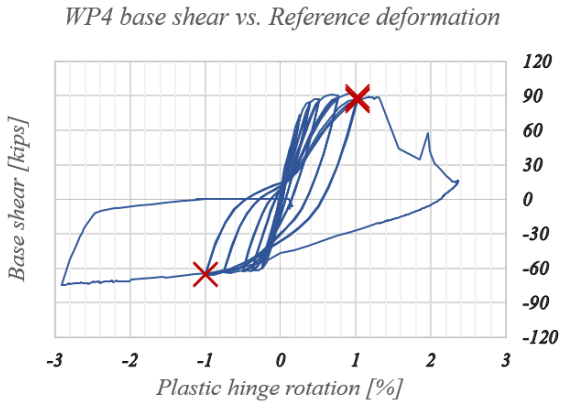
WP4 base shear vs. Reference deformation
Base shear [kips]
120
90
60
30
0
-30
-60
-90
-120
-3 -2 -1 0 1 2 3
Plastic hinge rotation [%]

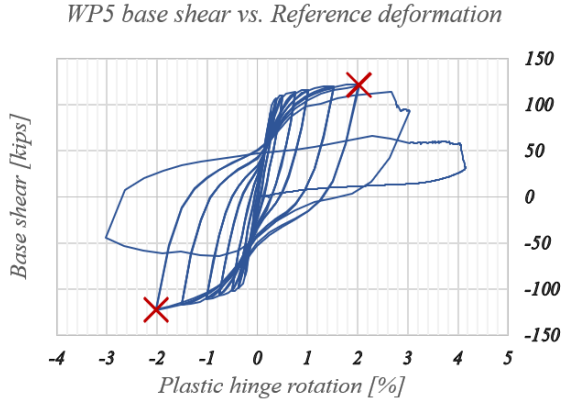
WP5 base shear vs. Reference deformation
Base shear [kips]
150
100
50
0
-50
-100
-150
-4 -3 -2 -1 0 1 2 3 4 5
Plastic hinge rotation [%]

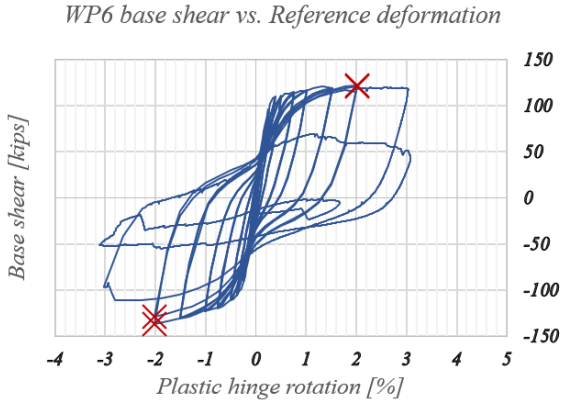
WP6 base shear vs. Reference deformation
Base shear [kips]
150
100
50
0
-50
-100
-150
-4 -3 -2 -1 0 1 2 3 4 5
Plastic hinge rotation [%]

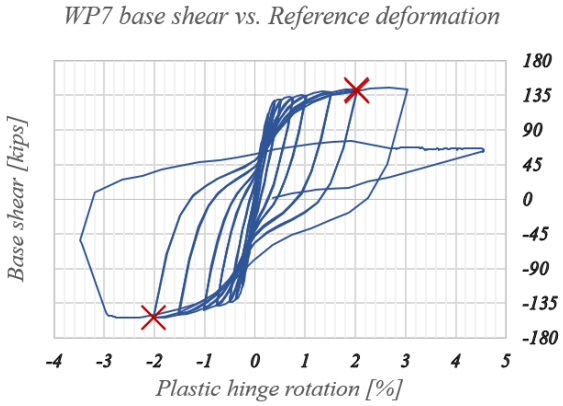

Figure 7-4 Force deformation response of specimens tested by Segura and Wallace. The load steps at which the curvature profile is calculated at are marked by red crosses.

Specimens do not have symmetric cross sections. So, the positive and negative direction of loading are treated as different data points for analyses.

The profiles of curvature over height, for specimens tested by Segura and Wallace are shown in Figure 7-5. The curvatures are normalized by the yield curvature calculated according to 5.6.3. The figures also show the bilinear fits on the curvature profiles. The bilinear fit is used to estimate the nonlinear height of the specimens, as discussed in 5.6.1.

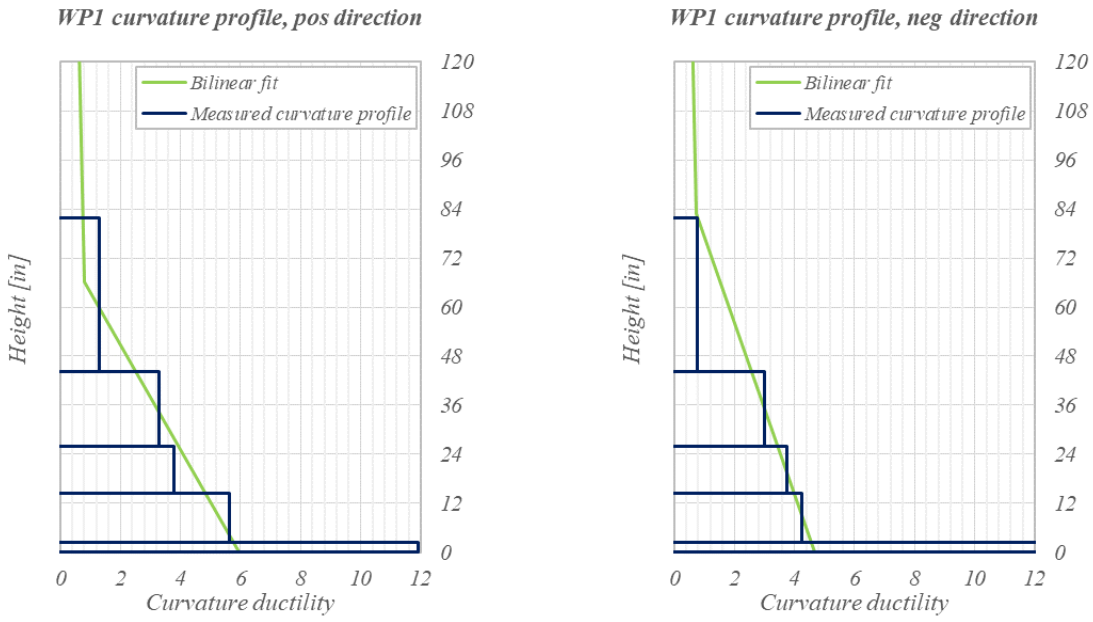

WP2 curvature profile, pos direction

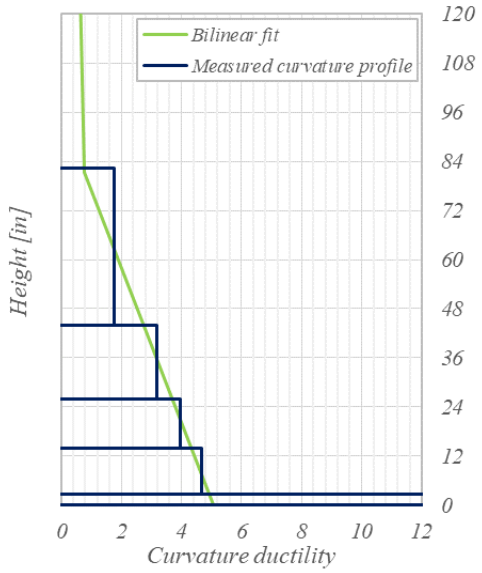

WP2 curvature profile, neg direction

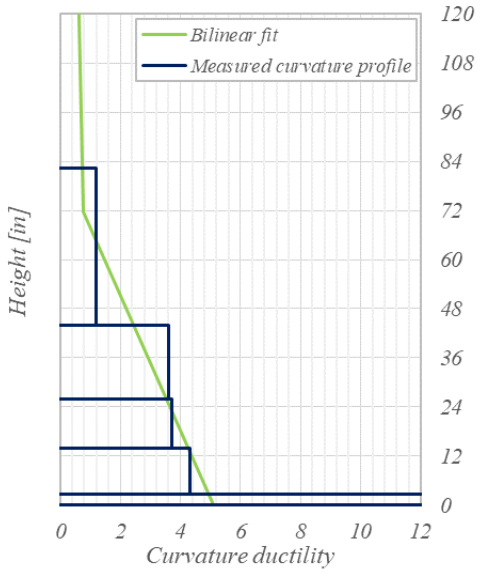

WP3 curvature profile, pos direction

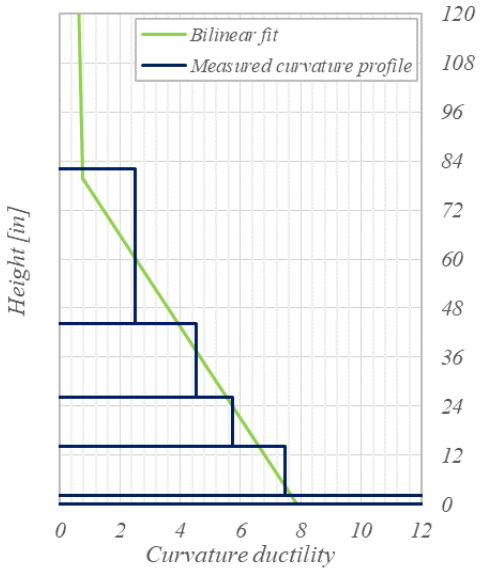

WP3 curvature profile, neg direction

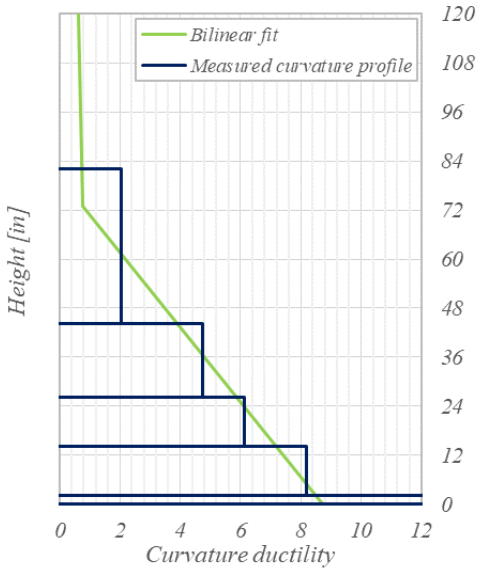

WP4 curvature profile, pos direction

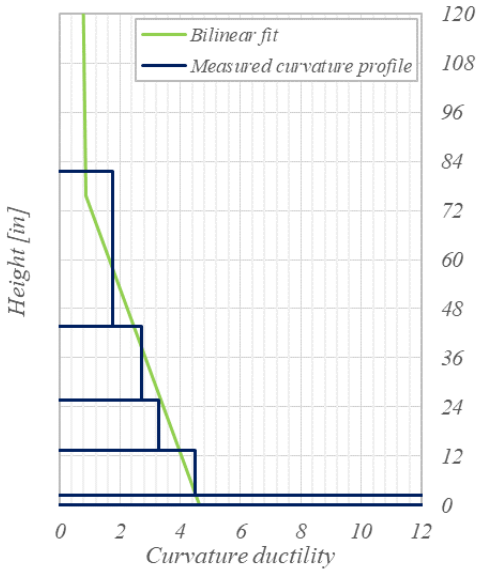

WP4 curvature profile, neg direction

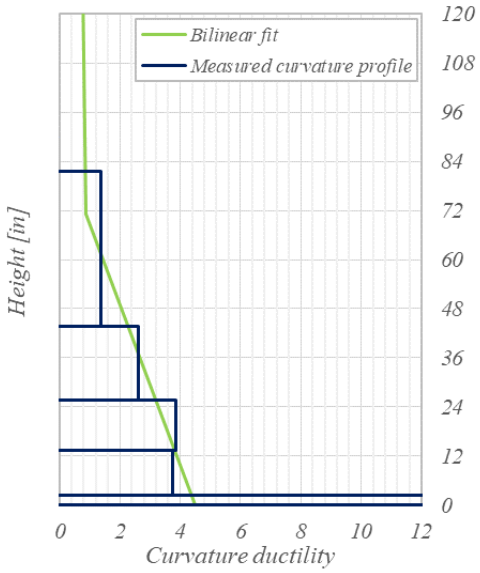

WP5 curvature profile, pos direction

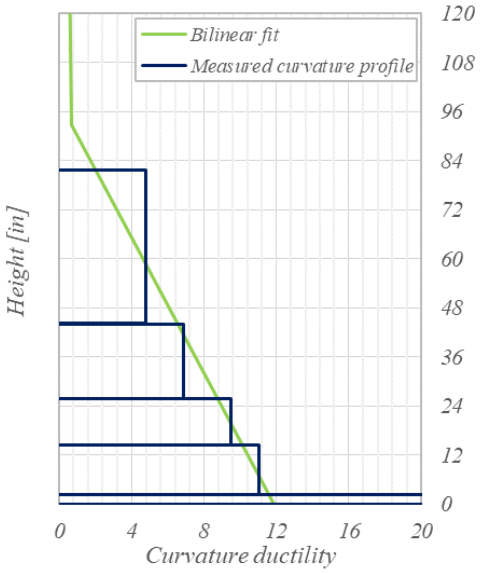

WP5 curvature profile, neg direction

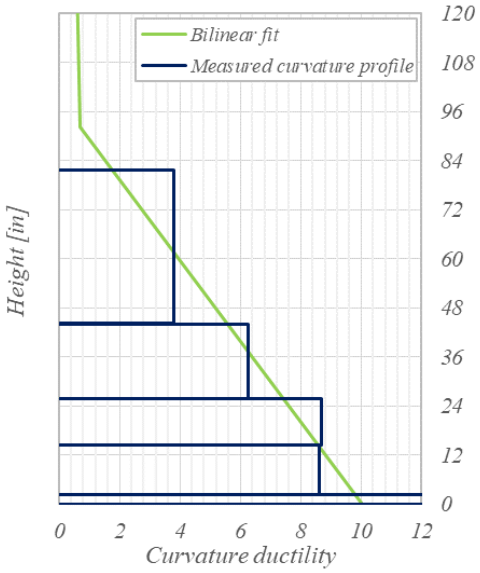

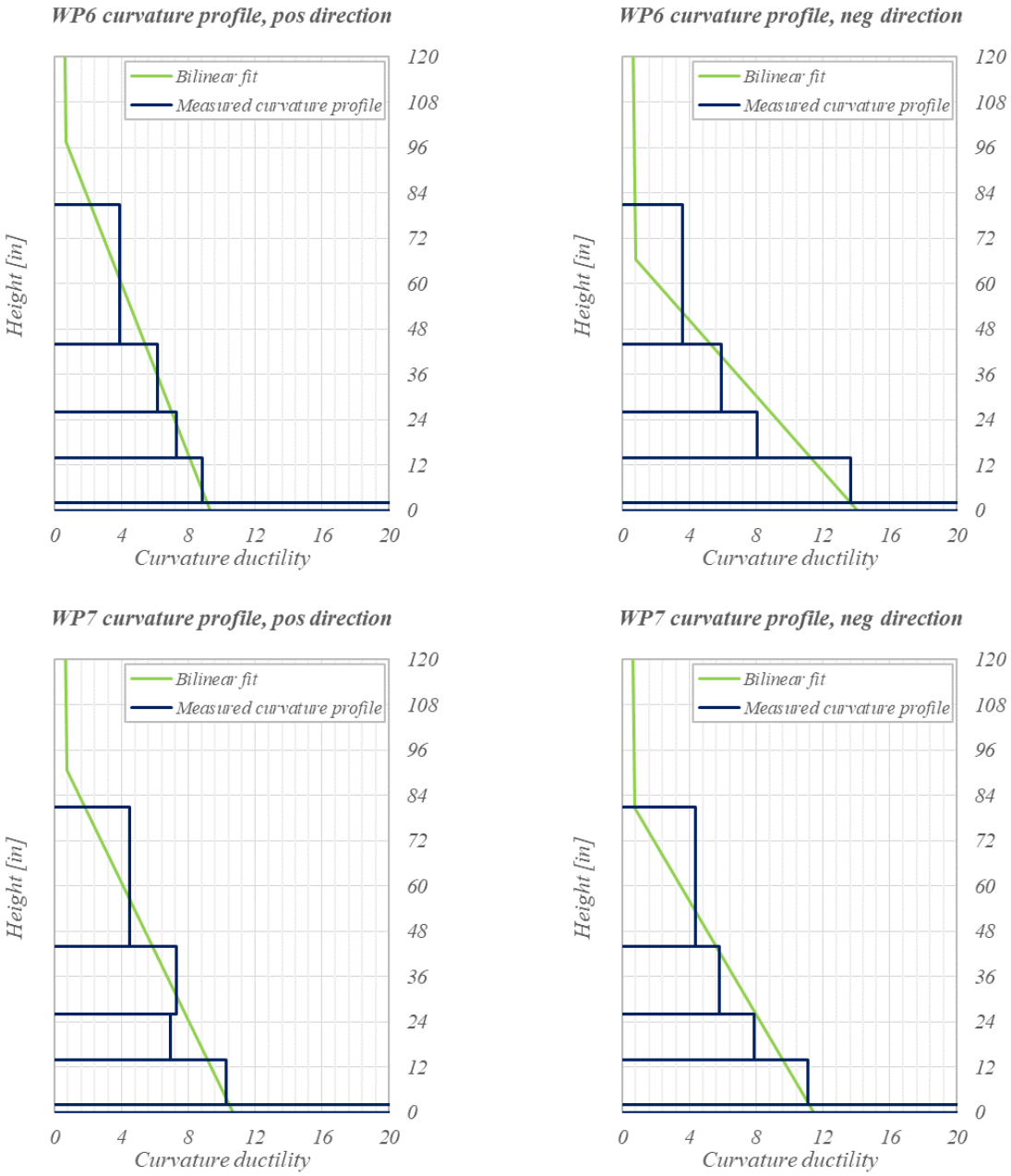

Figure 7-5 Curvature profile of specimen WP7 tested by Segura and Wallace in positive and negative directions

7.4.2 Tests conducted by Dazio, Beyer, and Bachmann (1999)

Figure 7-6 shows layout of LVDTs used to measure curvature over height. LVDT "1 N" and LVDT "1 S" measure curvature over the bottom 60-mm segment in addition to the rotation at the base of

the wall due to slippage and extension of longitudinal bars. Note that the bottom pin of these LVDTs lie on the footing.

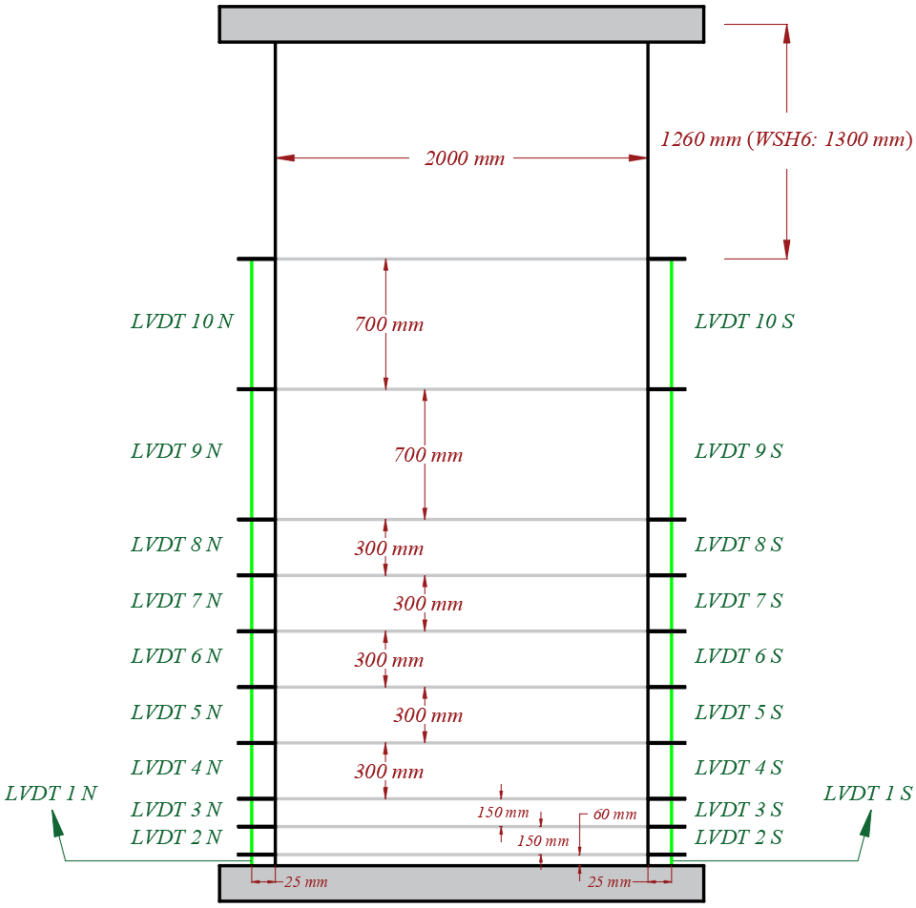

Figure 7-6 Layout of LVDTs used for measuring curvature in tests conducted by Dazio et al.

The force deformation response of specimens, and the load steps at which the curvature profiles are calculated are shown in Figure 7-7. In these figures, the reference deformation is the drift of the wall measured by the string potentiometer installed at the elevation of horizontal actuator (4,520 mm for WSH2 through WSH5, and 4,560 for WSH6).

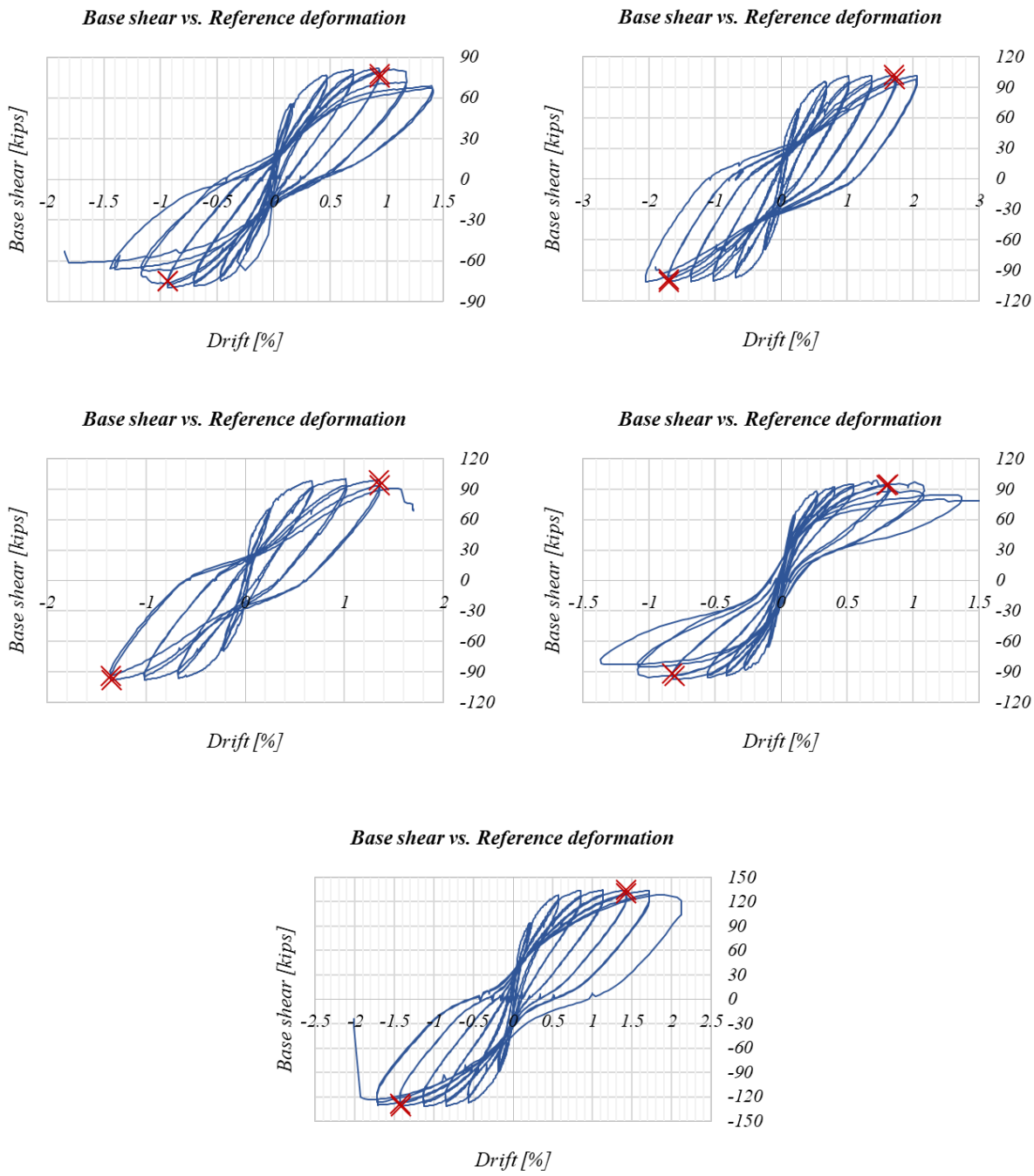

Figure 7-7 Force deformation response of specimens tested by Dazio et al. The load steps at which the curvature profile is calculated at are marked by red crosses.

The profiles of curvature over height, for specimens tested by Dazio et al. are shown in Figure 7-6.

The curvatures are normalized by the yield curvature calculated according to 5.6.3. The figures

also show the bilinear fits on the curvature profiles. Bilinear fit is used to estimate the nonlinear height of the specimens.

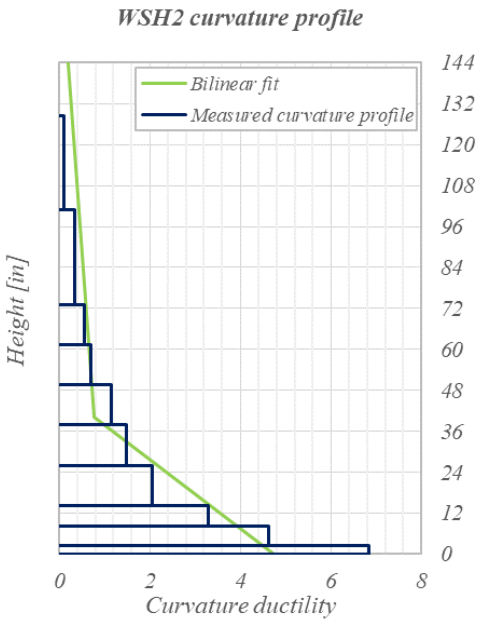

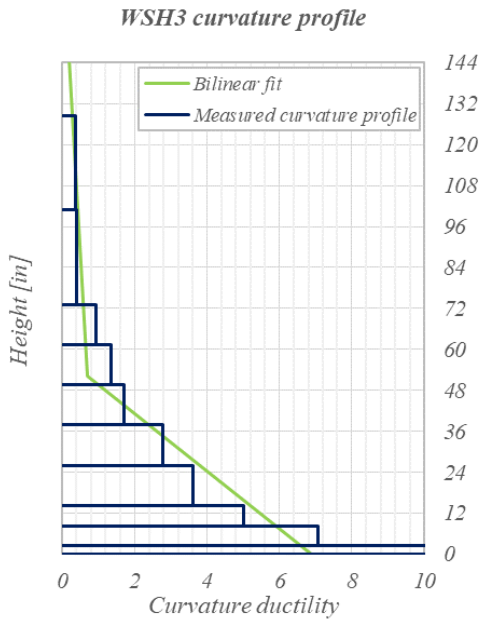

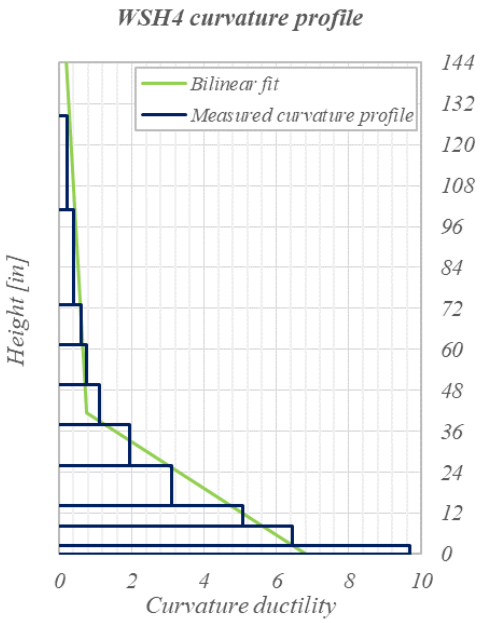

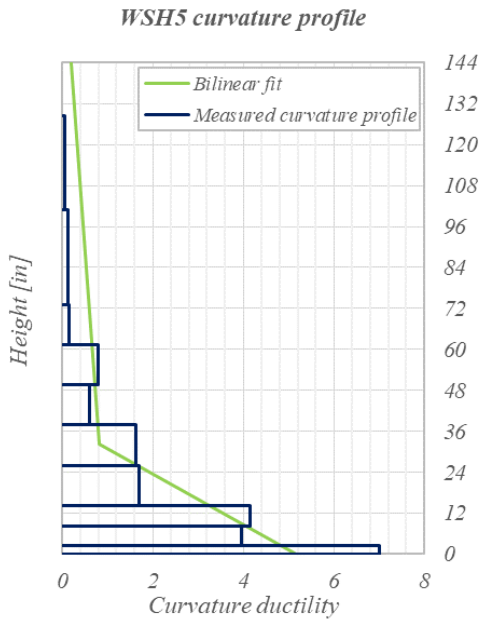

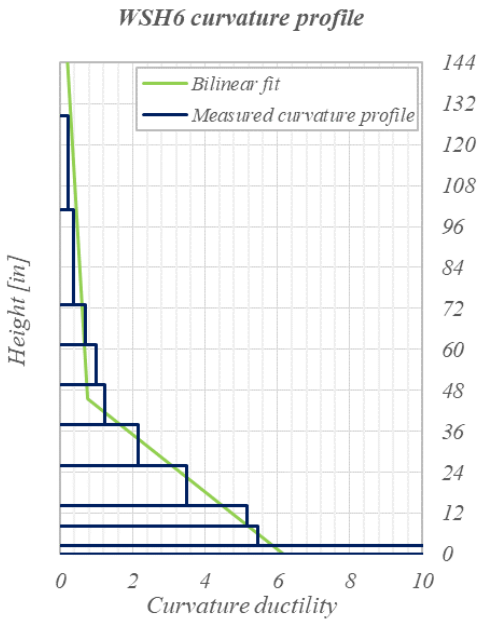

Figure 7-8 Curvature profile of specimens tested by Dazio et al.

7.4.3 Tests conducted by Tran and Wallace (2012)

Figure 7-9 shows layout of LVDTs used to measure curvature over height. The left figure corresponds to specimens “RW A20 P10 S38” and “RW A20P10S63”, and the right figure corresponds to specimens “RW A15 P10 S51”, “RW A15 P10 S78”, and “RW A15 P25 S64”. LVDT 29 and LVDT 30 measure curvature over the bottom 24-inch segment in addition to the rotation at the base of the wall due to slippage and extension of longitudinal bars. Note that the bottom pin of these LVDTs lie on the footing.

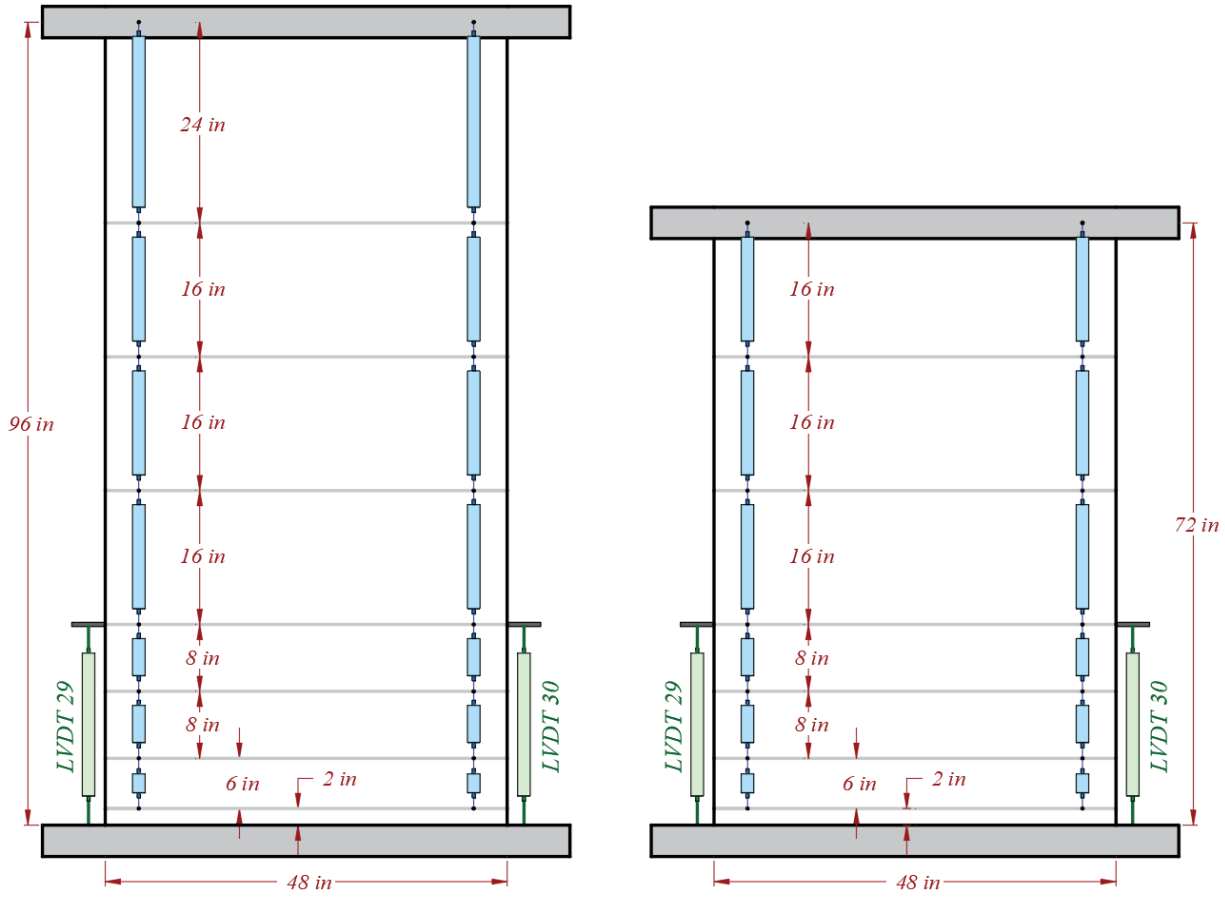

Figure 7-9 Layout of LVDTs used for measuring curvature in tests conducted by Tran and Wallace

The force deformation response of specimens, and the load steps at which the curvature profiles are calculated are shown in Figure 7-10. In these figures, the reference deformation is the drift of

the wall measured by the string potentiometer installed at the elevation of horizontal actuator (96 in for A20 specimens, and 72 in for A15 specimens).

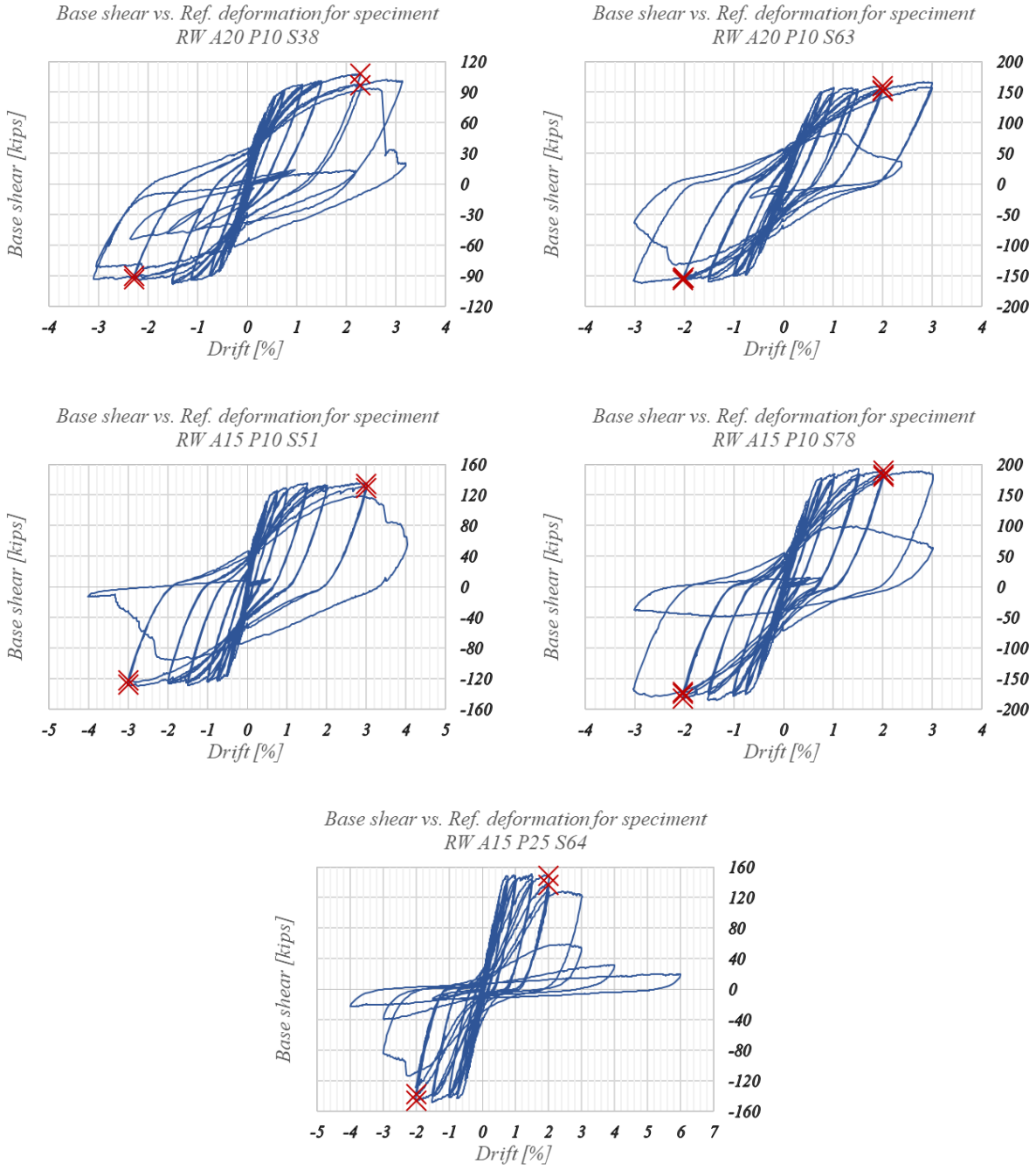

Figure 7-10 Force deformation response of specimens tested by Tran and Wallace. The load steps at which the curvature profile is calculated at are marked by red crosses.

The profiles of curvature over height, for specimens tested by Tran and Wallace are shown in Figure 7-11. The curvatures are normalized by the yield curvature calculated according to 5.6.3. The figures also show the bilinear fits on the curvature profiles. Bilinear fit is used to estimate the nonlinear height of the specimens.

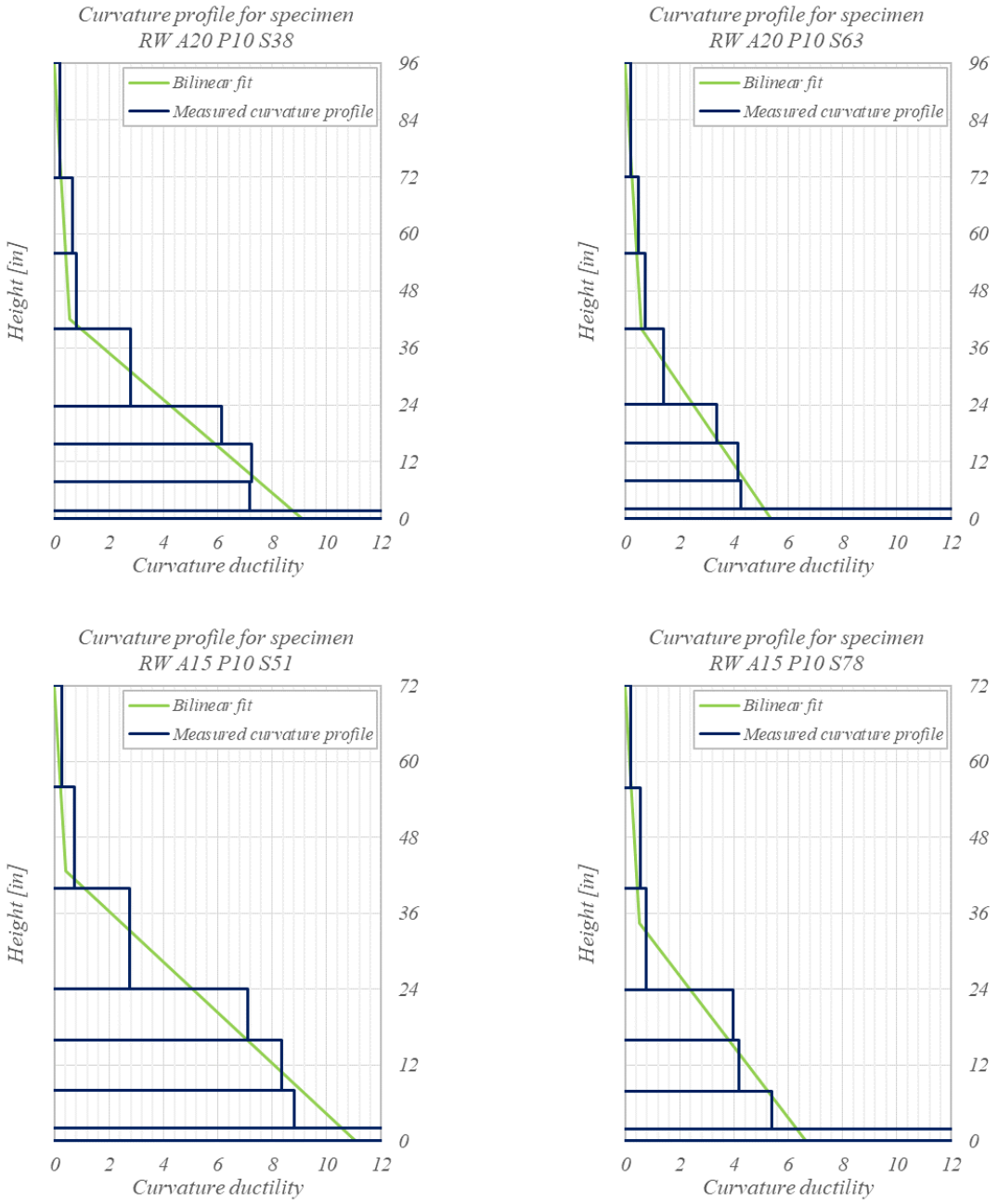

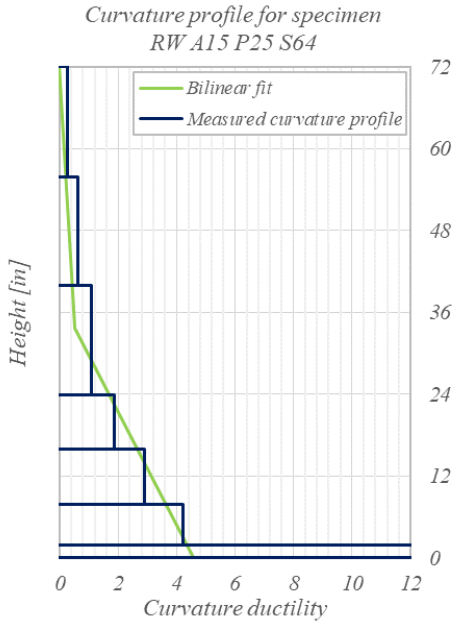

Figure 7-11 Curvature profile of specimens tested by Tran and Wallace

Chapter 8 References

1. Minimum design loads and associated criteria for buildings and other structures: provisions. (2022). American Society of Civil Engineers.
2. Seismic Evaluation and Retrofit of Existing Buildings (ASCE/SEI 41-17). (2017). American Society of Civil Engineers.
3. Guidelines for performance-based seismic design of tall buildings: developed by the Pacific Earthquake Engineering Research Center (PEER) as part of the Tall Buildings Initiative. (2010). Pacific Earthquake Engineering Research Center, College of Engineering, University of California.
4. McKenna, F. (2011). OpenSees: a framework for earthquake engineering simulation. Computing in Science & Engineering, 13(4), 58-66.
5. Clough, R. W. (1966). Effect of stiffness degradation on earthquake ductility requirements. In Proceedings of Japan earthquake engineering symposium.
6. Improvement of nonlinear static seismic analysis procedures. (2005). Dept. of Homeland Security, Federal Emergency Management Agency.
7. Effects of strength and stiffness degradation on seismic response / prepared by Applied Technology Council; prepared for Federal Emergency Management Agency, Department of Homeland Security. (2009). Federal Emergency Management Agency, Dept. of Homeland Security.
8. Ibarra, L. F., Medina, R. A., & Krawinkler, H. (2005). Hysteretic models that incorporate strength and stiffness deterioration. Earthquake engineering & structural dynamics, 34(12), 1489-1511.

9. Building code requirements for structural concrete (ACI 318-19): an ACI standard; Commentary on building code requirements for structural concrete (ACI 318R-19) / reported by ACI Committee 318. (2019). American Concrete Institute.
10. Sivaselvan, M. V., & Reinhorn, A. M. (2000). Hysteretic models for deteriorating inelastic structures. Journal of engineering mechanics, 126(6), 633-640.
11. Chenouda, M., & Ayoub, A. (2008). Inelastic displacement ratios of degrading systems. Journal of structural engineering, 134(6), 1030-1045.
12. Takayanagi, T., & Schnobrich, W. C. (1979). Non-linear analysis of coupled wall systems. Earthquake Engineering & Structural Dynamics, 7(1), 1-22.
13. Otani, S., Kabeyasawa, T., Shiohara, H., & Aoyama, H. (1984). Analysis of the Full Scale Seven Story Reinforced Concrete Test Structure.
14. Vulcano, & Bertero, V. V. (1987). Analytical models for predicting the lateral response of R C shear walls: evaluation of their reliability (p. 99 pages–99 pages).
15. Vulcano, A., Bertero, V. V., & Colotti, V. (1988, August). Analytical modeling of RC structural walls. In Proceedings, 9th world conference on earthquake engineering (Vol. 6, pp. 41-46).
16. Zhou, Y. (1988). Test investigation of the effect of section shape and reinforcement on seismic behavior of the isolated walls. Research Institute of Structural Engineering, Tsinghua University, Beijing, China.
17. Fajfar, P., & Fischinger, M. (2022). Mathematical modelling of reinforced concrete structural walls for nonlinear seismic analysis. In Structural Dynamics-Vol 1 (pp. 471-478). Routledge.

18. Orakcal. (2001). Macroscopic modeling for nonlinear analysis of reinforced concrete structural walls / by Kutay Orakcal. University of California, Los Angeles.
19. Orakcal, K., Wallace, J. W., & Conte, J. P. (2004). Flexural modeling of reinforced concrete walls-model attributes. Structural Journal, 101(5), 688-698.
20. Orakcal, K., & Wallace, J. W. (2006). Flexural modeling of reinforced concrete walls-experimental verification. ACI Materials Journal, 103(2), 196.
21. Thomsen IV, J. H., & Wallace, J. W. (2004). Displacement-based design of slender reinforced concrete structural walls—experimental verification. Journal of structural engineering, 130(4), 618-630.
22. Thomsen, J. H., IV, and Wallace, J. W. (1995). ‘‘Displacement-based design of reinforced concrete structural walls: Experimental studies of walls with rectangular and T-shaped cross sections.’’ Rep. No. CU/CEE-95/06, Department of Civil and Environmental Engineering, Clarkson University, Potsdam, N.Y.
23. 2019 California Building Code: California Code of Regulations, Title 24, Part 2 / California Building Standards Commission. 2019. Washington, D.C: International Code Council.
24. Park, R., & Paulay, T. (1975). Reinforced Concrete Structures, John Wiley & Sons. NY, USA.
25. Paulay, T., & Priestley, M. N. (1992). Seismic design of reinforced concrete and masonry buildings (Vol. 768). New York: Wiley.
26. Priestley, M. J. N., & Kowalsky, M. J. (1998). Aspects of drift and ductility capacity of rectangular cantilever structural walls. Bulletin of the New Zealand Society for Earthquake Engineering, 31(2), 73-85.

27. Berry, M. P., & Eberhard, M. O. (2003). Performance Models for Flexural Damage in Reinforced Concrete Columns., Pacific Earthquake Engineering Research Center Report 2003. Univ. of California, Berkeley.
28. Kazaz, İ. (2013). Analytical study on plastic hinge length of structural walls. Journal of Structural Engineering, 139(11), 1938-1950.
29. Saatcioglu, M., & Razvi, S. R. (1992). Strength and ductility of confined concrete. Journal of Structural engineering, 118(6), 1590-1607.
30. Chang, G. A., & Mander, J. B. (1994). Seismic Energy Based Fatigue Damage Analysis of Bridge Columns: Part I - Evaluation of Seismic Capacity (p. 222). Buffalo, NY: National Center for Earthquake Engineering Research.
31. Takahashi, S., Yoshida, K., Ichinose, T., Sanada, Y., Matsumoto, K., Fukuyama, H., & Suwada, H. (2013). Flexural drift capacity of reinforced concrete wall with limited confinement. ACI Structural Journal, 110(1), 95.
32. Matsubara, S., Sanada, Y., Tani, M., Takahashi, S., Ichinose, T., & Fukuyama, H. (2013). Structural Parameters of Confined Area Affect Flexural Deformation Capacity of Shear Walls That Fail in Bending with Concrete Crushing. Journal of Structural and Construction Engineering, 78(691), 1593-1602.
33. Orakcal, K. (2004). Nonlinear modeling and analysis of slender reinforced concrete walls. University of California, Los Angeles.
34. Segura, C. L. (2017). Seismic performance limitations of slender reinforced concrete structural walls. University of California, Los Angeles.
35. Segura Jr, C. L., & Wallace, J. W. (2018). Impact of geometry and detailing on drift capacity of slender walls. ACI Structural Journal, 115(3), 885-895.

36. Segura Jr, C. L., & Wallace, J. W. (2018). Seismic performance limitations and detailing of slender reinforced concrete walls. ACI Structural Journal, 115(3), 849-859.

37. Tran, T. A., & Wallace, J. W. (2012, September). Experimental study of nonlinear flexural and shear deformations of reinforced concrete structural walls. In 15th World Conference on Earthquake Engineering.

38. Kolozvari, K., Orakcal, K., & Wallace, J. W. (2015). Modeling of cyclic shear-flexure interaction in reinforced concrete structural walls. I: Theory. Journal of Structural Engineering, 141(5), 04014135.

39. Kolozvari, K., Tran, T. A., Orakcal, K., & Wallace, J. W. (2015). Modeling of cyclic shear-flexure interaction in reinforced concrete structural walls. II: Experimental validation. Journal of Structural Engineering, 141(5), 04014136.

40. Tran, T. A. (2012). Experimental and analytical studies of moderate aspect ratio reinforced concrete structural walls (Doctoral dissertation, UCLA).

41. Rathje, E. M., Dawson, C., Padgett, J. E., Pinelli, J. P., Stanzione, D., Adair, A., ... & Mosqueda, G. (2017). DesignSafe: New cyberinfrastructure for natural hazards engineering. Natural Hazards Review, 18(3), 06017001.

42. Dazio, A., Beyer, K., & Bachmann, H. (2009). Quasi-static cyclic tests and plastic hinge analysis of RC structural walls. Engineering Structures, 31(7), 1556-1571.

43. Dazio, A., Wenk, T., & Bachmann, H. (1999). Versuche an Stahlbetontragwänden unter zyklisch-statischer Einwirkung (Vol. 239). ETH Zurich.

44. Bozorgnia, Y., Abrahamson, N. A., Atik, L. A., Ancheta, T. D., Atkinson, G. M., Baker, J. W., ... & Youngs, R. (2014). NGA-West2 research project. Earthquake Spectra, 30(3), 973-987.

45. Ancheta, T. D., Darragh, R. B., Stewart, J. P., Seyhan, E., Silva, W. J., Chiou, B. S. J., ... & Donahue, J. L. (2014). NGA-West2 database. Earthquake Spectra, 30(3), 989-1005.
46. Abdullah, S. A., & Wallace, J. W. (2019). Drift capacity of reinforced concrete structural walls with special boundary elements. ACI Structural Journal, 116(1), 183.
47. Abdullah, S. A. (2019). Reinforced concrete structural walls: Test database and modeling parameters. University of California, Los Angeles.
48. Bohl, A. G. (2006). Plastic hinge length in high-rise concrete shear walls (Doctoral dissertation, University of British Columbia).
49. Menegotto, M., & Pinto, P. E. (1973). Method of analysis for cyclically loaded reinforced concrete plane force and bending. In Proceedings, IABSE Symposium on Resistance and Ultimate Deformability of Structures Acted on by Well Defined Repeated Loads, Lisbon (pp. 15-22).
50. Abdullah, S. A., & Wallace, J. W. (2018, June). UCLA-RC walls database for reinforced concrete structural walls. In Proceedings of the 11th national conference in earthquake engineering.
51. Wallace, J. W., & Moehle, J. P. (1992). Ductility and detailing requirements of bearing wall buildings. Journal of Structural Engineering, 118(6), 1625-1644.
52. Zhao, X., Wu, Y. F., Leung, A. Y., & Lam, H. F. (2011). Plastic hinge length in reinforced concrete flexural members. Procedia Engineering, 14, 1266-1274.
53. Standard, B. (2005). Eurocode 8: Design of structures for earthquake resistance. Part, 1, 1998-1.

54. LATBSDC (2020). "An alternative procedure for seismic analysis and design of tall buildings located in the Los Angeles region.", Los Angeles Tall Buildings Structural Design Council, Los Angeles, CA.
55. Massone, L. M., & Wallace, J. W. (2004). Load-deformation responses of slender reinforced concrete walls. Structural Journal, 101(1), 103-113.